# ABSTRACT

Title of dissertation: UNCOVERING FUNDAMENTAL MECHANISMS OF ACTOMYOSIN CONTRACTILITY USING ANALYTICAL THEORY AND COMPUTER SIMULATION

James Komianos
Doctor of Philosophy, 2018

Dissertation directed by: Professor Garegin Papoian
Department of Chemistry and Biochemistry

Actomyosin contractility is a ubiquitous force-generating function of almost all eukaryotic organisms. While more understanding of its dynamic non-equilibrium behavior has been uncovered in recent years, little is known regarding its self-emergent structures and phase transitions that are observed *in vivo*. With this in mind, this thesis aims to develop a state-of-the-art computational model for the simulation of actomyosin assemblies, containing detailed cytosolic reaction-diffusion processes such as actin filament treadmilling, cross-linker (un)binding, and molecular motor walking. This is explicitly coupled with novel mechanical potentials for semi-flexible actin filaments. Then, using this simulation framework combined with other analytical approaches, we propose a novel mechanism of contractility in a fundamental actomyosin structural element, derived from a thermodynamic free energy gradient favoring overlapped actin filament states when passive cross-linkers are present. With this spontaneous cross-linking, transient motors such as non-muscle myosin

II can generate robust network contractility in a collective myosin II-cross-linker ratcheting mechanism. Finally, we map the phases of contractile behavior of disordered actomyosin using this theory, showing explicitly the cross-linking, motor and boundary conditions required for geometric collapse or tension generation in a network comprised of those elements. In this theory, we move away from the sarcomeric contractility mechanism typically reconciled in disordered non-muscle structures. It is our hope that this study adds theoretical knowledge as well as computational tools to study the diverse contractile assemblies found in non-muscle actomyosin networks.

# UNCOVERING FUNDAMENTAL MECHANISMS OF ACTOMYOSIN CONTRACTILITY USING ANALYTICAL THEORY AND COMPUTER SIMULATION

by

James Komianos

Dissertation submitted to the Faculty of the Graduate School of the
University of Maryland, College Park in partial fulfillment
of the requirements for the degree of
Doctor of Philosophy
2018

Advisory Committee:
Professor Garegin Papoian, Chair/Advisor
Professor Chris Jarzynski
Professor Michelle Girvan
Professor Arpita Upadhyaya
Professor Sergei Sukharev, Dean's Representatitve

Dedication

*To my grandmother, Yolanda Zaffutti*

*1930-2018*

# Acknowledgments

There are many people to thank for making this work possible. First, to my adviser, Garyk Papoian, I cannot thank you enough for your guidance through this interesting research. You have taught me so much about science and developing original ideas which I will carry throughout the rest of my career. I am glad to see our work develop into a large and successful project. It has been great to learn from such a talented researcher and develop a great friendship in the process.

My committee of Michelle Girvan, Chris Jarzynski, Sergei Sukharev, and Arpita Upadhyaya generated many productive comments and overall review of the work in this thesis. It has been an excellent opportunity to work and collaborate with them in the Biophysics program and to learn from their extensive knowledge in various subjects. This work would not be possible without the research environment that they have helped to develop at the University of Maryland.

I would like to thank the great team of *MEDYAN* developers in the Papoian lab, including the original developer Kostya Popov, and later developers Aravind Chandrasekaran, Qin Ni, Cal Floyd, and Haoran Ni. It is exciting that you all have contributed greatly to the code and are doing successful research projects in actin network dynamics. It has been a pleasure to work and spend time with you all in the last few years.

The rest of the Papoian lab were also essential in feedback and generating ideas for our work, including David Winogradoff, Haiqing Zhao, Hao Wu, Mary Pitman, and Ignacia Echeverria. I have enjoyed all of the discussions and ideas we

have exchanged about science and life. I will miss working in the lab with you all, and wish you the best in your future endeavors.

To the students, faculty, and administrative staff of the Biophysics program, Institute for Physical Science and Technology, as well as the Computational and Mathematics for Biological Networks program for continued support in my research, as well as for the camaraderie we have developed over the past years. These programs have given students at UMD an excellent environment to pursue computational biophysics research, which I am truly grateful for. I hope to see that success continue for years to come.

The Physics Department at Carnegie Mellon University was also essential in providing a scientific foundation to pursue my research interests. I would like to thank my previous advisers Kunal Ghosh and Michael Widom, as well as Stephen Garoff and Riendhard Schumacher for their continued support through my course-work, research, and personal development. My time at Carnegie Mellon was an invaluable experience.

None of this work would be possible without the constant support of my family and friends through my time at the University of Maryland. To my loving parents Bill and Maryanne Komianos, I cannot thank you enough for providing me with everything that I've needed to pursue my academic goals. To my girlfriend Haley Burnside, I don't know what I would have done without your help through it all. And to all my friends in Washington, and from the University of Maryland and Carnegie Mellon, I thank you for all the support you have given me. We made it!

Of course, I have left many people out that have contributed to this work,

including old friends and mentors who have guided my experiences throughout the years. I thank you as well.

# Table of Contents

# List of Tables

# List of Figures

# List of Abbreviations

| | |
|---|---|
| *in vivo* | in the living |
| *in vitro* | in the glass |
| *in silico* | in silicon |
| F-actin | Filamentous actin |
| G-actin | Monomeric actin |
| ATP | Adenosine triphosphate |
| GTP | Guanosine triphosphate |
| Arp2/3 | Actin-related protein 2 and 3 complex |
| mDia2 | Diaphnous related formin 2 |
| WASP | Wiscott-Aldrich Syndrome Protein |
| TFM | Transmission Force Microscopy |
| AFM | Atomic Force Microscopy |
| MEDYAN | Mecanochemical Simulations of Active Networks |
| OpenMP | Open multi-processing |
| MPI | Message-passing interface |
| RDME | Reaction-diffusion master equation |
| NMII | Non-muscle myosin II |
| FENE | Finitely extensible non-linearly elastic |
| LAMMPS | Large-scale Atomic/Molecular Massively Parallel Simulator |
| pFD | Passive force dipole |
| aFD | Active force dipole |
| UD | Uni-directional motor |
| BD | Bi-directional motor |
| FB | Free boundary condition |
| TB | Tethered boundary condition |
| PALM | Photoactivated Localization Microscopy |
| STORM | Stochastic Optical Reconstruction Microscopy |

# Chapter 1: Introduction

Actomyosin networks are complex protein microstructures responsible for many of the dynamics seen in cellular life. Their formation and function, regulated by a wide assortment of signaling and regulatory proteins, is well conserved and one of the most ancient protein networks known in eukaryotes [31], forming even before the simpler muscle tissue. In fact, the cytoskeleton has been determined as a key factor spurring the development of eukaryotic life from prokaryotes [31, 32]. While researchers have begun to understand the key bio-molecular processes involved in its function through advancements in *in vivo* super-resolution microscopy and *in vitro* reconstituted and extracted cytoskeletal networks, actomyosin self-organization and force generation within cells remains poorly understood from a biophysical perspective. This has implications for a variety of complex cellular tasks relevant to biomedical research, such as invading tumor cells in cancer metastasis [195, 208].

The most fundamental function of actomyosin which lacks understanding in many instances is contractility, a ubiquitous inward motion or force caused by motor proteins binding to pairwise actin filaments, consuming ATP and walking directionally towards their plus ends. This motion, combined with transient linking of filaments by auxiliary cross-linking proteins, can rearrange actin networks into a

variety of organizations directly influencing cell membrane tension and morphology. This includes dynamic steady-states such as clusters, bundles, asters, and meshes. Dissecting how a network of protein polymers and motors such as actomyosin can produce contractile forces and rearrangement into a number of architectures by consuming chemical energy is an intriguing one and spans all branches of science including materials science, non-equilibrium physics and biochemistry. These are architectures not readily achieved with synthetic polymer gels. To answer these questions and investigate how these active materials can be understood and engineered, a variety of approaches must be employed, with detailed consideration of the biophysics underlying self-emergent behaviors of such a dynamic molecular network.

This thesis will investigate the biophysical mechanisms of actomyosin contractility, first by developing and benchmarking a state of the art computational model for representing actomyosin assemblies and other cytoskeletal systems. Then, this model will be used alongside other analytical and computational methods to describe novel mechanisms for the contractile dynamics of actomyosin. This begins from a description of contractility in one-dimensional actin filament pairs, typically regarded as actomyosin force dipoles, to entire disordered assemblies which contain many dipoles interacting in three dimensions. Through the chapters, we emphasize the combinations of cross-linking elements that are required to ellicit contractility in an actomyosin system, and that in particular, the combination of passively bound cross-linking and active walking by myosin II can be harnessed by the cellular cytoskeleton to produce powerful contractile machines.

To begin the thesis, we first give an overview and brief history of the actin

cytoskeleton - its function, regulation, and biophysical dynamics, to set the stage for our modeling considerations of a general cytoskeletal assembly. We will then highlight actomyosin dynamics in particular, focusing in on not only the methods of modeling them currently in the literature, but also interesting physics that result from their emergent behavior to motivate our contractility study. Then we will revisit the thesis claims in a more specific context and give a roadmap of the the chapters.

## 1.1 Overview of the actin cytoskeleton

The cytoskeleton has a part in many biological functions and can be thought of as the chemical engine of a cell. This biochemical machinery runs on adenosine triphosphate (ATP) and guanosine triphosphate (GTP) which are converted into mechanical force for cellular tasks. In eukaryotes, filamentous protein networks execute this function, with thousands of regulatory proteins that help to control its assembly based on extracellular signals. This can drastically alter cell shape and morphology by way of contacts with the cell membrane or other intra-cellular structures. For example, in cell division, a ring of actin filaments at the cytokinetic furrow is formed and contracted by motor proteins, consuming ATP and pinching the mother cell into daughters, while microtubules which hydrolyze GTP pull chromatin to both daughter cell bodies [18]. In a motile cell such as fibroblasts, actin filaments rich in ATP are able to rapidly polymerize into dense networks to develop a protrusive motion of the cell membrane in chemotactic response [23, 168].

The most functionally diverse of the cytoskeletal components is the polymerizing actin network, although microtubules display very interesting properties in their own right, including (de)polymerization, contractility and dynamic filament catastrophe [55, 79, 120]. Actin filaments (F-actin) are produced by the polymerization of actin globule protein (G-actin) monomers, which are approximately 42 $kDa$ [72]. Once polymerized, F-actin mechanically is a semi-flexible filament with persistence length 17 $\mu m$, a small diameter of 7 $nm$, and a double-helical structure [45]. There is a polarity associated with actin filaments, as the barbed (plus) end polymerizes more readily than the pointed (minus) end at steady-state conditions [147]. This is due to the conformational asymmetry of actin monomers when binding to a filament [173]. Further aided by the ability of G-actin in filament to hydrolyze ATP, F-actin readily produces a "treadmilling" process *in vivo*, where filament plus ends polymerize with more conformationally favorable ATP-rich monomers and depolymerize unfavorable ADP-bound monomers [57]. This treadmilling is shown in Fig 1.1, and is essential in a variety of mechanochemical tasks independent of auxiliary proteins. For example, actively polymerizing filaments can rectify Brownian motion when close to a fluctuating membrane to generate mechanical force as proposed by Peskin et al. [141]. This is harnessed by the cell as a fundamental mechanism for protrusive forces from within.

Other regulatory proteins have a large role in mediating the assembly of actin structures *in vivo*, allowing for remodeling of actin filaments in certain cellular regions. Since the spontaneous nucleation of actin filaments is highly unfavorable [146] as shown in Fig 1.1, specific regulatory proteins named nucleators exist to stabilize

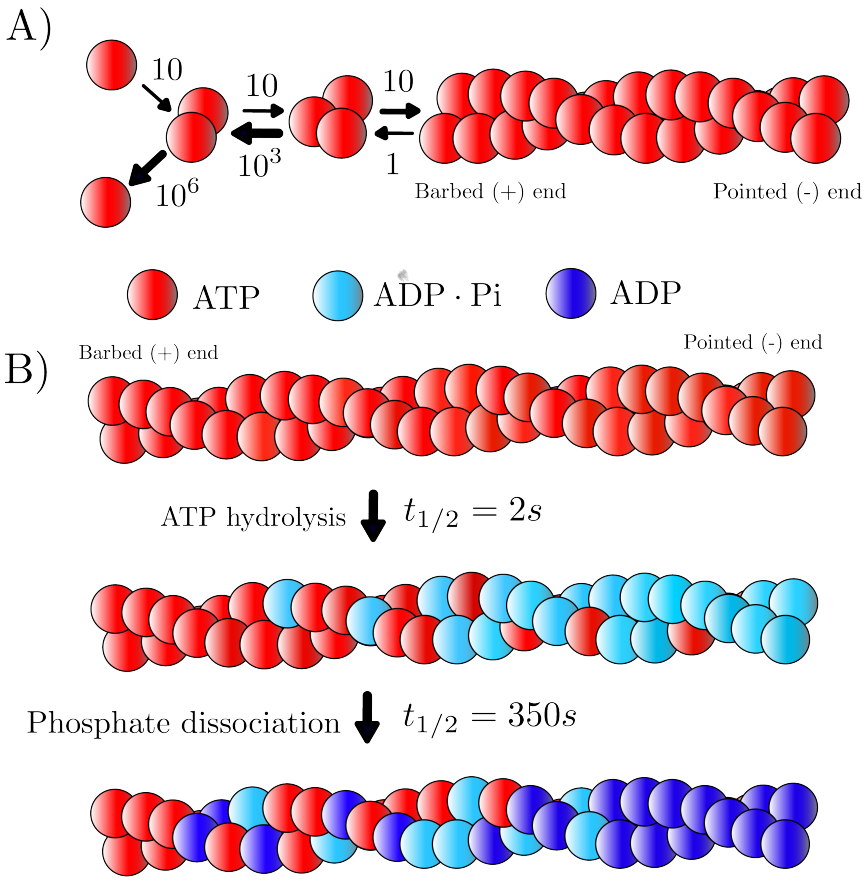


Figure 1.1: The structure and kinetics of an actin filament. a) Actin readily polymerizes into double helical-filaments, although the formation of a stable trimer is extremely rare unless aided by nucleating proteins (Rate constants are shown in $\mu m^{-1}s^{-1}$ for association reactions and $s^{-1}$ for dissociation). b) The chemical state of an actin monomer in filamentous form determines the turnover dynamics of a particular filament. ATP hydrolysis happens relatively quickly in actin monomers once bound to the plus end, transitioning to a ADP-Pi state (half-life of $2s$). Eventually, the phosphate is freed (much larger half-life of 6 minutes), resulting in rapid depolymerization of monomers from the minus end. Image adapted from [145].

the creation of actin filaments from single actin monomers, allowing for localized assembly. Formins are a class of proteins that provide this function to actin monomers in cells. Activated by the Rho-family GTPases downstream from extracellular signaling [21], formins bind to actin monomers, eventually producing a stable actin trimer configuration, the minimal building block for a growing actin filament [146].

Formins can also bind to pre-existing filaments and increase their polymerization rate [97] by way of tracking polymerizing plus ends, as shown in a kinetic model by Vavylonis et al. [185]. Another important nucleator is Arp2/3, a seven-unit protein complex found readily in the cytoskeleton, which can initiate new actin filaments on the sides of existing filaments at a characteristic $70^o$ angle [126], generating a branched actin network structure. This nucleation requires not only the Arp2/3 itself but also the nucleation promoting factor Wiskott-Aldrich syndrome protein (WASP) [98, 169]. Together, these nucleators allow for explicit biochemical control of actin filament assembly in linear or branched architectures.

A great example of a dynamic cellular protrusion is in dendritic spine growth. In this process essential to neuronal development, the growing dendrite relies on the polymerization of actin filaments to extend finger-like protrusions, named spines (post-synaptic), towards other neurons (pre-synaptic). These protrusions stay relatively plastic, even during human adulthood where 5-10% of neural connections turn over per day [159]. Thus actin network dynamics are a hallmark in this process and contribute directly to memory formation and learning. Physically, dendrites are thought to be initially formed by the activated nucleating factor Arp2/3 establishing protruding bundles of actin filaments outward from the membrane [158]. This is in agreement with recent findings of a convergent elongation mechanism for filopodial protrusions introduced by Svitkina et al. [180] - in this mechanism, branched filaments are tightly bundled due to membrane-induced tensions. Later, this was shown to be physically plausible by Liu et al. who analyzed in vitro protrusion assays with an elastic membrane model [111]. After initiation of spine-like protrusions,

mDia2 formin molecules are further responsible for extending the protrusions in a dynamic search process [74]. Once a contact with a pre-synapse is found, the head region is expanded (typically named "long-term potentiation") via Arp2/3 branched networks, which localizes neurotransmitters to the surface. The function of post-synaptic mushroom shape is still not well known but could be optimal for signal propagation [15]. Fig 1.2 shows the general shape and emergence of a dendritic spine.

To perform more intricate tasks such as lamellipodial protrusion in a motile cell or to develop a dendritic spine head and neck, further regulation is needed to control branched actin network remodeling. Antagonistic to nucleating proteins, there exist many regulatory molecules which are necessary for the disassembly of actin filaments to enhance either the network's monomer recycling or control average filament length [24]. In particular, capping proteins are an important regulatory molecule that can bind to the plus ends of actin filaments blocking network polymerization. These proteins are highly active in the function of a branched network protruding against a membrane, which our lab has studied in detail using Gillespie-based stochastic models. By interacting with dendritic networks at the leading edge of the cell, Hu and Papoian showed that capping proteins can help to develop a robust protrusion velocity profile of a leading edge when under external force [78]. Hu and Papoian also showed enhanced protrusion speed for moderate capping of a dendritic network can also occur by increasing the pool of G-actin monomers for polymerization [77]. Along with capping protein function in a branched network, at the rear of a protrusion, Cofilin proteins are responsible for severing filaments such that actin can be reused

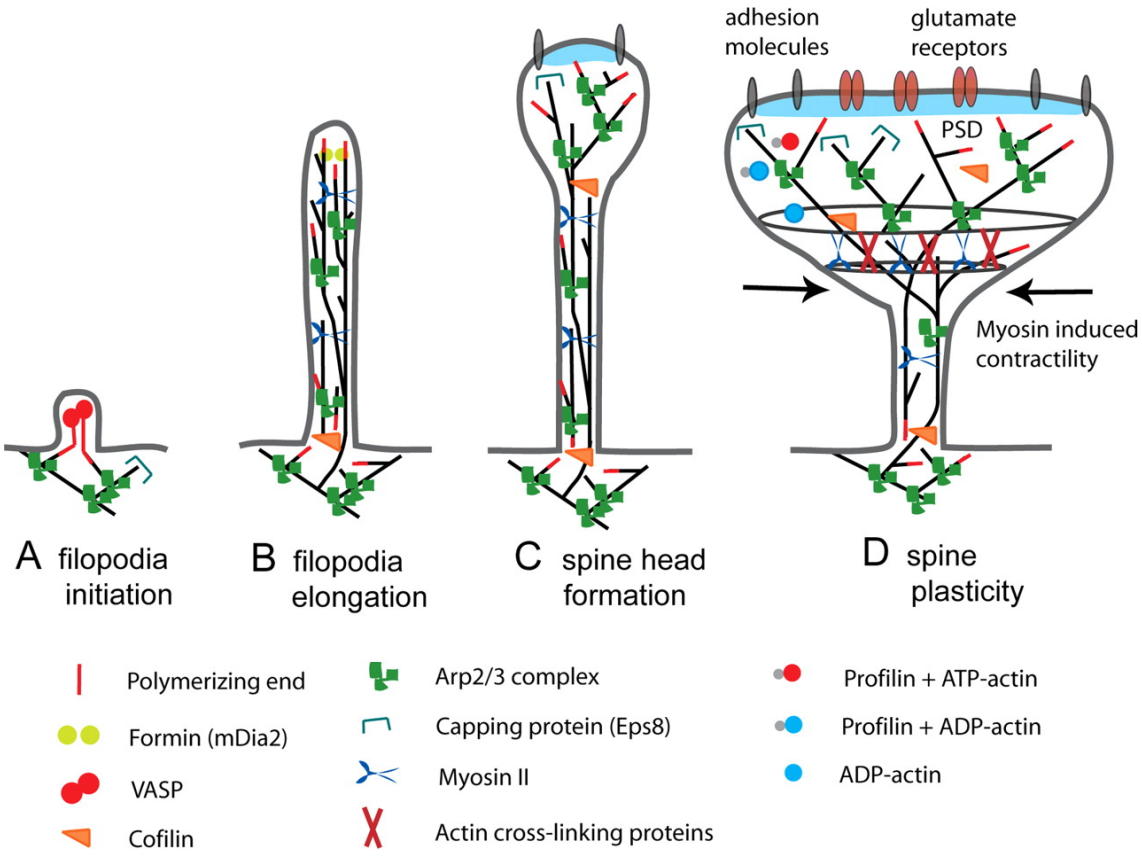


Figure 1.2: Dendritic spine formation and growth. a) Branched actin networks can create small protrusion from the leading edge via membrane-induced bundling. The cross-linking protein VASP aids in bundling of small filaments at the filipodial base to produce a more mechanically stable protrusion. b) Elongation of the protrusion occurs by formin mDia2 attaching to the plus ends of actin filaments and polymerizing them at an accelerated rate. c-d) Synaptic plasticity is mediated by the further protrusion of the mushroom spine shape and actin remodeling by Arp2/3. Cofilin helps to recycle ADP-bound actin monomers to the leading edge by decorating and severing actin filaments. Profilin, another regulatory protein, is also responsible for binding to actin monomers and mediating the exchange of ADP-ATP in those monomers as they recycle to the leading edge. Neural receptors eventually localize to the post-synaptic head region. Myosin II, cross-linking proteins, and other intermediate filaments such as Spectrin are thought to be responsible for producing the mechanical tension and integrity required for spine neck development. Reprinted from [107] with permission from *The Journal of Cell Biology*.

at the front of the network [7, 41]. Since Cofilin decoration is more favorable to occur on ADP-bound monomers [178], this promotes the disassembly of the aged, ADP-rich actin filaments, which can then rebind to ATP and recycle to the leading

edge. This recycling and protrusion is shown in in the dendritic spine maturation process in Fig 1.2.

## 1.2 Actomyosin-cross-linker contractility

Cells also rely heavily on contractile actin machinery along with protrusive mechanisms. Actomyosin is typically regarded as a tertiary system of actin, myosin II filaments and cross-linking proteins that can vary in geometry and organization to fulfill this need. We review the components of this system beginning with the structural basis of an actomyosin network - cross-linking proteins. Cross-linking is a particularly key tool of actin machinery for producing organized filament architectures, and acts by transiently binding and linking pairwise filaments. The properties of a cross-linker can greatly determine actin network polarity and organization. For example, the 35 $nm$ actin filament cross-linking protein $\alpha$-actinin is found in apolar actin filament bundles in the interior of motile cells [112], and can develop higher-order structures *in vitro* such as fibers and branched networks [109, 199]. Fascin, a smaller 8 $nm$ protein, is responsible for forming tighter, polar bundles observed in protruding filopodia [194]. *In vivo*, mutations of cross-linker expression displayed altered contractile behaviors in cells in TFM measurements, particularly solidification of the network in the case of varying kinetics of $\alpha$-actinin by Ehrlicher et al. [46] as well as increased traction forces in the case of Palladin knockdown by Azatov et al. [9]. *In vitro*, Schmoller et al. also demonstrated that the type of cross-linking protein can directly mediate actin bundle stiffness [163]. Based on these observations,

the transience and mechanical consequence of cross-linkers in actin networks when interacting with molecular motors will be a main factor in our study of contractility.

As cross-linking plays important roles in actin dynamics, molecular motors that utilize energy released due to chemical reactions and transfer it into mechanical work further drive actin dynamics and morphology. The myosin family of motors, found in the cytoskeleton, harnesses the energy from ATP hydrolysis, converting it into mechanical motion on actin filaments. In particular the myosin II family (non muscle IIA/IIB typically expressed in humans [20]) which bind to actin filaments and walk in the plus end direction, can produce sliding forces in the actin network and promote network reorganization [165, 192]. Since myosin II molecules are a non-processive motor in monomeric form, in order to produce stable attachments to actin filaments *in vivo*, they must polymerize, connecting their long tail regions in bipolar arrangement. This produces filaments with typically 28-30 monomers and up to 300 $nm$ length as imaged *in vitro* by Billington et al. [20]. Biochemically, formation of mini-filaments is regulated by many pathways which phosphorylate monomeric tail regions, inducing favorable filament polymerization in specific cell areas. Along with signaling regulation, myosin II is a catch bond when bound to actin, producing increased affinity under external load [68]. This provides mechanosensing ability in the form of tension-driven aggregation to certain cellular areas such as the cortex [113]. The basic interaction of myosin II filaments and actin filaments, interacting with other regulatory proteins is shown in Fig 1.3. Through signaling and mechanosensing mechanisms, myosin II plays a direct role along with cross-linking in the formation of many cellular structures, including the formation lamellar bun-

dles [183] and dorsal stress fibers which retract the cell rear in migration [130]. The function of myosin II and other regulatory proteins in forming a mature dendritic spine neck is also shown in Fig 1.2.

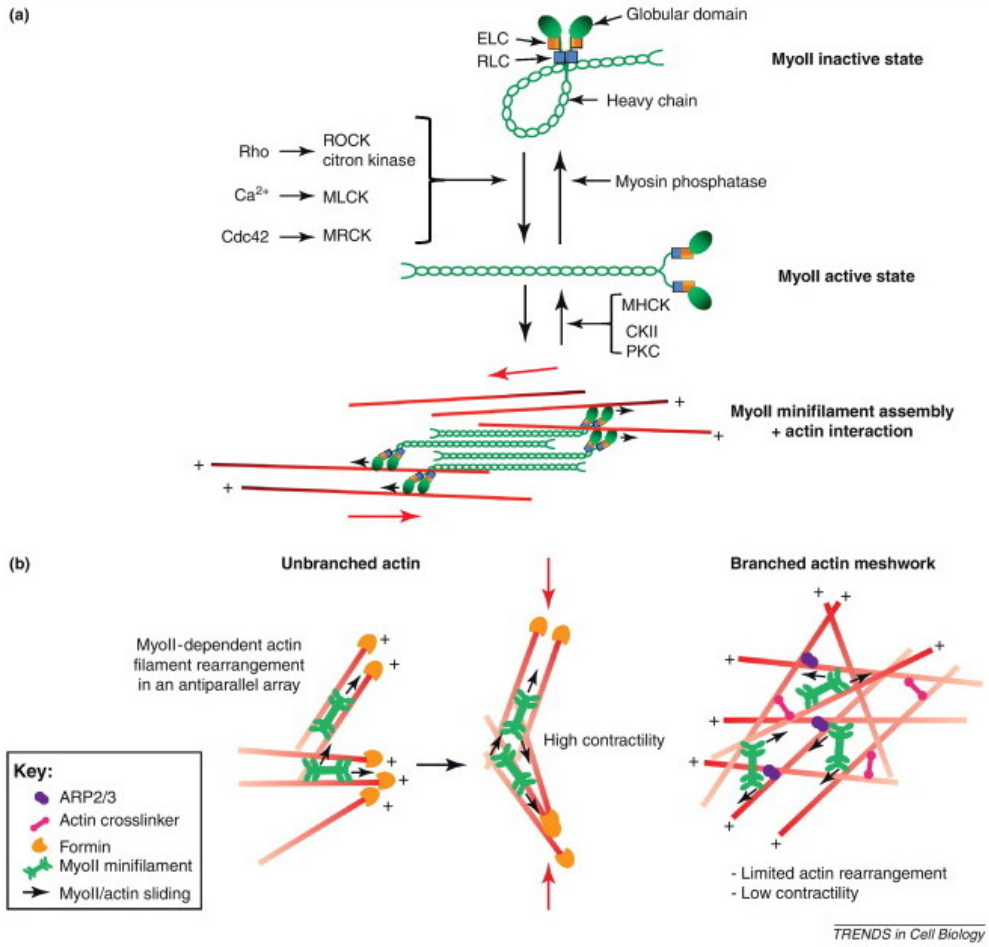


Figure 1.3: Actomyosin structure. a) Myosin II is a double-headed and unprocessive motor protein, which contains a long tail region. *In vivo*, non-muscle myosin filaments typically reach 28-30 molecules per filament and up to $300nm$ in length. Extracellular signaling can initiate the phosphorylation of the monomer tail, for example through the myosin II light chain kinase pathway, allowing for polymerization into filaments. b) Contraction occurs in non-muscle cells by way of myosin II filament heads hydrolyzing ATP and pulling directionally on many actin filaments. If the polarity of actin being considered is disordered, unlike a muscle cell, some symmetry breaking mechanism such as polarity organization must occur to produce overall contractile motion. It is also well-known that branched actin structures do not contract, possibly due to exclusion of large myosin II filaments from densely branched networks. Reprinted from [107] with permission from Elsevier.

With these components, non-muscle actomyosin can form robust contractile networks that are fluid between cell regions. This is quite unlike the muscle sarcomere form of contractility which has a static polarity and develops intuitive inward forces (described in detail in Chapter 3). To attempt to model this behavior, we must consider that the emergence of a diverse arrangement of structures is in part due to myosin II in non-muscle being highly transient [129] compared to its motor counterpart thick filaments [142], allowing for dissipation in actomyosin structure formation. Since kinetic measurements of non-muscle myosin II filaments are lacking due to its difficulty to purify and polymerize in vitro [20], analytical efforts must be used to aid in modeling small filaments of myosin II and their interactions with actin. A recent theoretical study of small mini-filaments by Erdmann et al. has revealed the original Hill force-velocity relation [71], which describes a concave relationship between stall force applied to a motor head and subsequent walking velocity, can in fact apply to such small stochastic ensembles. This consideration has been adopted recent agent-based cytoskeletal modeling approaches with more transient actomyosin behavior. Along with this, the catch bond nature of small myosin II filament isoforms has also been modeled stochastically by Stam et al. [175] and Greenberg et al. [67], showing a non-linear mechanosensitive response when operating in stiff environments. Our framework has adopted these results to model non-muscle myosin IIA motors [148], as well as have other three-dimensional Langevin-based polymer models [82, 85, 132]. Other models have also been used to study the contraction of disordered filament assemblies using motors with simpler mechanochemistry in two dimensions [48, 176]. In general, more modeling efforts

must consider these new types of transient and non-linear non-muscle actomyosin architectures for full realism.

So what controls the emergence of contractility in a disordered non-muscle network which has transient myosin II motors? Currently this is thought to be largely determined by the connectivity of a network that is imbedded with contractile force dipoles (myosin II bound to pairwise and oppositely polar actin filaments). Connectivity is typically described as the ratio of bonded neighbors in an idealized lattice network, however, cross-linker concentration can be directly tuned to affect connectivity in an actin filament system, since the concentration of soluble linkers determines the occupied fraction of pairwise actin binding sites. Using this idea, force percolation mechanisms have been studied *in vitro* by Alvarado et al. pointing to a classic conductivity percolation and scale-free cluster distribution of contractile networks when cross-linking concentration is increased above a threshold [4, 5]. Similarly Jung et al. showed in a detailed myosin II and actin Langevin model the transition of increasing cross-linker concentration to produce contractile force [82]. Along with elliciting contractility, connectivity not only has been shown to produce a transition to contractile structures but also an inhibitory effect at high concentrations *in vitro* [12, 48]. This has been modeled well by Wang et al. who used a cat's cradle tensegrity model to describe the biphasic behavior at high filament connectivities [204], agreeing with the work of Bendix et al. [12] which first showed this effect *in vitro*. In all, this work on has provided a perspective on contractility for many micron sized networks, which may not be relevant to a cellular structure. At length scales relevant to a cell, we also must consider that a system of semi-

flexible polymers and cross-linkers alone can display lamellar and bundled phases as displayed in recent finite element studies [37, 125].

There is still the question of how symmetry is broken at the molecular level to induce contractility of individual pairs of actin filaments, beyond the overall connectivity and reorganization of larger microstructures. Since actin filaments have high tensile strength but buckle readily under compressive loads, myosin II motors in an actin network could plausibly buckle filaments when walking in a non-contractile manner, generating robust network contractility. The *in vitro* work of Murrell and subsequent modeling efforts of Lenz et al. has shown that asymmetric buckling can readily contract apolar bundles and break contractile-extensile symmetry in non-muscle myosin II units [105, 106, 128], and multi-stage coarsening processes have also been shown to occur in reconstituted networks depending on buckling [171]. This reconciles the sarcomeric mode of contractility in disordered networks. Recently Ronceray et al. showed that contractile forces can propagate in a model disordered network due to a similar local deformation mechanism [156]. Finally Stam et al. showed anisotropic deformations can be tuned by filament deformability in similar model of disordered networks [176]. Figure 1.4 displays the buckling mechanism of filaments proposed. Along with most studies investigating contraction of actomyosin, some extensile states have been also been recently studied in model motor driven systems, questioning the robustness of actomyosin contractility in certain regimes of biochemical reaction rates and mechanical behavior [22, 58, 104].

The last consideration we have is of cytoskeletal networks to contract from passive cross-linking processes alone. This is interesting to consider because some

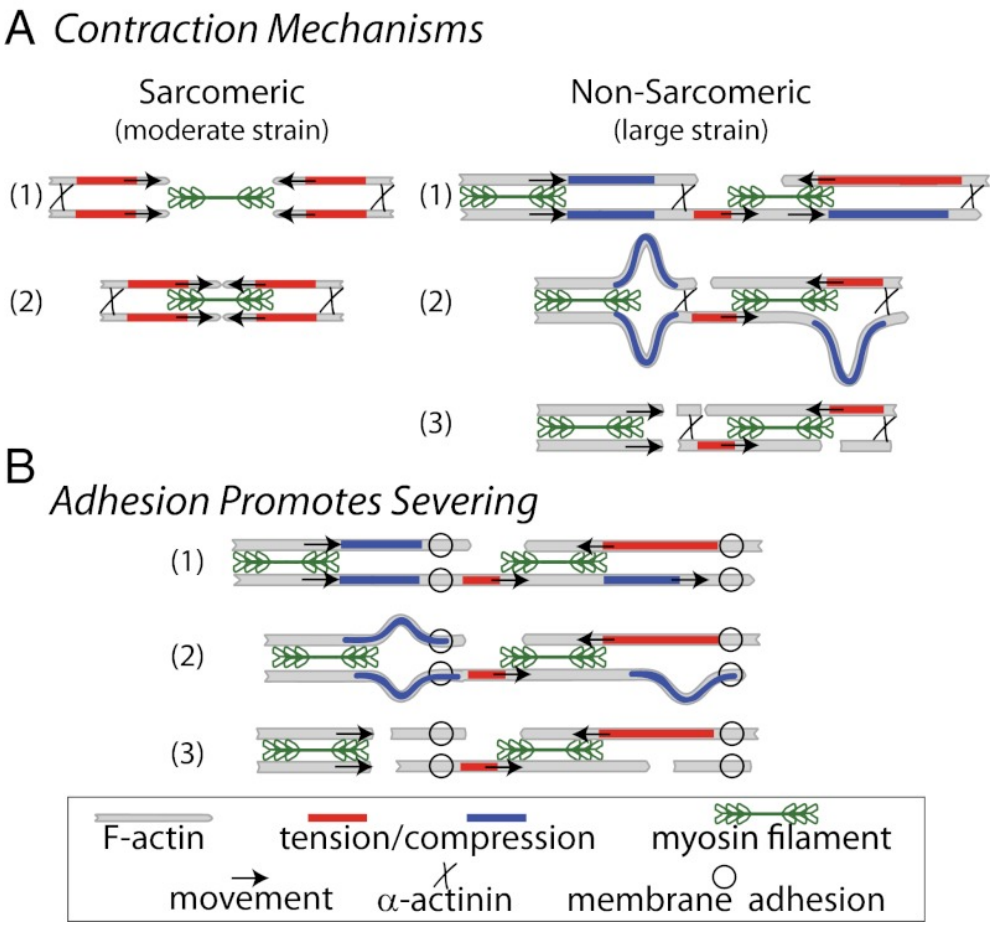


Figure 1.4: In Murrell et al., the buckling mechanisms of actin-myosin networks was presented using a *in vitro* quasi-2D disordered actomyosin network on a model lipid bilayer coverslip. This describes the basic idea of the buckling mechanism - a) The sarcomeric mode of actomyosin contractility is geometrically intuitive and requires no symmetry breaking mechanism for inward motion. When in a disordered arrangement, however, which creates extensile filament force along with contractile, actin filaments can buckle, only transmitting contractile forces to the surrounding medium. b) If adhesive sites are present, the severing of network elements due to buckling will be enhanced, disallowing transitions into overall contractile networks states. Image from [128], Copyright 2012 National Academy of Sciences.

experiments have shown contractile mechanisms independent of myosin II activity, such as cytokinesis [17] and tumor cell migration [11]. We believe these mechanisms must also be considered because buckling behavior has not been resolved in a cell, as also mentioned in a review by Koenderink et al. [88]. But how could contraction

without motors occur? Walcott and Sun recently proposed in a continuum model and Langevin simulations that passive actin bundles could produce force against an external constraint by harnessing the free energy of cross-linker binding between filaments [200]. This gives a thermodynamic drive towards overlapped filament states by the enthalpic contribution of cross-linker binding. In a similar mechanism driven by passive motion, Lansky et al. showed *in vitro* that diffusing cross-linkers in between microtubule networks can produce overlap formation because of entropic expansion in the overlap region [101]. Johann et al. also performed stochastic modeling of this overlap region showing the regions of stability when considering passive and active diffusing cross-links [81]. To the best of our knowledge no researchers have yet considered the consequence of these passive force generating mechanisms in driving contraction in actomyosin networks. Figure 1.5 describes this contractile mechanism based on cross-linker confined entropic expansion.

## 1.3 Outline of chapters

Clearly the accurate representation of actomyosin network and their key emergent contractile processes is challenging due to a number of factors as we have presented. Not only is the complexity in size and geometry of such an assembly overwhelming, each protein in the network is undergoing spatially resolved chemical processes that have intricate mechanical consequence. This includes nano-scale mechanochemical dynamics of semi-flexible actin filaments, regulatory proteins, and molecular motors. We believe it is necessary to fill a niche with regard to this prob-

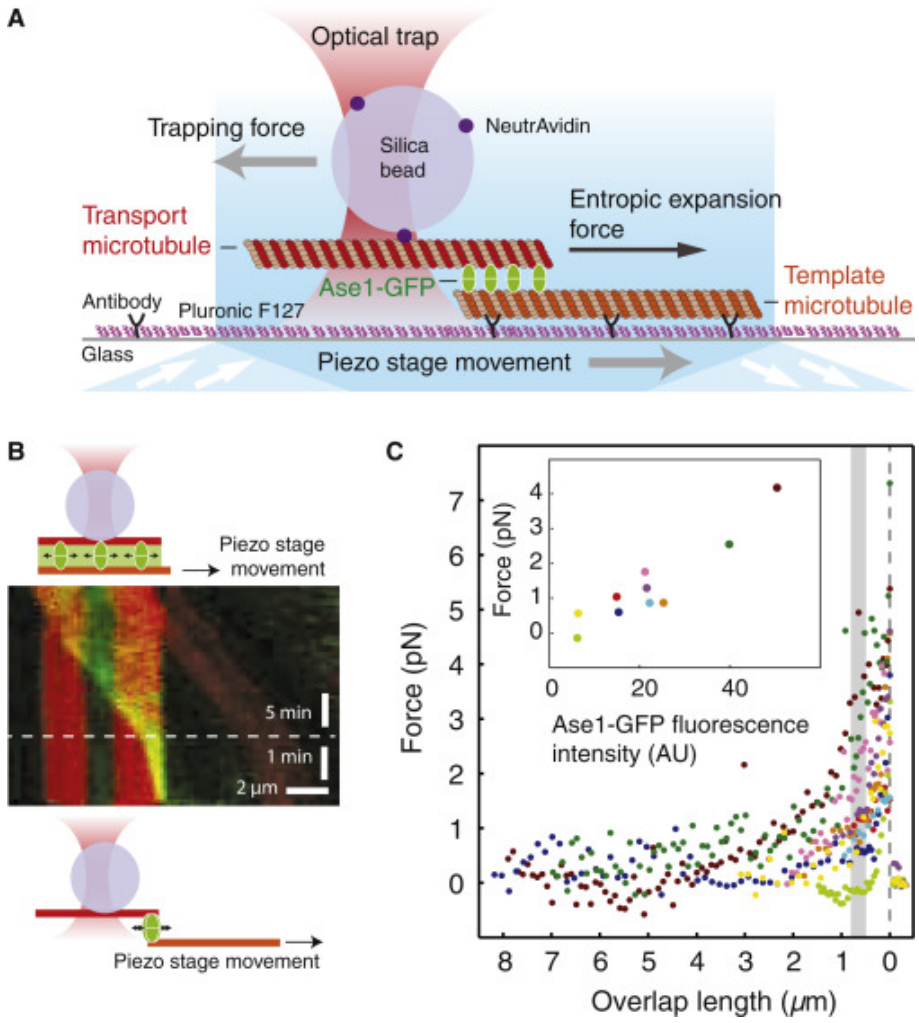


Figure 1.5: In Lansky et al., microtubule cross-linking proteins Ase1 were shown to produce overlap increase in two microtubules when confined between them. This can be explained by the ability of cross-linkers to diffuse between binding sites on the microtubules, producing an entropically driven force similar to an adiabatic expansion of an ideal gas against a piston. a) Forces were measured between microtubule filaments using a optical tweezer assay with Ase1 and Kinesin-14 motors. The optical trap setup can measure the force created by diffusive cross-linking between a connected microtubule and another template microtubule on a cover slip. b) An image of the flourescently labeled Ase1 cros-linkers in green diffusing between microtubules in red. c) Force produced on the optical trap by cross-linker diffusion is highly overlap-dependent - low overlaps experience large forces by the entropic expansion mechanism. Reprinted from [101] with permission from Elsevier.

lem - to have a high-resolution structural modeling framework which includes a minimally-complete set of spatially resolved cytoskeletal chemistries and regulatory proteins and efficiently describes mechanical deformations of the filamentous network under stresses generated by molecular motors. With this in mind in Chapter 2 we create an efficient framework to fulfill those requirements, as well as focus on the modeling required for a non-muscle actomyosin assembly. By doing so we deeply couple mechanics and chemistry at high spatial resolution while also allowing for high-performance simulations at $\mu m$ length scales. We hope to show this approach can open doors to modeling many types cytoskeletal assemblies, including actomyosin, microtubule-motor networks and even intermediate filaments. At the end of Chapter 2, a benchmarking study of contractile actomyosin is performed, highlighting the rich dynamic behaviors of a network when considering mechanochemical dynamics such as actin filament turnover and variations in cross-linking and motor concentration.

From a biophysics perspective, the emergence of contractility in disordered networks of actin filaments and myosin II motors has not been investigated at the molecular level, considering the energetic contribution and dynamics of passive cross-linking could provide networks with the symmetry breaking mechanism necessary for actin filament aggregation. So, in this thesis we show the effect of cross-linker induced energy landscapes on actin filaments in contractile actomyosin networks, utilizing the functionality of the developed computational model and other approaches. First a separate actomyosin force dipole model interacting with cross-linking and motor molecules is derived in Chapter 3, elucidating a dipole ratcheting mechanism

where cross-linkers can stabilize transient myosin II motions to produce many $pN$ of force against external tethers. This phenomenon utilizes a thermodynamically derived behavior of passive cross-linker binding to pairwise actin filaments. Then, moving to large simulations of disordered actomyosin networks in Chapter 4, we map the phase diagram of possible contractile behaviors, including tethered tension generation as well as untethered geometric collapse of a network, and their dependence on cross-linking and motor driving. In this we show that both contractility mechanisms are dependent on the cross-linker landscape derived in Chapter 3. This developed understanding of contractility has uncovered an alternative mechanism independent of the typical sarcomeric muscle organization and instead dependent on a passive energy landscape created by short-range cross-linking molecules binding to actin filaments. We believe this adds to the number of ways non-muscle actomyosin can contract and provides a new perspective of the molecular tools available to the cytoskeleton to perform biological function.

# Chapter 2: Developing *MEDYAN*: Mechanochemical Dynamics of Active Networks

*This chapter and its figures are adapted from: Konstantin Popov*, James Komianos* and Garegin Papoian. "MEDYAN - Mechanochemical Simulations of Contraction and Polarity Alignment in Actomyosin Networks". **PLOS Comp. Bio.** 12, e1004877 (2016) *co-first author*

## 2.1 A need for *mechanochemical* simulations of the cytoskeleton

The cytoskeleton is a dynamic chemical network of actin filaments, microtubules, and intermediate filaments that are controlled by a diverse collection of regulatory proteins. As mentioned previously, these networks are essential for many large-scale biological processes, including embryonic development, wound healing, and immune response [2]. The dynamic nature of the cytoskeleton allows the cell to respond to both chemical and mechanical cues, providing complex feedback mechanisms for growth and remodeling. Using molecular motors, the cytoskeleton can harness energy from ATP hydrolysis, converting it into mechanical work that can drive the system into configurations not possible with thermal motion alone. Along with the inherent nature of cytoskeletal filaments, which can assemble or disassemble rapidly due to chemical species gradients or regulatory signaling cascades, this

energy consumption allows the cytoskeleton to dynamically respond to a range of extracellular stimuli on varying timescales.

Despite this complexity, much progress has been made in recent years in modeling active networks, and in particular the cell cytoskeleton. Chemical models ranging from deterministic, ordinary differential equation as well as partial differential equation approaches describing reaction-diffusion processes [44, 66, 115, 122], to Monte Carlo approaches that rely on spatially resolved stochastic simulation [6, 25, 51, 207] have been used to reproduce the spatial concentration distributions and chemical dynamics of cytoskeletal networks in *in vivo* and *in vitro*. Separately, multi-scale, coarse-grained mechanical models of the cytoskeleton with limited chemical detail have been created to study its viscoelastic properties [33,37,87], growth and remodeling [132,184,186], as well as interactions with a cell membrane and surfaces [8,28,47]. Recently, models have been developed to investigate the active nature of cytoskeletal networks, and can reproduce many of the dynamic mechanisms involved in actomyosin contractility [39, 82, 102, 137, 181, 205]. Some hybrid models have begun to incorporate multiple aspects of cytoskeletal chemistry and molecular transport with network mechanics [3, 78, 124, 136], providing insight to the importance of this coupling in modeling and simulation.

However, we believe that a desirable platform for mechanochemical simulations of cytoskeletal dynamics at high structural resolution should contain the following capabilities: A) Spatially-resolved stochastic chemistry within the cytosol, the filamentous network, and between them, which would allow the establishment of global and local chemical gradients and heterogeneities, taking the fundamentally

stochastic nature of chemical reactions into account. B) A sufficiently rich set of filament chemical reactions that includes (de)polymerization processes, (de)branching, formin-based nucleation and capping, monomer aging via ATP or GTP hydrolysis, severing, cross-linker and molecular motor (un)binding, and molecular motor walking, which would enable the simulation of minimally complete cytoskeletal chemistries. C) An accurate, yet computationally efficient mechanical force field, which would allow computing the deformations of a connected filamentous network that is being continuously deformed by force-generating proteins, such as myosins, as well as other chemical reaction events. D) A deep coupling between chemistry and mechanics, where, for example, the chemical heterogeneity of individual monomers in a filament due to aging leads to the corresponding spatial modulation of bending stiffness along the chain, hence, correctly localizing buckling transitions. In the supplemental portion of our published work [148], we have compiled a salient selection of current agent-based approaches for modeling cytoskeletal dynamics. To the best of our knowledge, most of the individual capabilities listed above (A-D), needed to enable next generation of structural modeling, are absent in the currently existing or prior methods [3, 19, 36–38, 82, 85–87, 102, 124, 125, 131, 132, 136, 181, 202]. Furthermore, it would be most useful to the community if the source codes for these modeling frameworks were publicly available, which is again not the case for most, but not all [3, 124], modeling frameworks listed in Section **??**. In yet another challenge, apart from the computational complexity in combining these cytoskeletal aspects, there is a need to achieve computational efficiency of scaling up simulations to micron length scales, where most interesting cytoskeletal phenomena take place,

while still retaining locally high structural resolution at nanometer scale.

With the above considerations, we introduce the *Mechanochemical Dynamics of Active Networks* (*MEDYAN*) model which contains all of the aforementioned capabilities. While explicitly accounting for the complex chemical dynamics of polymers and the molecular transport of chemical species in an active network using a stochastic reaction-diffusion scheme, based on a spatially resolved Gillespie algorithm, a new coarse-grained representation and set of force fields for semi-flexible polymers has been developed, including complementary force fields for polymer branching molecules, cross-linking molecules, and molecular motors. The model also allows for mechanochemical coupling of any of these molecules, producing a full treatment of active network mechanochemistry where mechanical stresses influence chemical rate constants, allowing the modeling of Brownian ratchets, slip-bonds, catch-bonds, or more complex biphasic mechanochemical feedbacks. With this model, the complex and non-linear mechanochemical properties of active networks can be studied in full detail with efficiency, and can give insight to many active networks, including the cell cytoskeleton and other biological and artificial polymer ensembles.

Although the stochastic reaction-diffusion scheme of MEDYAN follows prior efforts from out laboratory [77, 78, 100, 210–212], in this work we have added significant new capabilities, including several new chemical reactions and their related mechanical elements, as well as a greatly accelerated stochastic reaction-diffusion algorithm for sparse reaction networks. But, perhaps a larger problem in cytoskeletal modeling has been the rigorous yet computationally efficient modeling of polymer

mechanics in network at micron scales or above. This fundamental problem goes beyond cytoskeletal simulations and concerns many other semi-rigid polymeric melts or assembles, where there is a large discrepancy between the polymer's persistent length and its diameter. A coarse-grained approach, based on representing polymer segments as cylinders which contain a number of monomeric units, is a natural way to address this problem. However, the difficulty is in enforcing the non-crossing constrain among the chains, where prior steric potentials were conceptually simple, but are non-analytic [87], or analytic but computationally highly inefficient in the case of large aspect ratio of polymer chain segments [60], raising serious concerns in many practical situations. In this work, we introduce a rigorous, fully analytic and computationally efficient excluded volume potential that solves this problem, enabling efficient simulations of melts of networks comprised of semi-flexible polymer chains with large aspect ratios at micron scales.

In this chapter, we first introduce both the chemical reaction-diffusion and mechanical models used in MEDYAN, while also highlighting the coupling of both parts and how they work together to provide a full mechanochemical treatment of an active network. Then, to explore the capabilities of this model and its publicly available software implementation (available at www.medyan.org), we investigate a contractile actomyosin network containing actin filaments, $\alpha$-actinin cross-linking proteins, and non-muscle myosin IIA mini-filaments, demonstrating the propensity for rich dynamical remodeling of these networks, as their mechanochemistry is tuned by varying myosin II and cross-linker concentrations. Our simulations indicate a clear threshold of cross-linker concentration which induces contractile behavior of

actin filaments by myosin II mini-filaments in a smaller $1 \times 1 \times 1\ \mu m^3$ actomyosin system, as well as other distinct network morphology changes. In particular, our analyses clearly indicate that in all simulated systems actin filaments tend not only geometrically align, but, surprisingly, this alignment is unipolar (emerging from an initially random, disordered network). We further found that both this polarity alignment and contractile behavior are tightly regulated by the extent of actin filament turnover, producing biphasic super-diffusive motions of individual actin fibers driven by myosin II mini-filament force generating activity. We also discuss myosin II mini-filament force-dependent accumulation in these systems, as all simulated concentration configurations and system sizes produce this accumulation in areas of high network stress, spontaneously generating concentration gradients in the solution phase. In a larger $3 \times 3 \times 3\ \mu m^3$ actomyosin system, we observed a distinct alignment, contraction and polarity sorting, reminiscent of arc formation in the rear of a lamellipodium.

## 2.2 The proposed model

### 2.2.1 Chemical reaction-diffusion representation

The cell cytoskeleton, as well as other active networks, takes advantage of distinct chemical phenomena which allows the network to grow and remodel based on extracellular signaling and other chemical cues [62, 174]. In order to model the complex chemical interactions that occur in these dynamic networks at a microscopic resolution, the *MEDYAN* model uses a stochastic reaction-diffusion scheme

based on a three dimensional, spatially resolved Gillespie algorithm [64, 65] as in previous works [77, 78, 100, 210–212]. With simulation space divided into compartments, with compartment size chosen based on the so-called "Kuramoto length" of the reaction-diffusion system of interest [83, 99] (see Section A.3.1 for an example determination of a Kuramoto length), diffusion and other transport events of chemical species, which could include active transport via molecular motors or convective transport such as retrograde flow, are modeled as stochastic jumps between compartments that can be directionally biased or unbiased in order to model various transport mechanisms. This allows for a discrete and spatially resolved treatment of small copy numbers and non-uniform concentration gradients, which could produce substantial and important fluctuations in chemical dynamics at the nanoscale. In particular, recent works have studied the significant effects of these stochastic fluctuations on filopodial growth [100, 211] as well as the effects of active transport phenomena and its significance in both lamellipodia and filopodia formation and sustainability [78, 210, 212]. In these systems, the concentration of G-actin monomers as well as other cytosolic molecules fluctuates greatly across the spatial domain of the protrusion due to both diffusion and active transport mechanisms, producing non-linear chemical response and signaling. These important effects could not be captured with deterministic approaches, which ignore the cytoskeleton's biologically inherent stochasticity.

In the *MEDYAN* model, we have developed the stochastic reaction-diffusion scheme further such that one can use varying types of stochastic simulation algorithms in order to optimize a simulation based on the chemical properties of the

simulated network. While the original Gillespie algorithm is an efficient and exact alternative to solving a chemical master equation [64, 65], with the chemical master equation being nearly impossible to solve for the complexity of systems we are considering, optimized methods have been developed for the original Gillespie *direct method* to decrease computational complexity for loosely-coupled chemical reaction networks, as reviewed by Cao et al. [27]. In particular, the *next reaction method*, developed by Gibson and Bruck [63], makes use of clever data structures to optimize the propensity updating process after each reaction is executed, producing massive speed-ups for sparse reaction-diffusion networks compared to the original algorithm. The *MEDYAN* model can make use of either of these algorithms depending on the type of chemical system to be simulated. In most cases, the latter is more suitable for simulating most active networks, where the chemical reactions across the system are sparse and spatially localized by compartments. With these algorithm optimizations, the computational complexity for stochastically simulating active network evolution is greatly reduced, allowing the model to surpass timescales accessible with the original Gillespie schemes. The *MEDYAN* software implementation, which is discussed in Section A.1.4, is also designed such that such that new stochastic simulation algorithms can easily be included in the existing reaction-diffusion framework, including the *optimized direct method* [27] and *partial propensity methods* [149, 150]. For a detailed benchmarking of the currently implemented optimizations in systems similar to the ones simulated in Section 2.3, see Section A.5.1.

In order to account for the chemical heterogeneity of active network polymers,

we represent them in the model as a distinct arrangement of chemical monomers that are overlayed onto the existing reaction-diffusion compartment grid, which allows them to undergo spatially resolved reactions with diffusing chemical species besides typical polymerization and depolymerization events. This can be of importance to network dynamics in the case of actin filaments, where polymerized actin hydrolyzes ATP, giving rise to a substantial change in polymerization kinetics at both ends of the filament [57, 177]. In conjunction with hydrolysis, the cytoskeletal regulatory protein ADF/Cofilin can sever actin filaments preferentially where ATP has been hydrolyzed [7, 14]. Together, and along with other chemical interactions in the cytoskeleton, these reactions are responsible for the actin filament turnover process observed in most types of cellular protrusions [147]. With the *MEDYAN* polymer representation, these important molecular processes can be included in the reaction-diffusion master equation (RDME) and simulated in full detail.

We have also included detailed cross-linker chemical dynamics to the model. It has been well known that cross-linking molecules are important for producing the observed morphology of the actin cytoskeleton *in vivo* [59, 198], but most existing cytoskeletal models do not include the stochastic binding and unbinding of cross-linkers to actin filaments in the simulation space. In the *MEDYAN* model, cross-linker binding reactions with neighboring polymers are dynamically added; if two separate polymer binding sites are within a specified range in a given compartment, an unbound cross-linker species in that compartment can bind to them. An unbinding reaction is also associated with that molecule once bound, which can then release it from both polymers. This dynamic addition of reactions allows for compu-

tational efficiency as well as an exact, spatially resolved treatment of cross-linking molecules, which can be essential for active network evolution.

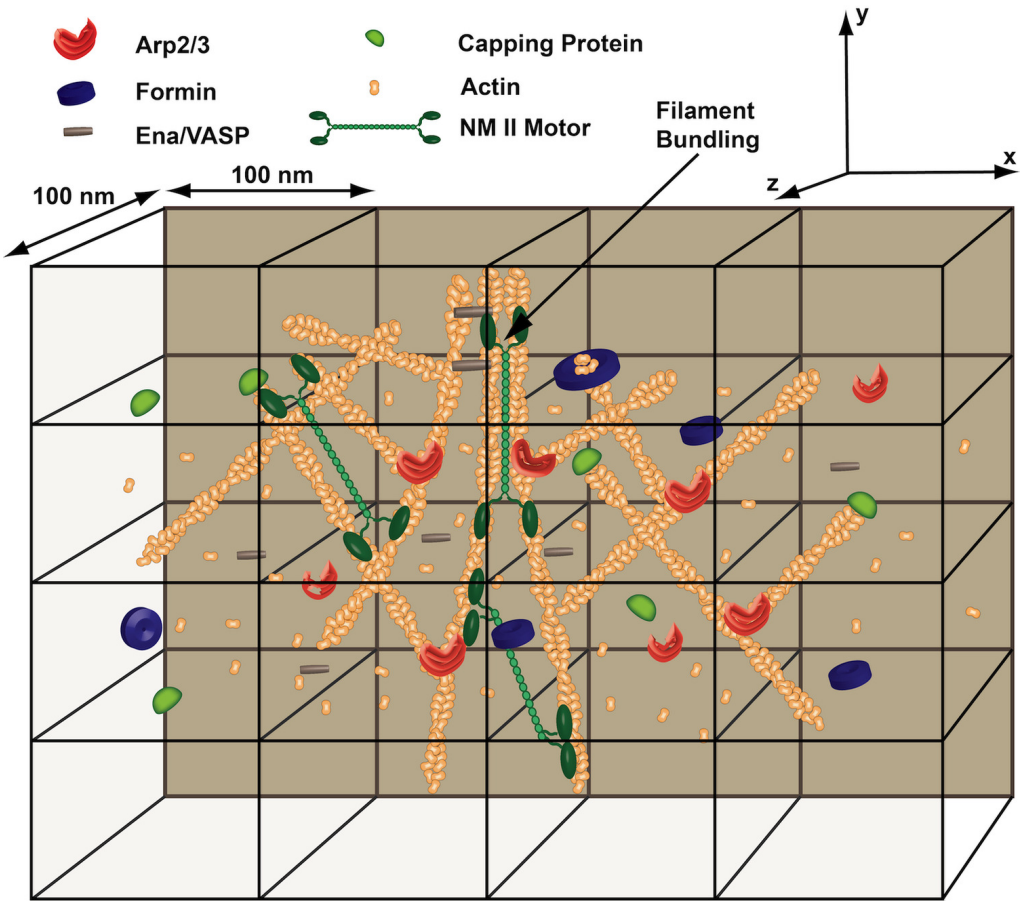


Figure 2.1: A complex cytoskeletal network can be simulated with *MEDYAN's* stochastic reaction-diffusion scheme based on well-mixed compartment volumes. Chemical reactivity and diffusion will cause complex and spatially resolved network evolution, such as the process of actin filament bundling. See Section A.1.1 for a more detailed description of all chemical reactions that can be included in a simulation. From [148].

In order to make a simulated network active, we have introduced molecular motors in the model – molecules which utilize energy released due to chemical reactions in the system and transfer it into mechanical work. For example, in cytoskeletal networks, energy from ATP hydrolysis is used by number of protein species to generate forces. In particular, the non-muscle myosin II (NMII) motor family plays a

significant role in cytoskeletal remodeling and cell motility [75, 192], where individual NMII motors assemble into larger bipolar filaments that can reach hundreds of nanometers in length [94]. The *MEDYAN* model can include bipolar NMII filaments that, in a similar manner to cross-linking molecules, can bind onto two neighboring actin filaments. The slow diffusion of these larger molecules may produce some spatial diffusion error on a compartment grid, and hybrid combinations of Brownian dynamics and stochastic reaction-diffusion models have been introduced in recent years [53] as a way to solve this error, which could be included in the *MEDYAN* model in the future. But, we believe for grids used in Section 2.3 which are 500 $nm$ in length, this is still a good estimate of true diffusive behavior. When bound, the head ensembles can make stochastic directional steps towards the barbed end of either filament, which generates "sliding" forces in the network, promoting reorganization and contractility.

In a *MEDYAN* simulation, a transport event or polymer-related reaction is chosen to occur by the stochastic simulation algorithm based on its reaction propensity. This process repeats, advancing the chemical reaction-diffusion system in time. Bulk reactions can also be included between diffusing species, allowing for even more complex chemical evolution. See Section A.1.1 for a more detailed description of the entire set of chemical reactions that can be simulated. With the stochastic reaction-diffusion scheme and polymer representation described, complex active networks can be simulated with explicit and detailed chemical interactions and molecular transport. Fig 2.1 shows a cartoon depiction of a cytoskeletal network that could be simulated with the MEDYAN model. All molecules can diffuse throughout the sim-

ulation space according to their specified diffusion rate and the chosen compartment size. Actin filaments can grow and shrink due to the polymerization and depolymerization of G-actin monomers, as well as the binding and unbinding of capping proteins and formins, and Arp2/3 can nucleate new actin filaments on existing filaments at a $70^o$ angle [23]. Lastly, cross-linking proteins can bind and unbind to actin filaments, and NMII mini-filaments can bind, unbind, and walk along actin filaments.

### 2.2.2 Semi-flexible polymer model

To complement the detailed stochastic reaction-diffusion scheme described above, we have developed a new set of force fields in the *MEDYAN* model to account for the mechanical properties of an active network. In previous work [77, 78], a simple bead-spring model was used to describe actin filament mechanics, where a single filament was regarded as a composition of hard-core beads. These beads represented individual monomers which were then connected by either a harmonic or more complex potential. This method, while being a detailed and robust description, required the calculation of a large number of interactions between neighboring beads during a mechanical equilibration of the system. Considering that a cubic micron of a cytoskeletal network could contain on the order of $10^6$ actin monomers, mechanical equilibration of a system with this simple model would severely limit simulation timescales that could be accessed.

In order to overcome these computational limitations, we are introducing in

this work a polymer model based on elongated cylindrical monomer segments for simulating semi-flexible polymers with a persistence length, denoted as $l_p$, that is much larger than its diameter $\sigma_0$ (i.e. very large aspect ratio, $l_p >> \sigma_0$). Cylinders have been previously introduced in various coarse-grained computational models for the description of systems containing elongated objects, including the modeling of viscoelastic actin networks [87] and hydrodynamics of suspensions [164, 172]. Here we would like to emphasize that cylinders in the *MEDYAN* description are not considered as collections of beads, but rather as stiff weightless springs of diameter $\sigma_0$, connecting its end points. This fact, as it will be seen later, will help us to build up a rather intuitive mathematical formalism to describe polymer mechanics. Fig 2.2 represents the scheme of using cylinders as monomer units in a polymer chain. This assumption makes the model applicable for the description of most biopolymers (in the case of actin filaments, $l_p/\sigma_0 \approx 10^3$), and while force-generating molecular motors could significantly change the correlation between two points along the polymer chain, these correlation lengths will still be significantly larger than the distance between two neighboring monomers in previously used bead-spring model. Moreover, the new model can describe flexible molecules as well, as a standard bead-spring model can be considered as a limit with $l_p \to \sigma_0$. For a detailed benchmarking of this coarse-graining scheme in systems similar to the ones simulated in Section 2.3, see Section A.5.2.

We now introduce the interaction potentials used in the *MEDYAN* model. We note that the *MEDYAN* software implementation can easily be modified to include different types of potentials for the interactions presented below. For example, a

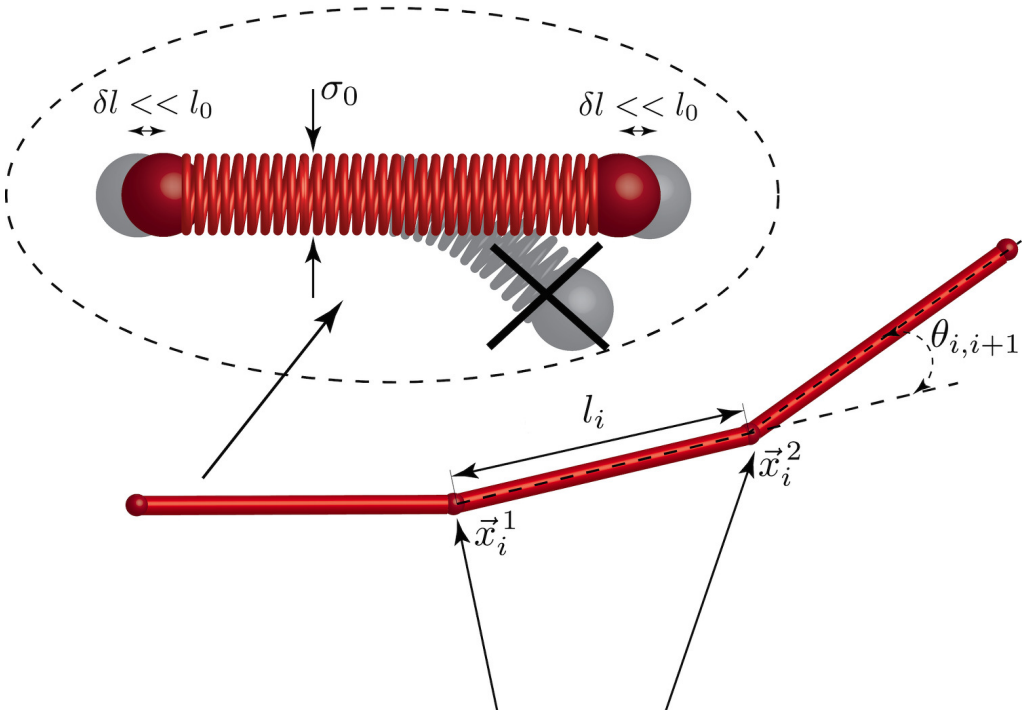


Figure 2.2: A cylinder based scheme is used in the *MEDYAN* force fields to model semi-flexible polymers. Here, $\sigma_0$ is the diameter of the cylinder and $l_0$ is the equilibrium length, where $l_0 >> \sigma_0$. We assume that axial deformations of the cylinders are small and radial deformations are forbidden. From [148].

finitely extensible nonlinear elastic (FENE) potential could be easily added to the existing code for less elastic semi-flexible polymers, molecular motors, and cross-linkers [30]. Other forms of polymer excluded volume effects could also be included.

We assume that every coarse-grained monomer segment is represented by a cylinder with a finite thickness $\sigma_0$ and equilibrium length $l_0$, as shown in Fig 2.2. To account for filament bending, we use an angular potential between consecutive cylinders in the polymer chain, written as

$$U_i^{bend} = \varepsilon_{bend} \left[1 - \cos\left(\theta_{i,i+1}\right)\right], \tag{2.1}$$

where $\theta_{i,i+1}$ is the angle between two consecutive cylinders $i$ and $i+1$ along the

polymer chain, and $\varepsilon_{bend}$ is the bending energy, which can be chosen based on the persistence length of the simulated polymer.

Cylinders also can be slightly stretched or compressed along their main axis, while radial deformations within the cylinder are not allowed. To illustrate this fact we draw springs inside of the cylinders in Fig 2.2. The stretching energy corresponding to deformations of the $i^{th}$ cylinder can be represented as

$$U_i^{str} = \frac{1}{2} K_{str} \left( |\mathbf{l}_i| - l_0 \right)^2 , \tag{2.2}$$

where $\mathbf{l}_i = \mathbf{x}_i^2 - \mathbf{x}_i^1$ is the vector connecting the endpoints of the $i^{th}$ cylinder, and $K_{str}$ is the stretching constant. As in the bending potential, this constant, along with the equilibrium length, $l_0$, can be chosen depending on the elastic modulus of the simulated polymer. In the case of actin filaments, these bending and stretching potentials allow the model to capture non-linear deformations reported by various studies [84, 108, 121]; with $U_i^{bend}$ accounting for the thermal elasticity of the chain, $U_i^{str}$ describes elastic deformations of the chain stretched beyond its entropically driven elastic limit [114]. These deformations are considered to have high energy penalties, which is reflected in high values of $K_{str}$, therefore, can occur only under very large global deformations of the system.

There are several common approaches usually used to calculate excluded volume interactions between two aspherical elongated particles, which are cylinders in our case. The most obvious approach is to represent the elongated particles as a collection of spheres; with this representation, interactions are simply calculated as

a sum of pairwise hardcore repulsions between the spheres forming each cylinder. While this is a very simple and straightforward method, it defeats all purpose and efficiency of the initial cylindrical coarse-graining. Another widely used approach is to use the Gay-Berne potential to describe excluded volume interactions between interacting cylinders [13, 60], which can be used as a part of the LAMMPS [143] package. This potential, however, has limited applicability and lower computational efficiency when $l_p >> \sigma_0$ as in the case of most biopolymers. On top of that, computational complexity of this potential is also increased greatly due to constantly finding the distance of closest approach between the two cylinders, which is a very costly calculation. Finally, another method was used in the model of Kim et al. [87] which calculates cylindrical repulsive interactions using the closest distance between two interacting segments. This force is then transferred to the end points of the segments, based on the lever rule as well as the position of the point of closest approach. Despite the elegance of this method, we found several drawbacks for using this approach in the *MEDYAN* model: from a computational point of view, algorithms for calculating the point and the distance of closest approach between neighboring cylinders contains costly control flow as mentioned previously, increasing computational complexity for this approach greatly. From a mathematical and physical point of view, a lack of a continuous and analytical function for this closest distance puts limitations on the resulting force calculations, which might lead to oscillations and divergence during mechanical equilibration of the system.

In order to overcome these issues, we introduce a novel approach for calculating excluded volume interactions between two cylinders. This approach is conceptually

similar to early mentioned devision the cylinders into small point-like subunits and calculating interactions between them. However, instead of an actual representation of the cylinders as a collection of subparticles, we solve this analytically by writing a pair potential between two infinitely small fragments on both cylinders and then integrating this pair potential over the length of both cylinders.

The potential of excluded volume interactions between two cylindrical units on neighboring polymers, denoted as $i$ and $j$, can be given by:

$$U_{ij}^{vol} = \int_{l_i,l_j} \delta U(|\mathbf{r}_i - \mathbf{r}_j|) dl_i dl_j. \tag{2.3}$$

Here, $\delta U(|\mathbf{r}_i - \mathbf{r}_j|)$ is the above mentioned pair potential between two points located on the two interacting cylinders $i$ and $j$ as shown in Fig 2.3a. For pure excluded volume repulsion, we have chosen $\delta U(|\mathbf{r}_i - \mathbf{r}_j|) = 1/|\mathbf{r}_i - \mathbf{r}_j|^4$. This provides a steep enough function to mimic cylindrical hard core repulsion, while allowing the integrals in Eq 2.3 to be evaluated analytically. This allows us to derive analytical expression for the forces acting on the end points of the cylinders $i$ and $j$. For every arbitrary point on a given cylinder $i$ we can write the parametric equation $\mathbf{r}_i = \mathbf{x}_i^1 + t(\mathbf{x}_i^2 - \mathbf{x}_i^1)$, where $\mathbf{x}_i^1$ and $\mathbf{x}_i^2$ are coordinates of the beginning and the end of cylinder $i$, respectively, and $t \in [0, 1]$ is a parameter. Taking this into account, and writing a similar parametric equation for cylinder $j$, Eq 2.3 can be written as

$$U_{ij}^{vol} = K_{vol} \int_0^1 \int_0^1 \frac{dsdt}{|\mathbf{r}_i(\mathbf{x}_i^1, \mathbf{x}_i^2, t) - \mathbf{r}_j(\mathbf{x}_j^1, \mathbf{x}_j^2, s)|^4}, \tag{2.4}$$

where $K_{vol}$ is a constant determining the strength of repulsion.

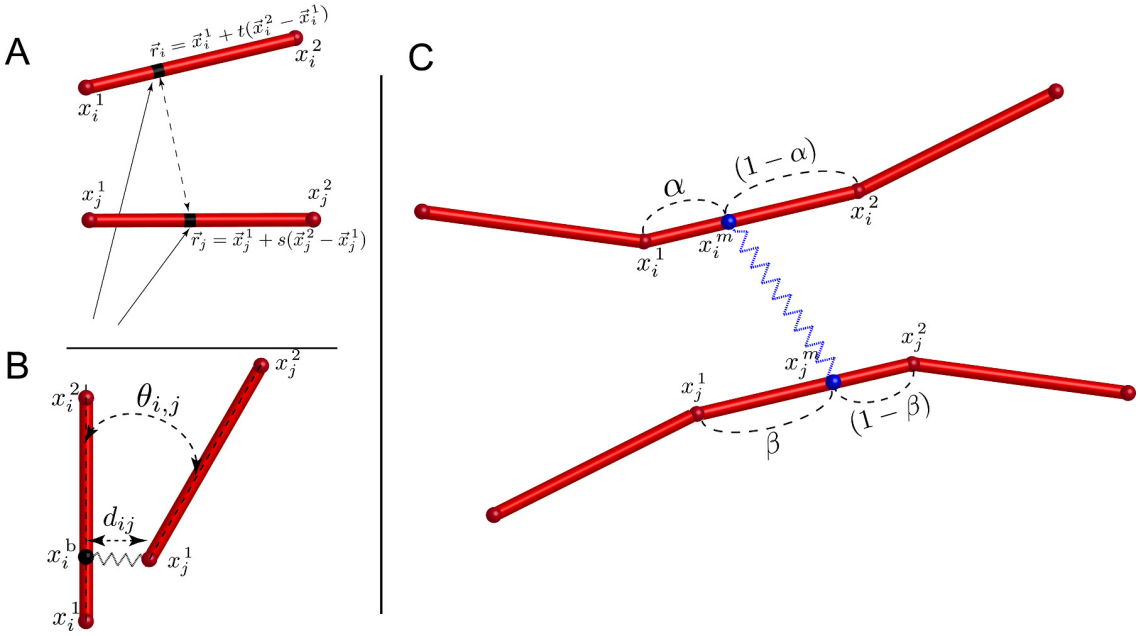


Figure 2.3: a) A Schematic representation of two arbitrary points on the cylinders $i$ and $j$, used to calculate excluded volume interactions. b) Representation of branching points. Position of the branching point $\mathbf{x}_i^b$ on the "mother" filament is determined by a stochastic chemical reaction. c) Representation of the motor as a potential between two points $\mathbf{x}_i^m$ and $\mathbf{x}_j^m$ on bound cylinders. Positions of the binding points $\alpha$ and $\beta$ are determined by stochastic chemical reactions. From [148].

The *MEDYAN* model accounts for the process of polymer nucleation by branching. See Section 2.2.1 section for a more detailed description of branching nucleation events. We introduce the following potential to describe the mechanical interactions of branched polymers, as seen in Fig 2.3b:

$$U_{ij}^{branch} = U_{ij}^{branch,str} + U_{ij}^{branch,ang} + U_{ij}^{branch,dihed}, \tag{2.5}$$

where this interaction regards cylinder $i$ as being on the "mother" polymer and cylinder $j$ as the "daughter" or branched polymer.

The first term in Eq 2.5, which is a potential securing cylinder $j$ to a branching point on cylinder $i$, can be written as

$$U_{ij}^{branch,str} = K_{branch,str} \left( |d_{ij}| - d_0 \right)^2 , \tag{2.6}$$

where $\mathbf{d}_{ij} = \mathbf{x}_j^1 - \mathbf{x}_i^b$ is the distance between branching point on the cylinder $i$, $\mathbf{x}_i^b$, and the end point of the cylinder $j$, $\mathbf{x}_j^1$, $d_0$ is the equilibrium value for this distance, and $K_{branch,str}$ is the stretching constant that can be chosen depending on the stiffness of the simulated branching molecule. As it was noted previously, we assume that axial deformation of the cylinders are small, and radial deformations are prohibited. In this case we can describe position of any branching point on the cylinder in terms of a scalar value $\gamma \in [0, 1]$, which represents a fractional position of the branching point $\mathbf{x}_i^b$ with respect to end points of the cylinder $\mathbf{x}_i^1$ and $\mathbf{x}_i^2$, $\mathbf{x}_i^b = (1 - \gamma)\mathbf{x}_i^1 + \gamma \mathbf{x}_i^2$. In other words, $\gamma$ will be generated as the result of a chemical branching event and will not depend on the stress generated in the branching junction.

The second term in Eq 2.5 describes an angular potential at the chosen branching point between cylinders $i$ and $j$:

$$U_{ij}^{branch,ang} = \varepsilon_{branch,ang} \left[ 1 - \cos \left( \theta_{i,j} - \theta_0 \right) \right] , \tag{2.7}$$

where $\theta_0$ is the equilibrium value of the branching angle, $\theta_{i,j}$ is the angle between cylinders $i$ and $j$, and $\varepsilon_{branch,ang}$ is the angular bending energy, which can be chosen based on the flexural rigidity of the branching molecule. In case of actin filaments, Arp2/3 grows nucleated filaments at an equilibrium angle $\theta_0 \approx 70^o$ to the mother filament [23].

Finally, the last term in Eq 2.5 describes a dihedral potential between cylinders $i$ and $j$, which uses the dihedral angle between two planes, formed by the points $(x_i^2, x_i^b, x_j^1)$ and $(x_i^b, x_j^1, x_j^2)$:

$$U_{ij}^{branch,dihed} = \varepsilon_{branch,dihed}\left[1 - \cos\left(\phi_{i,j} - \phi_0\right)\right], \tag{2.8}$$

where

$$\phi_{i,j} = \arccos(\mathbf{n}_i \cdot \mathbf{n}_j),\ \mathbf{n}_i = \frac{\left[(\mathbf{x}_i^2 - \mathbf{x}_i^b) \times \mathbf{d}_{ij}\right]}{|(\mathbf{x}_i^2 - \mathbf{x}_i^b)|\,|\mathbf{d}_{ij}|},\ \textit{and}\ \mathbf{n}_j = \frac{[\mathbf{l}_j \times \mathbf{d}_{ij}]}{|\mathbf{l}_j|\,|\mathbf{d}_{ij}|}. \tag{2.9}$$

The symbols ( $\cdot$ ) and [ $\times$ ] stand for scalar and vector product, respectively, and $\varepsilon_{branch,dihed}$ represents the dihedral bending energy between the two cylinders, which can be chosen in a similar manner to $\varepsilon_{branch,ang}$.

The *MEDYAN* model incorporates molecular motors into the network as a dynamic object which can bind onto neighboring cylinders $i$ and $j$ at the positions $\mathbf{x}_i^m$ and $\mathbf{x}_j^m$, and create a mechanical bond, as shown in Fig 2.3c. See Section 2.2.1 for more description of motor binding and walking events. For computational efficiency in studies of global deformations in large active networks under the force generation of small molecular motor ensembles, an implicit representation for molecular motors has been developed in which the motor is represented as a single potential acting on two neighboring cylinders. In the case of modeling myosin II mini-filaments, which are small ensembles of 10-30 myosin heads aligned in a bipolar fashion [189], this is an excellent approximation. In future studies, a more explicit implementation of molecular motors, comprised of connected monomer units, can be implemented to allow a more detailed and accurate description of myosin II filaments at the cost

of computational efficiency. This explicit representation may be of importance in studies including myosin II thick filaments, which can contain on the order of 100-800 motor heads [182], thus allowing the ensemble to bind to a large number of actin filaments simultaneously.

To describe the stretching energy of a bond created by an implicit motor, we introduce the following harmonic potential:

$$U_{ij}^{motor} = \frac{1}{2} K_{motor} \left( |\mathbf{l}_{ij}^{m}| - l_0^m \right)^2, f \tag{2.10}$$

where $\mathbf{l}_{ij}^{m} = \mathbf{x}_j^m - \mathbf{x}_i^m$ is the instantaneous length of the motor, $l_0^m$ is the equilibrium length of the particular motor, and $K_{motor}$ is the stretching constant, which can be chosen based on the stiffness of molecular motor to be simulated.

The binding position of the motor head $\mathbf{x}_i^m$ on cylinder $i$ can be expressed as $\mathbf{x}_i^m = (1-\alpha)\mathbf{x}_i^1 + \alpha \mathbf{x}_i^2$ where $\alpha \in [0,1]$. Here, similar to the case of the branching potential in Eq 2.6, we assume that $\alpha$ is a scalar parameter, which does not change during mechanical minimization and is determined by a stochastic chemical event. Using this representation along with a similar expression for the binding position on cylinder $j$, we can write $\mathbf{l}_{ij}^m$ as

$$\mathbf{l}_{ij}^m = (1-\beta)\mathbf{x}_j^1 + \beta \mathbf{x}_j^2 - (1-\alpha)\mathbf{x}_i^1 - \alpha \mathbf{x}_i^2. \tag{2.11}$$

where $\beta \in [0,1]$ represents the fractional position on cylinder $j$. As the result of chemical reactions, $\alpha$ and $\beta$ can stochastically change, which results in motor head relocation and the generation of new mechanical stresses in the system.

Similarly, passive cross-linkers are represented using the potential in Eq 2.10, but with time-independent values of $\alpha$ and $\beta$. In a similar manner to molecular motors, by not explicitly introducing new classes of interactions for these molecules, but instead using analytically computed energies and forces between neighboring cylinders connected by passive cross-linkers (i.e. relying on an implicit mechanical representation), the *MEDYAN* model can achieve much higher computational efficiency in the simulation of large active networks with these molecules.

System boundaries in *MEDYAN* are modeled as non-deformable shells with a number of possible shapes, including cubic, spherical, and capsule geometries. These boundaries sterically repel approaching polymer segments, keeping the simulated network confined in the chosen domain. One of the possible potentials used to describe the interaction between the $i^{th}$ cylinder and the boundary can be written as:

$$U_i^{boundary} = \varepsilon_{boundary}\, e^{-\mathbf{d_i}/\lambda}, \tag{2.12}$$

where $\lambda$ is the screening length and $\mathbf{d_i}$ is the distance between the boundary and the closest endpoint of the $i^{th}$ cylinder, $\mathbf{x}_i^2$ or $\mathbf{x}_i^1$. $\varepsilon_{boundary}$ represents the repulsive energy provided by the boundary.

The total energy of the system $U^{tot}$, assuming all corresponding species were chemically generated, is equal to a sum of the above contributions. This energy is then used in the *MEDYAN* model to mechanically equilibrate the system after a number of stochastic chemical reaction-diffusion steps. In order to perform this equi-

libration efficiently, most methods require analytical expressions for the derivatives of the energy with respect to cylinder position, *e.g.* forces in Langevin dynamics or gradient directions in conjugate gradient methods. Note that all terms in $U^{tot}$ (Eqs 2.1 - 2.12) but Eqs 2.6 to 2.10 are initially written in terms of the end points of the cylinders; so, derivatives of those terms can be taken with respect to $\mathbf{x}^1$ and $\mathbf{x}^2$ such that, if using "force" terminology, will give forces acting on these end points of the cylinders. Eqs 2.6 to 2.10 also include coordinates of points located on the cylinders somewhere in between its end points: branching position on the "mother" filament in Eqs 2.6 to 2.8 and motor or cross-linker head positions in Eq 2.10. However, as it was discussed before, for every point $m$ along cylinder $i$ we can write $\mathbf{x}_i^m = (1-\alpha)\mathbf{x}_i^1 + \alpha\mathbf{x}_i^2$, where $\alpha \in [0,1]$ does not depend on the coordinates of the cylinder end points or stresses in the system during a mechanical equilibration. Taking this into account, Eqs 2.6 to 2.10 can be rewritten only in terms of positions of cylinder end points. Therefore, these potentials can be differentiated with respect to only $\mathbf{x}^1$ and $\mathbf{x}^2$. This assumption follows under the condition of small axial deformations of the cylinders and the absence of radial deformations within each cylinder (see Fig 2.2), appropriate for relatively stiff filaments, such as F-actin and many other biological and artificial polymers. Very soft polymers, on the other hand, would be more profitably modeled as comprising of spherical beads and not cylinders. Mathematically speaking, this is equivalent to a simple chain rule:

$$\frac{\partial U^i}{\partial \mathbf{x}_i^m} = (1-\alpha)\frac{\partial U^i}{\partial \mathbf{x}_i^1} + \alpha\frac{\partial U^i}{\partial \mathbf{x}_i^2}. \tag{2.13}$$

From a mechanical point of view, this is equivalent to transferring of a force applied at a point $\mathbf{x}_i^m$ to cylinder end points according to a lever rule, which was also used in [87]. Hence, to compute instantaneous forces needed for mechanical energy minimization in a system with the interaction potentials introduced in this section, we only need to calculate

$$\frac{\partial U^{tot}}{\partial \mathbf{x}_i^1}, \ and \ \frac{\partial U^{tot}}{\partial \mathbf{x}_i^2}, \tag{2.14}$$

where the notation $\frac{\partial}{\partial \mathbf{x}} = \{\frac{\partial}{\partial x_x}, \frac{\partial}{\partial x_y}, \frac{\partial}{\partial x_z}\}$ represents the gradient in the direction of $\mathbf{x}$. This formalism allows us to calculate not only point-like interactions that can be described by a lever rule, but also more complex interactions, where the level cannot be applied, as in the case of our newly introduced cylindrical excluded volume potential (Eq. 2.3). With these forces, an energy minimization is performed using a conjugate gradient method in the current *MEDYAN* software implementation, and is designed such that optimized minimization methods can be easily added to the existing code; see Section A.1.4 for more description.

### 2.2.3 Mechanochemical coupling and simulation protocol

In a *MEDYAN* simulation, the chemical and mechanical models work in tandem to evolve an active network in time. Fig 2.4 shows the general flow of the entire *MEDYAN* trajectory, where timescale separation of slower chemically-driven force generation and faster local force relaxation in a simulated active network allows for an iterative switching between stochastic chemical simulation and mechanical equilibration. After the stochastic simulation algorithm executes a set number of

chemical steps to evolve the network in time, some of which have mechanical effects that drive the network slightly out of mechanical equilibrium, the energy of the network will be minimized according to the force fields specified in the simulation. By performing highly efficient chemical stochastic simulation coupled with coarse-grained semi-flexible polymer chain mechanics, active network simulations with the *MEDYAN* model can reach time and length scales not accessible by its preceding models [77, 78] with this high level of resolution in both aspects of stochastic reaction-diffusion and coarse-grained polymer chain mechanics.

The above-stated iterative simulation protocol assumes that the mechanical subsystem is always near equilibrium, adiabatically following the slow chemical dynamics at all incremental time points during a simulation of an active network evolution. This is a valid approximation in the case of typical actin cytoskeletal networks undergoing small, localized force deformations, as evidenced by the recent microrheology experiment of Falzone et al. [50]. Their measurements of the relaxation time of various mesh-sized deformations in an actin filament network indicated an upper limit of approximately 10 milliseconds, which is significantly faster compared to the the walking rate of non-muscle myosin II motors [96] or actin filament growth rates [57] under physiological concentrations. While this timescale separation holds for most cytoskeletal networks undergoing typical molecular motor or filament growth-induced deformations, ones with slower network stress relaxation, possibly due to larger-scale network deformations or very fast reaction-diffusion processes, or if thermal motions need to be studied for other reasons, may be better served with a Langevin thermal dynamics approach at the cost of significantly re-

duced computational efficiency. In the latter case, the mechanical subsystem will evolve under constant time step Langevin dynamics, where it may be then more convenient to evolve the reaction-diffusion subsystem employing one of the multi-particle RDME methods [153,154] instead of a variable time-step algorithm such as the next subvolume approach used in the current work.

We also allow for the explicit coupling of both separate chemical and mechanical entities such that one can simulate the mechanochemical feedbacks of an active network. Many molecules in active networks, and in particular the cell cytoskeleton, have distinct mechanochemical properties that can greatly affect overall network dynamics and morphology [113,197]. *MEDYAN* allows for a detailed treatment of these relationships by dynamically updating reaction rates based on a reacting molecule's evolving stresses, and any form of mechanochemical effect can be included in the model. Once the system is mechanically equilibrated following a number of chemical steps, reaction rates are updated based on newly formed mechanical deformations as shown in Fig 2.4. With chemical, mechanical, and molecular transport properties of an active network being treated on equal footing, as well as their coupling being explicitly accounted for, the *MEDYAN* model allows simulations of various active networks with great mechanochemical detail and efficiency.

### 2.2.4 Publicly available software package

The MEDYAN model has been implemented in a C++ software package which uses efficient data structures and object-oriented programming paradigms to simu-

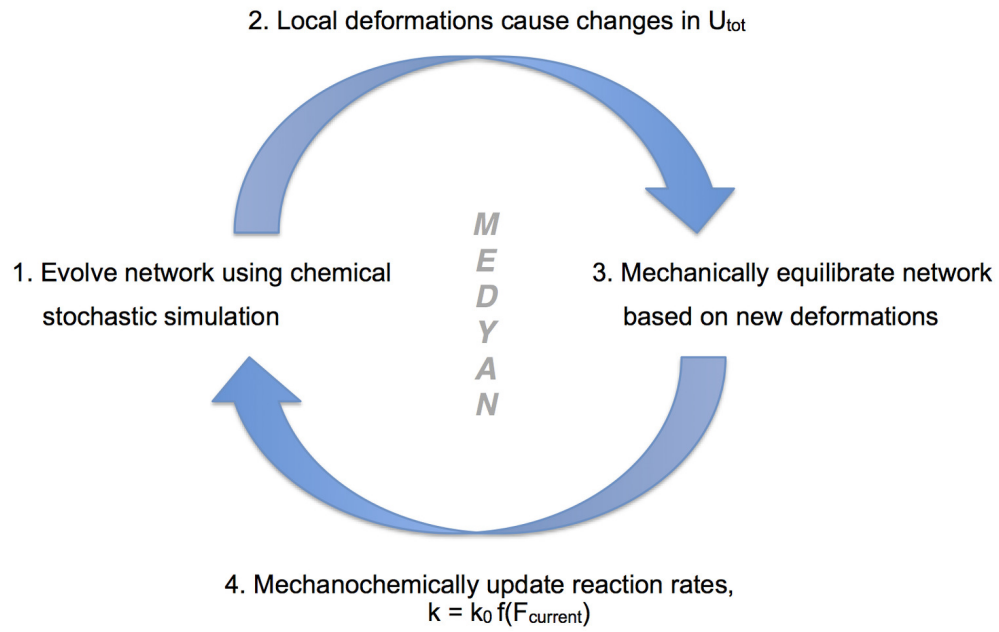


Figure 2.4: The flow of the simulation is as follows: (1) After the chemical stochastic simulation evolves the network in time and (2) local deformations are formed, (3) a mechanical equilibration is performed and (4) reaction rates are updated according to chosen functional forms $f(F_{current})$ where $F_{current}$ is the force on that reacting molecule after equilibration. From [148].

late active networks with the scheme described in the earlier sections. The package has the capability for the user to specify the geometric, chemical, and mechanical properties of the simulated active network in a number of system input files, making the code robust and flexible enough to perform simulations for a range of active matter systems. This package, along with documentation on usage and compilation, as well as a visualization tool, is publicly available for use, modification, and addition of new patches (www.medyan.org). See Section A.1.4 for a more detailed description of the software implementation.

## 2.3 A first investigation of actomyosin contractility

We relied on the the capabilities of the *MEDYAN* model to investigate the the effects of NMIIA and $\alpha$-actinin concentration on the morphological and contractile properties of both a smaller $1 \times 1 \times 1$ $\mu m^3$ and larger $3 \times 3 \times 3$ $\mu m^3$ sized cubic actomyosin network. Simulations were performed for a number of actomyosin systems with varying molar concentration ratios of both NMIIA and $\alpha$-actinin relative to a fixed overall actin concentration, denoted as $R_{m:a}$ and $R_{\alpha:a}$, respectively. We observed the distinct morphological changes in the network that come with varying these concentrations. We also discuss below our quantitative and qualitative observations about overall network contractility under various conditions and modeling assumptions, as well as actin filament bundling and phase transitions into these bundles.

The simulated actomyosin systems are comprised of actin filaments that are coarse-grained into cylindrical segments. Using harmonic potentials to represent the stretching and bending response under stress, F-actin filaments can be displaced when acted on by an external force due to NMIIA or an external boundary. Filamentous force constants were chosen based on the known persistence length and elastic modulus of actin filaments [91, 138]. Chemically, the filaments can polymerize and depolymerize with diffusing actin monomers at either end at specified rates determined experimentally [57]. These events increase or decrease the filament length by 2.7 $nm$, correspondingly [173]. To include the mechanochemistry of actin polymerization, we describe the polymerization rate change of a filament tip under external

load with the Brownian Ratchet model as in previous works [141], as elaborated in Section A.4. Binding events that can occur on the actin filament will be described in more detail below, and we assume there is one binding site per 27 $nm$ of actin filament, which can be dually occupied by $\alpha$-actinin and NMIIA mini-filaments. We will discuss in a later part of this section the implications of this modeling decision and the consequences of introducing a mutual site exclusion of the cross-linkers and molecular motors.

The simulated actomyosin systems contain diffusing NMIIA mini-filaments that are assumed to contain 10-30 individual myosin heads [189] with each having an individual step size of $d_{step} = 6\ nm$ [196]. While we do not account for the explicit binding and walking of separate subunits to actin filaments in the ensemble, we have adopted the results of the Parallel Cluster Model of Erdmann et al. [49] to describe, in a coarse-grained fashion, the binding, unbinding, and walking of small ensembles of NMIIA motors in a similar manner to [85]. This model is fully mechanochemical and contains relationships for all reaction events in terms of the mechanical force acting on the mini-filament. See Section A.4.1 for a detailed derivation of adopting the results of the Parallel Cluster Model to our coarse-grained description. When a NMIIA mini-filament stochastically binds to neighboring actin filaments within a distance of $200 \pm 25\ nm$, which was chosen based on the known length of NMII mini-filaments [144], it creates a harmonic potential, where the force constant for this potential has been chosen based on single molecule pulling experiments [196]. The walking of these head ensembles along filaments then can produce mechanical stress due to this potential, which actively remodels the actin network. The systems also

contain diffusing $\alpha$-actinin which can stochastically bind, and unbind to neighboring actin filaments within $35 \pm 5$ $nm$, which was chosen based on the known length of $\alpha$-actinin [118]. When bound, the cross-linker creates a harmonic potential with force constant found in single molecule pulling experiments [42]. To model the mechanochemical effects of pulling forces on $\alpha$-actinin, a simple slip bond form was used; see Section A.4.2 for more description on this mechanochemical model.

For each concentration configuration presented in the following sections, omitting the larger systems which will be presented later, 2000 $s$ of simulation were run in a $1 \times 1 \times 1$ $\mu m^3$ cubic spatial boudary with a hard-wall potential at an actin concentration of 20 $\mu M$. The simulations all initially nucleate 50 short actin filaments at random positions and orientations, then grow them for 10 $s$ in the presence of $20 \mu m$ diffusing G-actin and $\alpha$-actinin. Subsequently, diffusing NMIIA mini-filaments are added to the system. While the average actin filament length in these simulations is 0.8 $\mu m$, which may be shorter than the average actin filament length observed in vivo [190], this filament length is of relevance to the remodeling of lamellipodial and lamellar actin fragments by myosin II and cross-linking proteins. These fragments have been observed to be of lengths ranging from 0.5 to 2 $\mu m$ in the lamellipodium under various conditions [162]. Sixteen trajectories were run for each actomyosin configuration, and all shown results are averaged over those trajectories.

### 2.3.1 Network contractility controlled by presence of NMII and $\alpha$-actinin

Fig 2.5 shows a single trajectory snapshot of an actomyosin system simulation containing actin filaments, NMIIA mini-filaments, $\alpha$-actinin, and the constituent diffusing species within the simulation boundary. To quantify overall contractile behavior of the various actomyosin systems, we define an actomyosin network radius of gyration using all coarse-grained actin filament cylinder segments in the network:

$$R_g = \sqrt{\frac{1}{n}\sum_{i=0}^{n}(\mathbf{r}_i - \mathbf{r}_{GC}) \cdot (\mathbf{r}_i - \mathbf{r}_{GC})}, \tag{2.15}$$

where $\mathbf{r}_{GC}$ is the geometric center of the ensemble of cylinders, $\mathbf{r}_i$ is the position of the $i^{th}$ cylinder, and $n$ denotes the number of cylinders in the network. This is a more useful measure for our system than other more macroscopic measurements, including contractile velocity and minimum enclosing spherical volume. This is due to the fact that the dynamics of most networks studied do not show an obvious volume contraction, but do reorganize rapidly into contractile structures.

Fig 2.6a shows a heat map of actomyosin network $R_g$ for the various systems after 2000 $s$ of network evolution. We observe patterns in agreement with [4, 12], including a decreased $R_g$ for increasing NMIIA concentration, which implies more contractile behavior with this increase. We also observe the same effect of decreasing $R_g$ for increasing $\alpha$-actinin concentration. More motors can provide more contractile force and linkers aid this contraction by increasing the transmitted force length

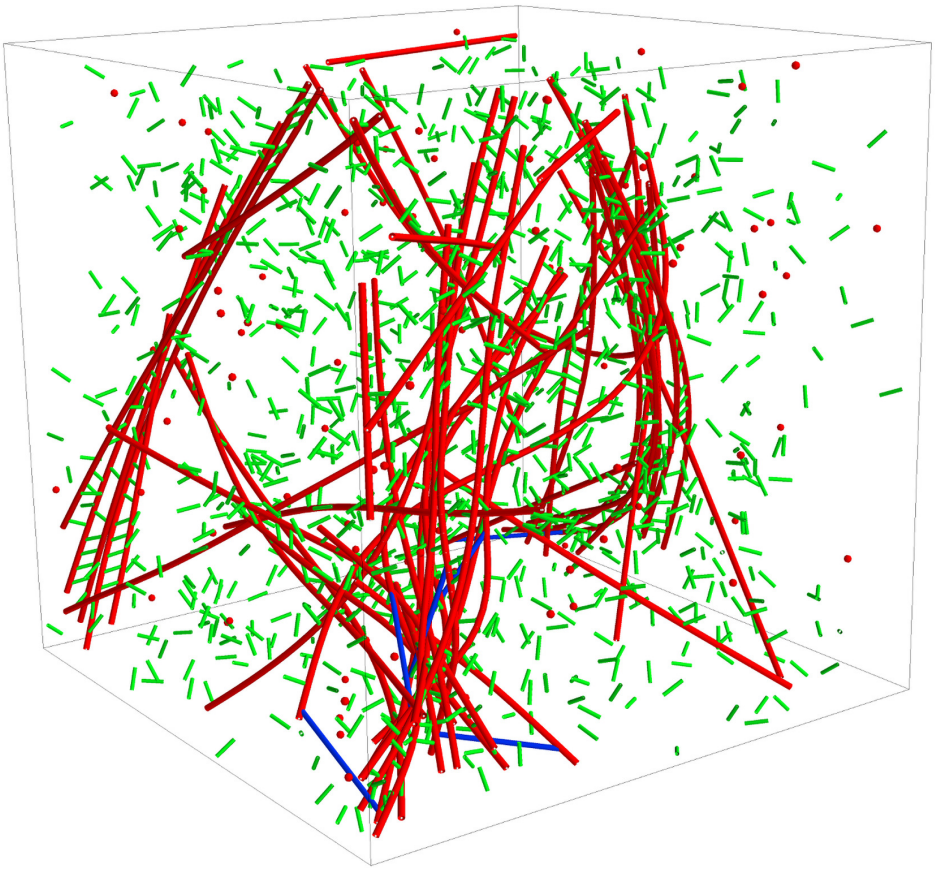

Figure 2.5: A single trajectory snapshot of a $1 \times 1 \times 1$ $\mu m^3$ actomyosin system simulation at $R_{\alpha:a} = 0.1$ and $R_{m:a} = 0.01$ after 2000 $s$ of network evolution. Actin filaments are represented as red connected cylinders, $\alpha$-actinin are represented as green cylinders, and NMIIA mini-filaments are represented as blue cylinders. The corresponding diffusing species are also shown in the same colors. The system is bounded by a cubic, hard-wall potential. From [148].

scale. Fig 2.6b shows the network morphology for various values of $R_{\alpha:a}$ as $R_{m:a}$. We observe that for the lowest value of $R_{\alpha:a} = 0.01$, there is very little reorganization and contractile structure formation from the original randomly oriented network. But, with $R_{\alpha:a}$ values of 0.1 and 0.5, there is very apparent actin filament bundle formation. Increases in $R_{m:a}$ throughout the systems tends to slightly increase the network's ability to contract into more tightly packed structures, as was also indicated by the values of $R_g$ in Fig 2.6.

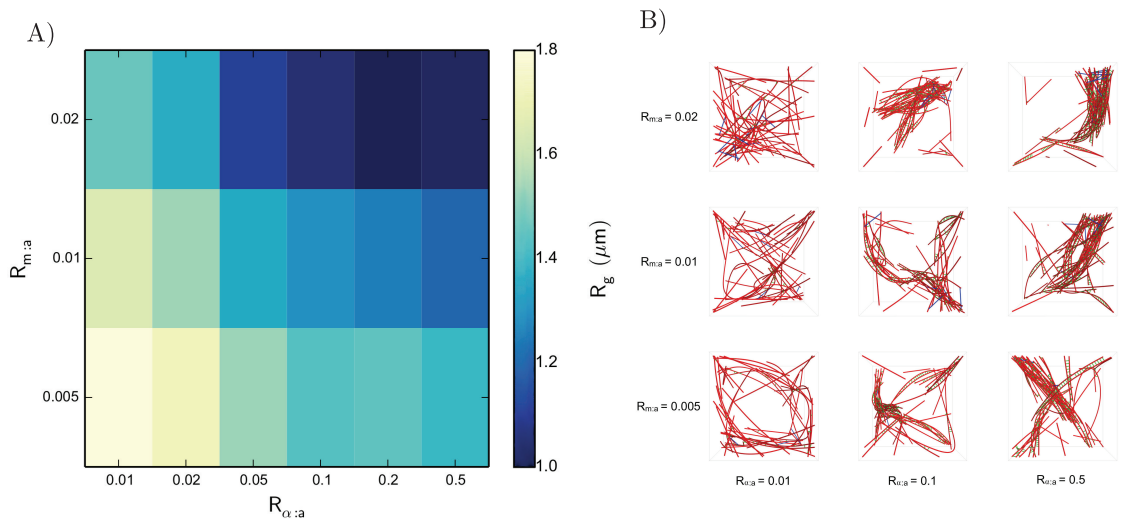


Figure 2.6: a) A heat map of actomyosin network $R_g$ as a function of $R_{m:a}$ and $R_{\alpha:a}$ after 2000 $s$ of network evolution. As NMIIA and $\alpha$-actinin concentrations are increased, a very apparent correlation in overall network contraction results. b) Single trajectory snapshots of the actomyosin systems with various concentrations of $R_{\alpha:a}$ and $R_{m:a}$ after 2000 $s$ of network evolution. These snapshots are shown without diffusing species for simplicity. For increasing $\alpha$-actinin and NMIIA concentration, actin filament bundle formation is increasingly more apparent. From [148].

### 2.3.2 Switch-like transition to contraction regulated by cross-linking

Since the final network $R_g$ does depend on the initial configuration of the randomly oriented network, especially for non-contracted networks, it is useful to look at the ratio of final $R_g$ after 2000 $s$ to initial configuration $R_g$ for the various systems, denoted as $R_{g,f}/R_{g,i}$. Figure 2.7 shows this value for a range of systems, holding $R_{m:a}$ fixed, over the 2000 $s$ of simulation time. We see that there is a clear divergence in time evolution for the lowest $R_{\alpha:a}$ values compared to the other higher values. This may imply, coupled with morphology observations of the various trajectories as in Figs. 2.6b, that there is not a continuous distribution of achievable contractile structures accessible with a given $R_{\alpha:a}$ and $R_{m:a}$ as implied by Fig 2.6,

but only at a certain minimum $\alpha$-actinin concentration, actin filament bundle formation is possible. This also seems likely due to the fact that the systems with $R_{\alpha:a}$ values of 0.1, 0.2, and 0.5 converge to a similar $R_g$ value after the entire simulation. Comparing this observation to other systems with different $R_{m:a}$, we see that as motor concentration is increased, the minimum $\alpha$-actinin concentration for actin filament bundle formation decreases, possibly due to the increased contractile strength of adding more NMIIA mini-filaments to the system.

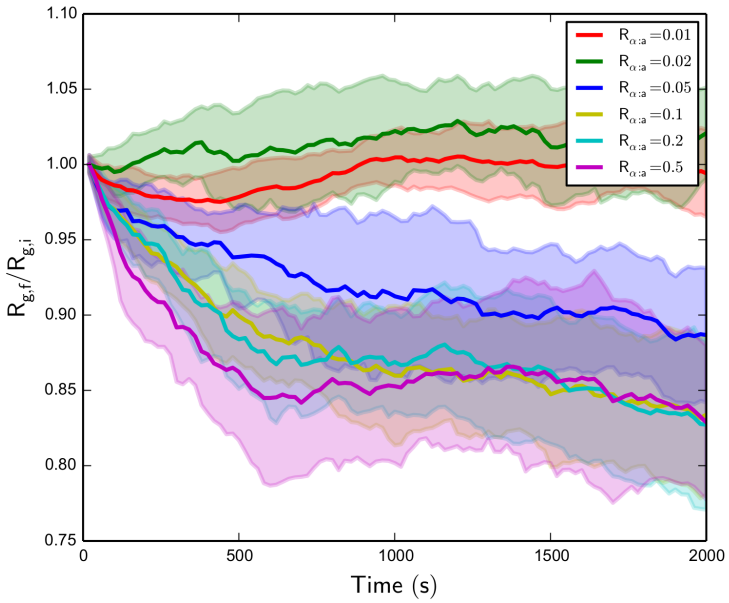


Figure 2.7: $R_{g,f}/R_{g,i}$ over time for various $R_{\alpha:a}$ with fixed $R_{m:a} = 0.01$. We see that above a threshold $\alpha$-actinin concentration, contraction is observed, and the time of bundle formation for these contractile structure formations decreases with increasing $\alpha$-actinin concentration. Standard deviations of the $R_{g,f}/R_{g,i}$ values over all trajectories are shaded. From [148].

From these observations, we deduce that in these systems, actomyosin system cross-linker concentration is a switch-like mechanism that controls a transition between disordered and bundled networks, with system motor concentration widening this contractile structure formation regime, thus decreasing the minimum cross-

linker concentration needed for bundle formation and contraction in general. This result is in agreement with the predictions of cross-linker percolation theory in larger scale actomyosin networks [4,205]. The formation of bundles agrees with the zippering mechanism of actin filament alignment and myosin II aggregation as proposed by Verkhovsky et al. [188,189], as long as sufficient cross-linking is present. We will quantitatively investigate this phenomenon in the later chapters.

### 2.3.3 Actin filament polarity alignment by motors is regulated by filament turnover

Other interesting morphological properties of the contractile actomyosin networks were observed. Fig 2.8 shows a single trajectory for a smaller actomyosin system with $R_{m:a} = 0.01$ and $R_{\alpha:a} = 0.1$. When we color the plus and minus ends of these filaments with black and white beads in the same trajectory, respectively, we see that the actin filaments within the bundle are globally aligned in polarity. This is an interesting result since the actin filament network started with random orientation within the uniform spatial boundary condition, and has not been predicted by previous models of bundle formation by way of zippering [188, 189], which describe the resulting apolar alignment of actin filaments, but not polarity alignment. The physical origins of this global polarity alignment by NMIIA mini-filaments is unclear from the trajectory videos, but has been observed and analyzed in two-dimensional motility assays [26, 80, 157], as well as been predicted and modeled in one-dimensional actomyosin bundles undergoing polarity sorting [34, 56]. Constant

turnover in the plus end direction of actin filaments most likely causes anti-parallel orientations to be unstable, thus in the long-time limit of our simulations, only parallel bundles survive. But, the observed global contraction implies that NMIIA mini-filaments are driving network dynamics to a globally aligned, contractile state. It is reasonable to assume that combination of these two factors attributes to the observed behavior.

To further quantify actin filament alignment in the simulated actomyosin networks, we define an orientational order parameter $S$ of the system of actin filaments, which is the largest eigenvalue of the ordering tensor $Q$ [161] which is constructed from

$$Q_{\alpha\beta} = \frac{3}{2}(\frac{1}{N}\sum_{i=0}^{N}\mathbf{u}_{i\alpha}\mathbf{u}_{i\beta} - \frac{1}{3}\delta_{\alpha\beta}),\ \textit{where}\ \alpha,\beta = x,y,z. \tag{2.16}$$

The vector $\mathbf{u}_i$ represents the normalized direction of filament $i$ over the $N$ filaments in the system. When $S$ is equal to zero, the filaments in the system are all randomly aligned, and when $S$ equals 1, the filaments are all perfectly aligned, regardless of polarity. To numerically capture the alignment of bent actin filaments, we chose to use a direction vector from minus to plus end of the entire filament, as opposed to a calculation of $S$ using cylindrical filament segments, which may give values corresponding to unaligned networks if an actin filament bundle is aligned but significantly bent in any direction. Fig 2.8 shows $S$ for the various systems after 2000 $s$ of network evolution, as $S$ correlates directly with trends in $R_g$ over the concentration ratios of $R_{m:a}$ and $R_{\alpha:a}$, showing that all actomyosin systems produce

alignment in tandem with contractile structure formation. We also confirmed qualitatively that in all actomyosin systems simulated, regardless of whether the systems eventually produced a single contractile bundle, all actin filament bundles formed consist of uniformly polar filaments, showing that all alignment observed is in fact polarity alignment.

To probe the origins of this polarity alignment behavior which has been shown to be dependent on actin filament turnover in various systems [34, 56, 119], we vary the reaction constants used for polymerization and depolymerization of actin filaments $k_{actin,poly}$ and $k_{actin,depoly}$ at both the plus and minus ends of the filament by a constant factor $\chi$ while keeping $R_{m:a} = 0.02$ and $R_{\alpha:a} = 0.1$ and holding all other parameter values constant. When this turnover factor $\chi$ is varied from 0.125 to 8, as shown in Fig 2.9, resulting in actin filament turnover rates of 0.07 to 4.4 monomers per $s$, distinct changes in network morphology result. At low $\chi$, which corresponds to a very slow actin filament turnover rate, highly contracted networks are formed with little to no overall polarity alignment. In the case of high $\chi$, no global contraction of the networks is observed, but local polarity alignment in small bundles is seen over the trajectories. Interestingly enough, the original parameters ($\chi = 1$) which corresponded to physiological values of actin filament turnover, is the only parameter set to produce both global polarity alignment and contraction. Fig 2.9 shows the resulting network morphologies - low $\chi$ values corresponded to a dense, disordered clump with no polarity alignment, where high $\chi$ corresponded to local polarity alignment but overall disorder.

To investigate further the contraction and alignment dependencies found by

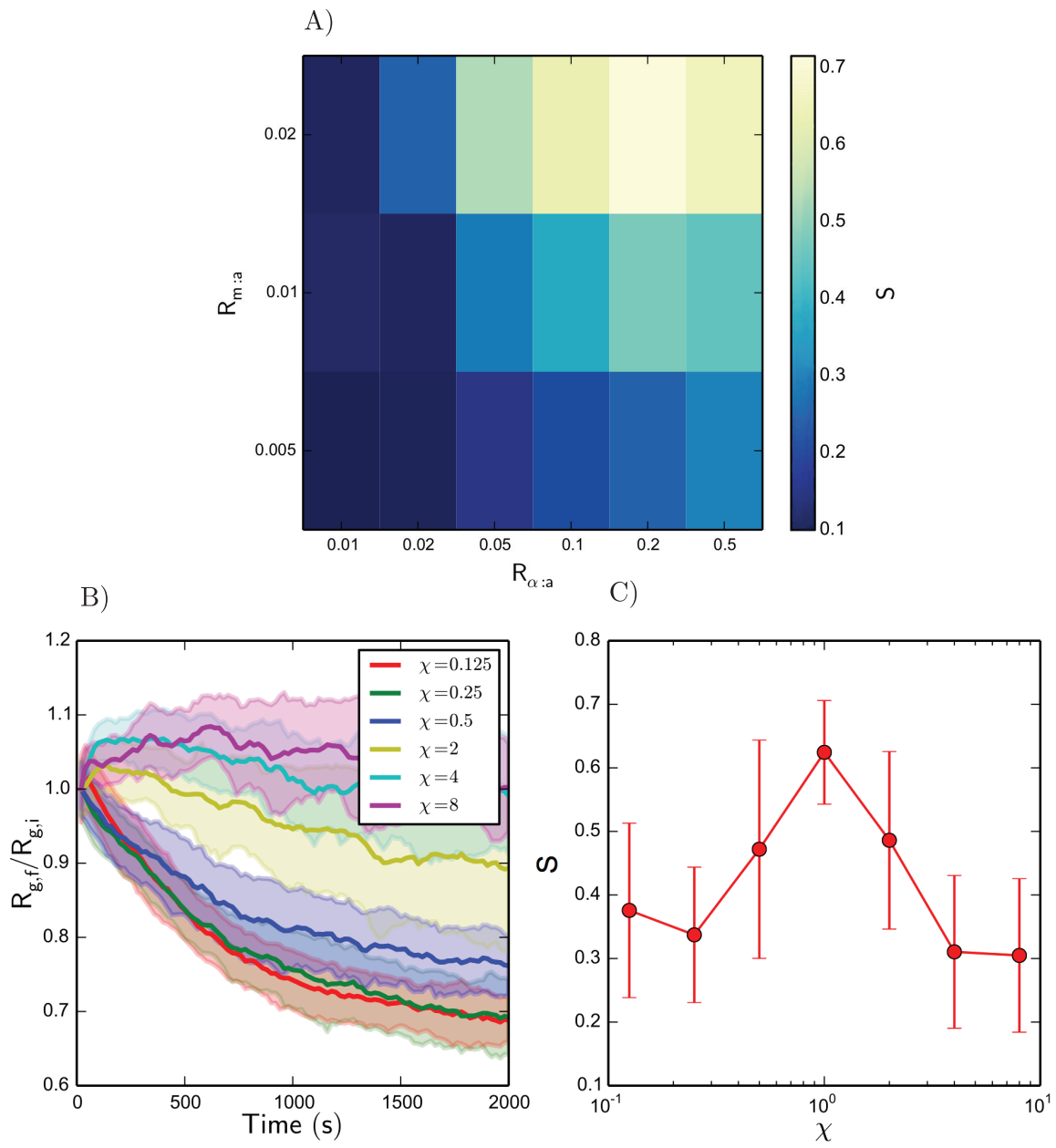


Figure 2.8: a) A heat map of actomyosin network $S$ as a function of $R_{m:a}$ and $R_{\alpha:a}$ after 2000 $s$ of network evolution. As NMIIA and $\alpha$-actinin concentrations are increased, a correlation in alignment results in a similar fashion to $R_g$ in Fig 2.6. b) Actomyosin network $R_{g,f/R_{g,i}}$ and $S$ for various $\chi$. $R_{g,f}/R_{g,i}$ over the 2000 $s$ network evolution for varying values of $\chi$. Contractile behavior increases with decreasing $\chi$. Standard deviations of the $R_{g,f}/R_{g,i}$ values over all trajectories are shaded. c) $S$ after 2000 $s$ of network evolution for varying values of $\chi$. Global alignment peaks around $\chi = 0.5$ to 2, and decreases for values outside of this range. Error bars represent standard deviation of $S$ values over all trajectories. From [148].

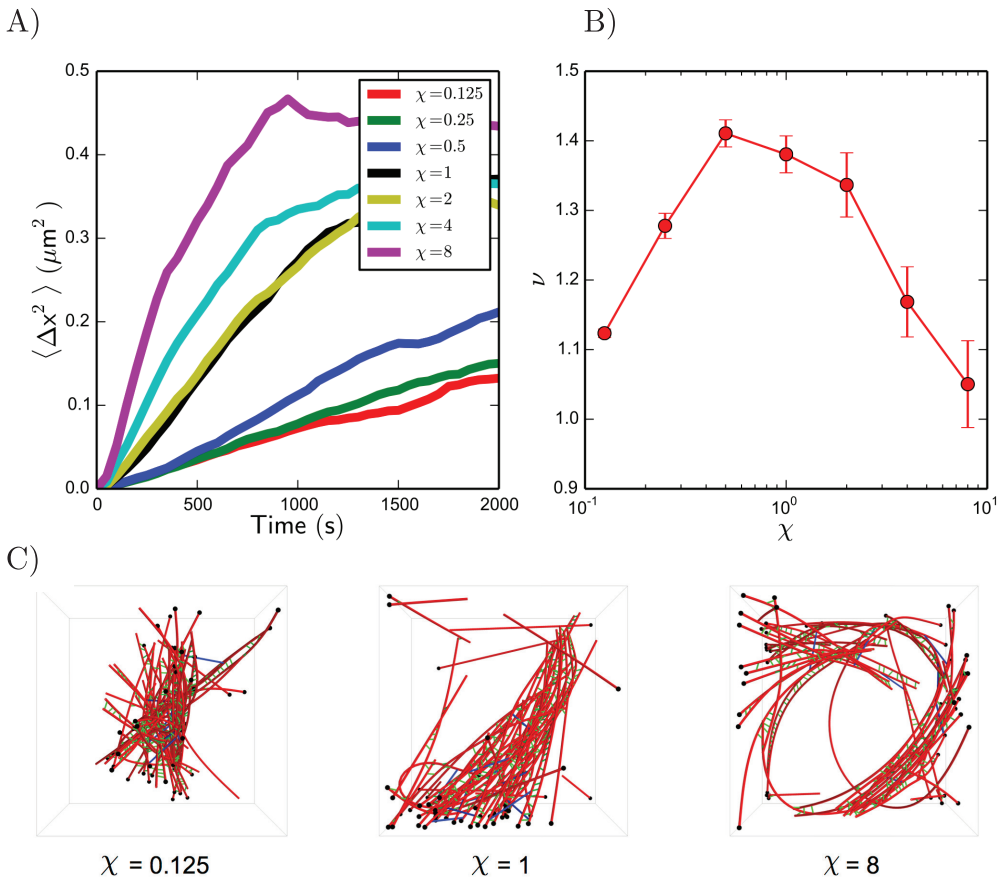


Figure 2.9: a) MSD analysis of actin filaments in simulation. MSD over time for various values of $\chi$. Error bars represent the standard error of the MSD, for each set of trajectories, are smaller than the data points. b) Diffusion exponent $\nu$ acquired from a log-log linear fit of a). Error bars represent the standard linear regression error in $\nu$. c) Single trajectory snapshots of the actomyosin systems, with various values of $\chi$ after 2000 $s$ of network evolution. These trajectories are colored with black and white beads for the plus and minus ends of actin filaments, respectively. From [148].

varying the turnover factor $\chi$, we look at the displacement of actin filaments over the time of the actomyosin system simulations, and compare different actin filament turnover rates to the resulting filament diffusivity. It is important to note that in this simulation context, actin filaments are not diffusing via Brownian motion

in the simulation volume, but are actively moving via actin turnover and NMIIA mini-filament force generation, thus causing a relative displacement of the filament midpoint. Fig 2.9a shows the mean squared displacement (MSD) of actin filament geometric centers, denoted as $\langle \Delta x^2 \rangle$, with respect to simulation time over various $\chi$ values. To describe the motion of filaments under varying turnover rates, we linearly fit the first 1000 $s$ of the MSD (choosing this cutoff due to kinetic arrest and sub-diffusion occurring after this time point, as shown in the sharp turns in MSD plotted against time on a log-log scale to obtain diffusion exponents, following the relation of general, anomalous diffusion:

$$\langle \Delta x^2 \rangle \sim t^{\nu}. \tag{2.17}$$

The exponents $\nu$ corresponding to each turnover factor $\chi$ are shown in Fig 2.9b. All systems exhibited super-diffusion ($\nu > 1$) in the 1000 $s$ interval, which is physically reasonable due to the active nature of the many constituents. Surprisingly, the variation of $\chi$ resulted in a biphasic distribution with a maximum $\nu$ value centered around $\chi = 1$, displaying the same $\chi$ dependence as the $S$ distribution shown in Fig 2.9b. This relationship does make some intuitive sense; in a randomly oriented filament network, a higher-order filament diffusion relationship in any direction would cause anti-parallel filament bundle orientations to be less stable, thus producing a higher fraction of parallel bundles. A physical explanation for the upper regime may be that when $\chi > 1$, actin filament turnover can out-run displacements via NMIIA mini-filament walking, thus not allowing NMIIA remod-

eling at all, and producing locally aligned but globally disordered actin networks. But, as $\chi$ is increased while remaining under the threshold $\chi = 1$, super-diffusive behavior and polarity alignment are apparent; a few studies have suggested actin filament turnover in the same direction of myosin II movement allows myosin II to walk farther on actin filaments, producing more contractile force [29, 137], but this is unlikely in our simulations due to the very short binding lifetime of NMIIA mini-filaments compared to actin filament turnover (about a 5 $s$ unloaded NMIIA mini-filament attachment time compared to an average 0.5 monomers per $s$ turnover rate), and furthermore, does not explain polarity alignment behavior. In fact, the actomyosin systems with the lowest $\chi$ values contracted more than ones with higher $\chi$, as shown in Fig 2.9a. Our results suggest that filament movement in these systems, and thus polarity alignment, is a cooperative effect depending on the synergy of actin filament turnover and NMIIA mini-filament walking.

### 2.3.4 Larger system simulations exhibit polarity alignment and sorting

To test whether a larger, biologically relevant-sized system with longer actin filaments would undergo the same polarity sorting mechanisms as observed in the smaller $1 \times 1 \times 1$ $\mu m^3$ systems, we ran another set of 16 trajectories, for 500 $s$, of a $3 \times 3 \times 3$ $\mu m^3$ sized actomyosin network with an overall actin concentration of 12 $\mu M$ and concentration ratios $R_{m:a} = 0.02$ and $R_{\alpha:a} = 0.1$. 400 filaments were nucleated in the system, resulting in a mean actin filament length of 1.4 $\mu m$ when

reaching a steady-state actin concentration. All trajectories did in fact undergo polarity alignment of sub-domains; Fig 2.10 shows a single trajectory snapshot of the actomyosin network with actin filament cylindrical segments colored by their directional angle with respect to the x-y plane. We see uniformly polar domains, with connections between those domains that span the entire simulation volume and appear to have similar polarity structure to sarcomeric bundle patterning observed *in vivo* [140]. Unfortunately, a detailed analysis of these larger systems is out of the scope of this paper and will be investigated in a future study.

## 2.4 Discussion

Active matter is a growing field of study at the interface of chemistry, mechanics and non-linear physics. In order to model active networks with complete realism, a model must take into account not only chemical processes and the molecular transport that occurs, but also the mechanical response of the network as well as complex mechanochemical feedbacks that result. With the MEDYAN model, one is able to, in a flexible manner, simulate these entities with precision, while also explicitly accounting for their coupling. Having the powerful capability to simulate active networks with this amount of flexibility and detail in aspects of stochastic reaction-diffusion and coarse-grained polymer chain mechanics, this model could be used to provide additional insights on the mechanochemical dynamics of many active networks, including the cell cytoskeleton. To compare the MEDYAN model to other recent agent-based cytoskeletal modeling approaches, an extensive list of mod-

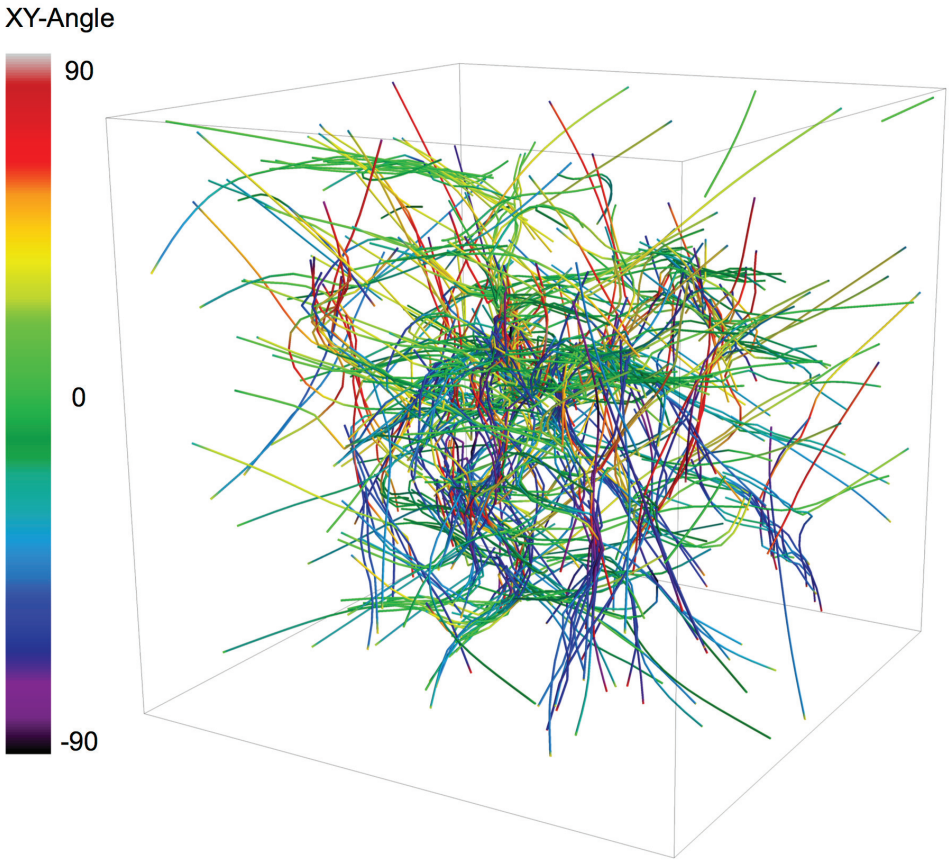


Figure 2.10: A single trajectory snapshot of a $3 \times 3 \times 3$ $\mu m^3$ actomyosin system simulation at $R_{\alpha:a} = 0.1$ and $R_{m:a} = 0.02$ after 500 $s$ of network evolution. Actin filament cylinders are colored by their angle with respect to the x-y plane. In this emergent behavior, polar domains emerge on the length scale of a single filament. From [148].

els in recent literature is given in [148], with notes on the essential mechanochemical capabilities of each model as outlined in the Introduction.

Our public software implementation of MEDYAN (available at www.medyan.org) is also versatile enough such that other active networks, biological or artificial, could be simulated with a similar level of detail in comparison to its cytoskeletal applications, including self-organizing polymeric micelles [206], ParM polymerization mechanisms in bacterial mitosis [123], and many types of synthetic polymer gels.

With these possibilities, the MEDYAN model is able to simulate a range of systems not previously achievable by other cytoskeletal models. Beyond the currently included chemical reaction set and mechanical force fields, the flexibility of the current software implementation also allows for the further development of the model to include new types of chemical and mechanical interactions as well as new classes of molecules, allowing for a completely customizable simulation framework.

As shown in the example application, simple actomyosin network simulations using the MEDYAN model can already capture the dynamics and shed light on the underlying mechanisms of actomyosin contraction and remodeling. Our results show that in a system consisting of actin filaments, myosin II mini-filaments, and cross-linkers, actin filament turnover and cross-linker concentration are both powerful tools to control actomyosin network reorganization and polarity alignment. These results have interesting implications for transverse arc assembly, which has been shown to be critically dependent on myosin II [73,183,189]: by way tightly regulating actin filament turnover as well as localized cross-linker concentration via biochemical regulators, a dynamic transition area between the lamellipodium and lamellum could form, where sharp changes in these parameters could result in dynamic network reorganization and bundle assembly in the lamellar region. The polarity alignment as well as network contraction via myosin II and actin filament turnover we have observed in our simulations suggests that a reorganization mechanism is occuring that is more complex than the previously proposed actomyosin zippering [188,189], which predicts the apolar alignment of actin filaments but not polarity alignment. It is possible that the observed polarity alignment behavior in these simulations via

myosin II and actin filament turnover could drive the sarcomeric polarity pattern formation seen in transverse arcs [35] when developing from an initially disordered, lamellipodia-like actin filament network. But, more studies on larger actomyosin networks with multiple bundled structures should be investigated in the future to test this polarity alignment and contraction mechanism.

While we observed contractile behavior in these systems as well as its dependence on cross-linker concentration, the exact contractile symmetry breaking mechanisms invoked in bundle formation, as well as the exact cooperation of actin filament turnover and myosin II mini-filament walking that results in actin filament polarity alignment, being difficult problems to analyze due to the many dynamic components of our simulation, remain unclear and will be further investigated in the next chapters. However, we initially hypothesized that cross-linkers may have an active role beyond increasing force transmission in overall contractile behavior due to the observed dependencies, and could break contractile-extensile symmetry by freezing contractile configurations into place by binding actin filament segments when they approach each other. We also have propose that actin filament turnover may be a mechanism which allows actin filaments to flip and align in polarity more easily in the actomyosin-cross-linker system. Overall, our results show that in contractile systems where relevant timescales of motor movement are comparable to the timescale of network turnover, i.e. cross-linker (un)binding and actin filament turnover, interesting critical behavior can result, as shown in recent experiments [4, 170]. Determining the exact relationships between these timescales of importance at the observed critical points, as well as the resulting dynamic behav-

ior and network reorganization in these systems, will be an interesting endeavor for cytoskeletal researchers in the future.

While the exclusivity of binding sites on actin filaments seems to alter the trends of contractile dependence of cross-linker concentration, more systems, as well as possible improvements to our model, should be studied in the future to probe these exclusion effects on network dynamics. In particular, we plan to include, in an explicit manner, a more realistic competition of cross-linkers and myosin II to binding sites on actin filaments. Also, the excluded volume effects of both molecules should be developed further such that they cannot pass through actin filaments while network dynamics occur. These developments will help to study the dynamics of these actomyosin networks in a more realistic manner, and will provide additional insights to the problem of contractility emergence and mechanisms. The effect on the accumulation and kinetic trapping of myosin II mini-filaments when this steric exclusion is added will then be investigated, as it has interesting implications for myosin II compartmentalization within the cytoskeleton.

We note that the imposed spatial boundary conditions could play a role in the actin filament polarity organization observed, and, in tandem with NMIIA mini-filaments, might be a contributing factor to the observed uniform bundle polarities in the actomyosin systems. Future works could examine the role of spatial boundary conditions on these organized structure formations, as there have been interesting *in vitro* investigations of the effect of boundaries on actomyosin network assembly as reviewed by Vignaud et al. [193]. In particular, the effect of pre-defined actin network microarchitectures on myosin II dynamics could be further investigated

[152].

# Chapter 3: An investigation of actomyosin force dipoles

*This chapter and its figures are adapted from: James Komianos and Garegin Papoian. "Stochastic Ratcheting on a Funneled Energy Landscape is Needed for the Highly Efficient Contractility of Actomyosin Force Dipoles". **Phys. Rev. X** 8, 021006 (2018)*

## 3.1 Back to the contractility problem

As we have discussed in the previous chapters, the distinct ability of the combination of actin filaments, passive actin cross-linking proteins and myosin II molecular motors to produce contractile cellular force is of fundamental importance in many cell types and has been well-studied in muscle cells [43, 71, 196], where parallel arrangements of filaments in opposite polarities allows for a directed, inward pull of the cell's sarcomeric unit (Fig. 3.1). Contractility is, however, much less understood in motile non-muscle cells, where it frequently emerges from an isotropic filament network with little geometric or polar ordering. These contractile networks are responsible for diverse micro-structural dynamics, including lamellar stress fiber formation of tens of bundled filaments (shown in Fig. 3.1b), cell rear retraction that is essential to locomotion, and tension maintenance in the thin sub-membrane cortical layer surrounding the cell [24]. Prior works on explaining the emergence of contractility

in disordered actomyosin networks have pointed to a variety of effects, including the potential importance of filament buckling [103, 105, 128, 171], actin filament treadmilling [137, 148], and the role of passive cross-linkers as force-transmitters between neighboring contractile clusters [4, 12, 48, 82, 89, 148, 204]. Other studies have also investigated the general non-equilibrium dynamics of such cytoskeletal arrangements, outside of the context of the emergence of contractility, and have described fluidized and glassy network behavior [148, 203] as well as strain-stiffening of the active polymer gel [108].

In light of both recent and older works, the fundamental physical intuition for the emergence of contractility still largely rests on the classical sarcomeric mechanism, where myosin mini-filament heads are bound to two locally anti-parallel actin filaments, allowing the energy-consuming unidirectional walking of those heads to generate a contractile shearing motion between the actin filaments (shown in Fig. 3.1a). Two questions naturally arise with regard to this picture: (1) How do initially isotropic actin networks in three dimensions give rise to these locally anti-parallel contractile force dipoles, and (2) do passive cross-linkers play an important role only in percolating force chains at larger spatial scales, as previously suggested, or are they also important in generating contractility *at the level of a single force dipole?* We will address the first question in Chapter 4.

In this chapter, we address the second question by analyzing an *in silico* actomyosin force dipole: two anti-parallel actin filaments, connected at their furthest ends by springs to boundaries, allowing both cross-linkers and a myosin mini-filament to transiently bind and dissociate. Our analytical and numerical results,

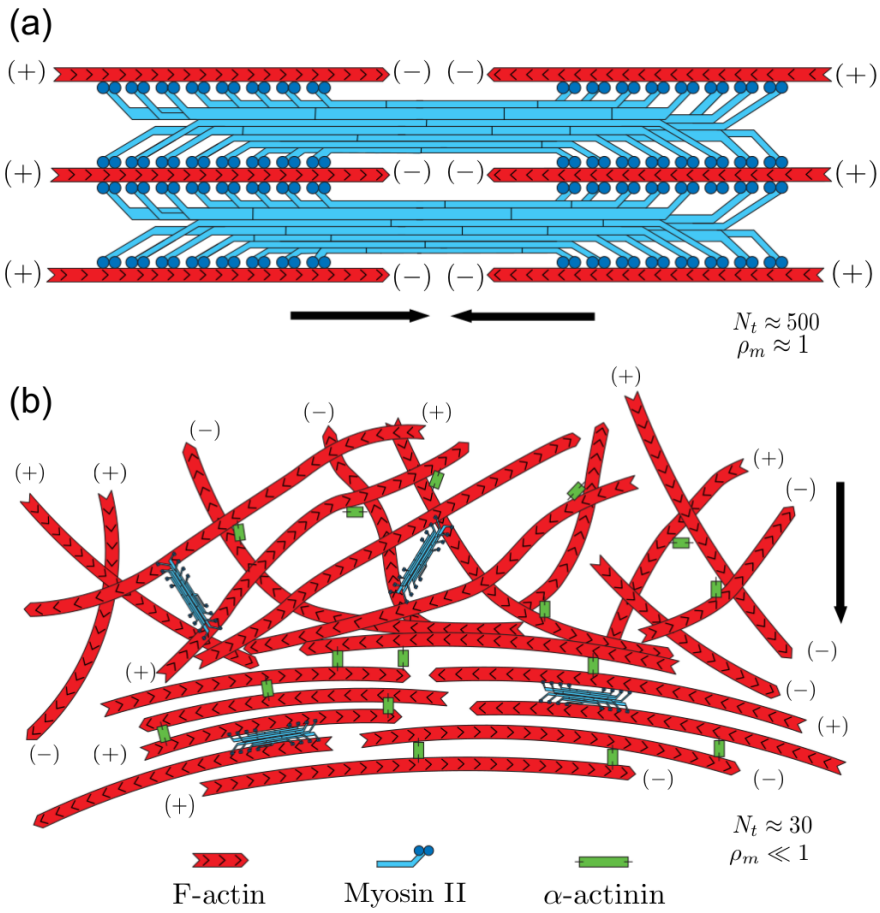


Figure 3.1: a) In a muscle sarcomere, actin filaments are aligned in bands of opposite polarity such that a bipolar myosin II filament can walk towards the actin filament's plus ends, generating maximal contractile force, shown as black arrows. The motor filaments also contain hundreds of heads, which are able to continuously generate force on the filaments and maintain attachment as they hydrolyze ATP to produce mechanical work. b) In a non-muscle actomyosin network, filaments are distributed in a random geometric fashion throughout the cytoskeleton. The myosin II filaments in a non-muscle actomyosin system are also smaller (number of heads per side of bipolar filament $N_t \approx 30$ [20]) and highly transient (the duty ratio of bound to unbound states of the motor filament $\rho_m \ll 1$) compared to their muscle counterparts ($N_t \approx 500$, $\rho_m \approx 1$), but can form disordered arrangements of locally anti-parallel actin filaments. Motor filaments of this nature are responsible for stress fiber formation via compression of a fragmented lamellipodial actin mesh. Figure is from [93], Copyright 2018 American Physical Society.

in qualitative agreement with recent works discussed below [101, 200], indicate that passive cross-linkers play a crucial role already at the scale of a single force dipole,

giving rise to a funneled energy landscape, where greater overlap of actin filaments corresponds to a larger number of bound cross-linkers. These configurations have lower free energy compared with less contracted states such that the dipole is energetically biased towards contractile configurations. In addition to shedding light on this gradient of free energy due to cross-linker binding, we have also discovered strongly non-linear behavior of contractility with respect to the strength of cross-linker binding energy, where a rise of contractile forces is followed by a rapid kinetic arrest of intermediate configurations by strongly bound cross-linkers.

Overall, we found that the thermodynamic drive to more complete overlap of actin filaments is significantly attenuated by trapping in a purely passive force dipole (pFD), generating contractile forces that are noticeably smaller than the ones generated by the unidirectional walking of myosin heads when in the presence of springs counteracting the contraction. However, pure myosin action is also relatively ineffective at generating contractile forces because the bound motor filaments are highly transient, easily permitting recoiling slippage of the contracted element of two oppositely polar actin filaments. We have discovered that cross-linkers can help to overcome this slippage process via a ratcheting mechanism - by using dynamic cross-linkers to prevent recoiling of intermediate configurations without bound motors, amplified contractile forces are produced. This presence of active motor behavior can thus create sharply amplified contractile forces depending on the mechanical and dimensionality constraints of the dipole considered. Our work reveals strong synergy between passive cross-linker binding dynamics and active myosin processes in an active force dipole (aFD), which constitutes the main building block of actomyosin

contractile network.

## 3.2 Modeling a force dipole

### 3.2.1 Mechanical Langevin representation

To shed light on the thermodynamic and kinetic nature of a fundamental contractile actomyosin element interacting with passive cross-linkers, which serve as building blocks of more complex actomyosin networks in non-muscle cells, we constructed and carried out various simulations of a pair of rigid actin filaments in one dimension (Fig. 4.1), where cross-linker proteins dynamically bind and unbind to the overlapping region. We first considered a system where only cross-linker binding generates contractile forces in a pFD, followed by simulations where a unidirectional motor was added to form an aFD, in which the motor filament can walk in the direction of the plus end of the actin filaments to generate additional mechanical force. We first note that all parameters are given in Table B.1 and Table B.5 contained in the Appendices. Two actin filaments, denoted as the right and left filaments with respect to the simulated length, have length $L = 2\ \mu m$ and midpoints $x_r$ and $x_l$, with initial midpoint positions $x_r^0 = 1\ \mu m$ and $x_l^0 = 3\ \mu m$, respectively. An overlap length $l_o$ between the two filaments can then be defined as $l_o = (x_l + L/2) - (x_r - L/2)$. Each filament is connected to springs at their outward-facing plus ends such that the tension provided by the springs on each filament is $F_t^r = -K_t(x_r - x_r^0)$ and $F_t^l = -K_t(x_l - x_l^0)$. The diversity of the chemical states of the force dipole can be represented with the integer values, $(m, n)$, with $m \in [0, 1]$

and $n \in [0, \infty]$, which specify the number of (active) myosin II motor filaments and (passive) cross-linkers bound to the filament pair, respectively.

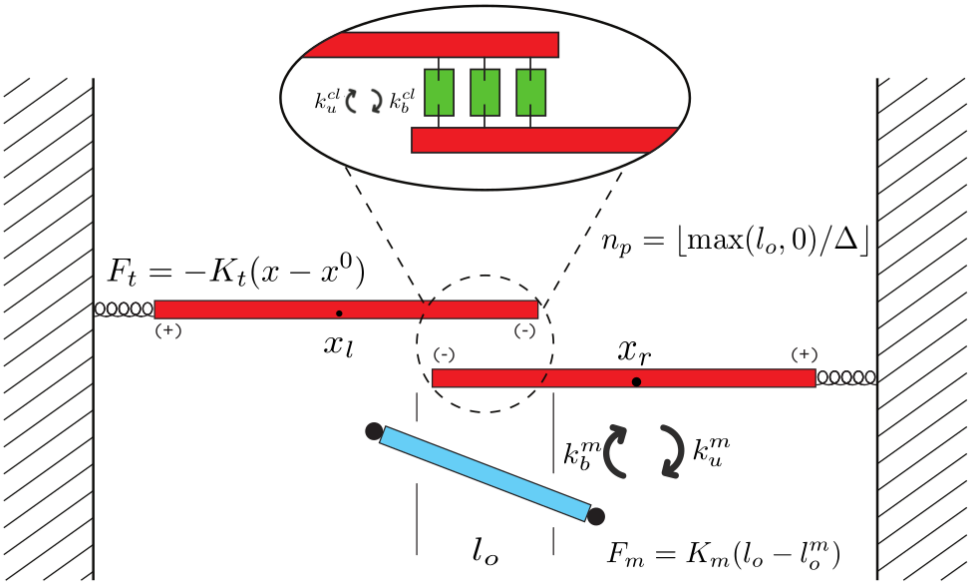


Figure 3.2: An actomyosin dipole model. Two filaments with plus ends facing outward and midpoints $x_r$ and $x_l$ are both connected to springs with stiffness $K_t$, initially with an equilibrium filament position of $x_r^0$ and $x_l^0$. When no cross-linkers are bound between the two filaments, they separately undergo tethered Langevin motion. While the filament overlap $l_o$ is large enough, cross-linkers can transiently bind and unbind according to their kinetic rates as in Eq. 3.2, which arrests the filaments if the number of cross-linkers bound is non-zero.The number of available binding sites $n_p$ varies with actin filament overlap. Motor filaments can (un)bind and walk stochastically on the pair of actin filaments, generating force via a time-varying filament overlap potential. Figure is from [93], Copyright 2018 American Physical Society.

When there are no motors or cross-linkers bound to the pair of filaments ($m = 0$, $n = 0$), they can separately undergo overdamped Langevin motion that includes forces provided by their respective tethers and a stochastic force, via $\eta \frac{dx_l}{dt} = F_t^l + F_s$, and $\eta \frac{dx_r}{dt} = F_t^r + F_s$, where $F_s$ satisfies the fluctuation-dissipation theorem in one dimension. The instantaneous number of sites, $n_p$, available for binding in the overlapping region between the two filaments, is obtained from $n_p = \lfloor max(l_o, 0)/\Delta \rfloor$,

where $\Delta$ denotes the spacing between adjacent binding sites. We assume that the filaments move only in the absence of bound cross-linkers ($n = 0$), otherwise, they are immobilized ($n \neq 0$). We further expect that upon binding of a cross-linker, the tension in each respective actin filament tether is nearly instantaneously equilibrated such that $|F_t| \equiv |F_t^r| = |F_t^l|$ while preserving the average tensile force experienced by the filament pair at the time-step before equilibration $|F_t| = \frac{1}{2}(|F_t^l| + |F_t^r|)$. This equilibration assumption is based on the separation of timescales between tether relaxation ($\approx ms$) and (un)binding dynamics ($\approx 0.1\ s$ in the fastest simulated case). The spatial positions of the filament pair remain stationary until complete cross-linker unbinding ($n = 0$).

The filament pair can also experience an active motor contractile force, $F_m$, when a motor is bound ($m = 1$), via a stochastically time-varying filament overlap potential, $F_m(t) = K_m(l_o(t) - l_o^m(t))$, where $l_o^m(t)$ indicates the filament overlap corresponding to an unstretched motor. Upon a new binding event, this motor parameter, which implicitly represents the intrinsic length of the molecule, is initialized to $l_o(t)$. This defines the motor filament's equilibrium length in terms of the filament pair's configuration at the moment of motor's binding. Then, $l_o^m(t)$ can stochastically increase by a motor step size $d_s$ with average walking velocity $v_w$, where this velocity depends on the instantaneous value of $F_m$, as described in Section B.1. With this active force contribution, the aggregate force experienced by all cross-linkers bound between the filament pair can be written as $F_{cl} = |F_m - F_t|$. The simulation protocol iteratively performs Gillespie stochastic simulation for chemical dynamics (including both binding, unbinding and motor-stepping events) and

switches to overdamped (mechanical) Langevin dynamics when the number of bound motors and cross-linkers becomes zero (i.e. $m$=0 and $n$=0). The latter dynamics is then evolved for $\tau_r$, which is the reaction time for the next re-binding event, estimated stochastically based on the same Gillespie algorithm.

### 3.2.2 Stochastic thermodynamics of cross-linking

Next, we relate the stochastic (un)binding rates of cross-linkers on the filament pair to their thermodynamic binding energy, denoted as $\epsilon$. This binding energy can be phenomenologically related to the change in Helmholtz free energy $\Delta A$ by the following form, which contains enthalpic and entropic contributions [70]:

$$\Delta A \approx -\epsilon + k_b T ln\left(\frac{v_m}{v_b}\right) \tag{3.1}$$

where $v_m = V/N$ is the inverse concentration of $N$ cross-linkers in volume $V$ in solution. $v_b$ can be thought of as the binding site volume of the cross-linker, which at most physiological concentrations is much smaller than $v_m$. Intuitively from this equation, one can imagine system entropy is lowered from cross-linker binding as $k_b T ln(\frac{v_m}{v_b})$, but is counter-acted by binding favorability $\epsilon$.

We assume upon cross-linker binding $P\Delta V \approx 0$ such that we can equate the change in Helmholtz free energy $\Delta A$ to the change in Gibbs free energy $\Delta G$. Combining Eq. 3.1 with this approximation, and using the classic relation for the dissociation of a molecule from a binding site $K_D = e^{\Delta G/k_b T}$, one obtains an approximate expression for the dissociation constant $K_D$ of cross-linkers in this system in

terms of their binding energy as

$$K_D \approx \frac{v_m}{v_b} e^{-\epsilon/k_b T}. \tag{3.2}$$

$K_D$ can then be related to the stochastic cross-linker reaction constants by $K_D = k_u^{cl}/k_b^{cl}$. Therefore, the concentration of cross-linkers ($[L] \propto 1/v_m$) as well as cross-linker bond energy $\epsilon$ influences the binding of cross-linkers to the filament pair in this description, with linear and exponential dependencies, respectively. In simulation, we will demonstrate the effects of varying the thermodynamic parameter $\epsilon$ for sets of fixed $k_u^{cl}$. This results in variation in $k_b^{cl}$, altering the stochastic dynamics of the force dipole.

### 3.2.3 Motor force contribution

Non-muscle myosin II molecules *in vivo* are assembled into bipolar mini-filaments, with patches of motor heads radiating outward [144] which then can (un)bind to neighboring filament segments. Hence, we must consider motor filament kinetics in our model as a coarse-grained version of a detailed stochastic process including $N_t$ transient motor heads per side of the mini-filament, coexisting in a connected bipolar structure. The number of motor heads per side of a mini-filament is typically $N_t \approx 30$ (in total $\approx 60$ heads per mini-filament) [20], so it is reasonable to assume that $< 10$ of these heads per side could be bound to a single actin filament simultaneously - we choose $N_t = 10$ for our simulations, which produces a mean unbinding time of $\bar{\tau}_u^m \approx 1/s$ in absence of mechanosensitivity. Since

tension is released upon unbinding of either side of the bipolar filament, we use this value as the effective unbinding rate of our coarse-grained description. Therefore, even with multiple motor filament heads possibly attached to a single actin filament, the stochastic dynamics of these heads creates a highly transient system of tension build and release between the filament pair. We leave the description of our mechanochemical model for these myosin II filaments, which explicitly includes catch-bond dynamics, to Section B.1.

## 3.3 Passive force dipoles in one dimension

### 3.3.1 Numerical results

In the absence of motor filaments, cross-linkers can create a substantial amount of contractile force in the one-dimensional anti-parallel filament pair against elastic tethering simply by rectifying Brownian fluctuations which increase filament overlap. Contraction of the pFD can be quantified in terms of a thermodynamic parameter $\epsilon$ and kinetic parameter $k_u^{cl}$ using their previously defined relation. Fig 3.3a shows the average force generated by the dipole $\langle F_D \rangle = \langle\ |F_t^l| + |F_t^r|\ \rangle$ in 250 simulations for 200 $s$ - we denote this time as $\tau_{lab}$. We observe a sharply biphasic dependence of generated force on varying cross-linker binding energies. At low $\epsilon$, cross-linkers cannot sustain significant levels of tension between the filaments due to a low occupancy of the available binding sites, while at high $\epsilon$, significant kinetic arrest occurs due to quick saturation of the binding sites, significantly hindering filament motion. While cross-linkers are able to generate overlap between the filament pair when restoring

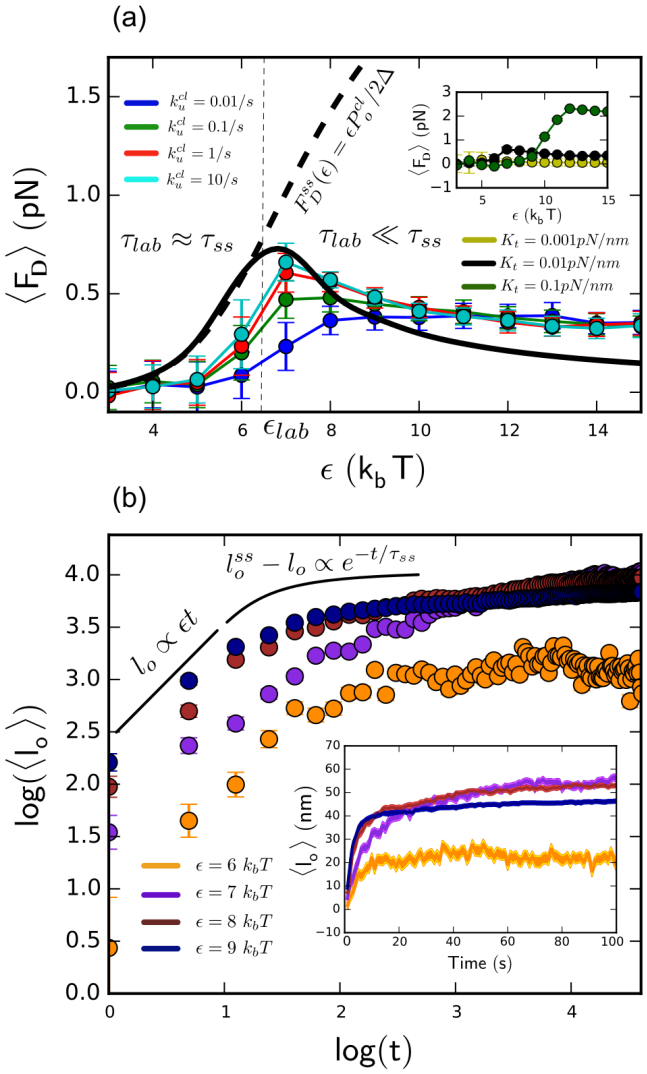


Figure 3.3: a) Average force $\langle F_D \rangle$ at $\tau_{lab} = 200s$ for $K_t = 0.01\ pN/nm$, as a function of cross-linker binding energy $\epsilon$. The analytically predicted $F_D^{ss}$ according to the thermodynamic limit in Eq. 3.8 is shown as the black dotted curve, with the numerical solution to Eq 3.7 as solid black - these solutions diverge at $\epsilon_{lab} \approx 6$ $k_bT$. This corresponds to the transition $\tau_{lab} \ll \tau_{ss}$ caused by increasing binding strength of cross-links. Increasing speed of unbinding shifts curves to the predicted thermodynamic limit. Inset displays stochastic trajectories for the same cross-linker binding energies. b) Log-log plot of the average filament overlap $\langle l_o \rangle$ versus time for $\epsilon$ values around $\epsilon_{lab}$ shows a linear force-generating regime $l_o \propto \epsilon t/(1 + v \cdot e^{-\epsilon/k_bT})$ followed by a exponential relaxation to steady state $l_o^{ss} - l_o \propto e^{-t/\tau_{ss}}$ with $\tau_{ss} \propto (1 + v^{-1}e^{\epsilon/k_bT})^{l_o/\Delta}$. Trajectories above $\epsilon_{lab}$ are far from equilibrium at $\tau_{lab} = 200s$, as shown by a significant flattening of the $l_o$ vs $t$ curve at long times for increasing binding energy. Figure is from [93], Copyright 2018 American Physical Society.

forces are minimal, at most binding energies simulated, they are ineffective against stiffer springs counteracting the contraction of the pair ($K_t = 0.1\ pN/nm$). This is due to slippage of the filament pair when cross-linker dissociation occurs, releasing contractile tension between them. Contraction can only be generated in this case if the binding affinity of the cross-linkers is greater than 10 $k_bT$, which induces complete arrest of the filament pair upon a single site occupancy.

Essential to the characteristic force production of the pFD is not only the overall cross-linker affinity $\epsilon$, which controls the probability of occupancy of the $n_p$ sites between the filament pair, but also, crucially, the kinetic rates of binding and dissociation processes that determine how quickly initially non-equilibrium dynamics approaches the steady state. The former arise purely from statistical mechanics principles, as we show below. Accelerating cross-linker binding kinetics in this regard (i.e. simultaneously increasing $k_b^{cl}$ and $k_u^{cl}$ while maintaining binding energy as in Eq 3.2) shifts resulting force curves upward until saturation is reached for $k_u^{cl} = 10\ s^{-1}$. This can be thought of as approaching the thermodynamic limit of force production of the dipole as $k_u^{cl} \to \infty$.

Furthermore, in order to derive a mean-field equation of motion describing the change in filament overlap over time, it would also be useful to have an analytical expression for the mean-first passage time of unbinding of $n$ cross-linkers from $n_p$ cross-link binding sites on the filament pair, $\bar{\tau}_u^{cl}$, since this mean behavior defines the rate of filament overlap increase, and thus the timescale of relaxation $\tau_{ss}$ of the contractile element. In our stochastic representation, this is the mean time of transitioning from the $n = 1$ to $n = 0$ state. Surprisingly, this mean-passage-

time problem is similar to the stochastic dynamics of an ensemble of myosin II motor heads becoming completely unbound from an actin filament. Recasting this equation to apply to cross-linker dynamics by replacing the number of motor heads $N_t$ with the number of possible binding sites $n_p$, as well as cross-linker kinetics of (un)binding, we obtain an expression for the mean-passage-time of complete cross-linker unbinding:

$$\bar{\tau}_u^{cl} \approx \frac{1}{k_b^{cl} n_p}\left[\left(1+\frac{k_b^{cl}}{k_u^{cl}}\right)^{n_p} - 1\right]. \tag{3.3}$$

On the other hand, the mean binding time (i.e. transition time from $n = 0$ to $n = 1$) is simply $\bar{\tau}_b^{cl} = k_b^{cl} n_p$. We note that both passage times are fundamentally dependent on the filament overlap by the definition of $n_p$ given above. Predictions of Eq 3.3 show agreement with simulated first-passage times of cross-linkers from $n = 1$ to $n = 0$ at various binding site availabilities.

### 3.3.2 Deriving a mean-field contraction equation

With this, we can construct an equation of motion describing the observed stochastic contraction process in terms of the cross-linker's mean-field energetic contribution to the filament pair and the resulting elastic restoring forces of the filament pair. First, in absence of stochastic effects, a thermodynamic driving overlap force $\epsilon P_o^{cl}/\Delta$ is expected to result when the filament pair increases their overlap by a distance $\Delta$, with a probability of occupancy of the binding site $P_o^{cl} = k_b^{cl}/(k_b^{cl} + k_u^{cl})$. Since the motion of the filament pair is hindered if $n \neq 0$, an effective mean-field

equation of motion neglecting stochastic force can be written as:

$$2\eta\frac{dl_o}{dt} = \left(\frac{\epsilon}{\Delta}P_o^{cl} - 2K_t l_o\right)(1-\delta_n), where \tag{3.4}$$

$$\delta_n = 0, \quad if\ n = 0. \tag{3.5}$$

$$1, \quad if\ n \neq 0. \tag{3.6}$$

Note in this description our equation contains a random state variable $\delta_n$ such that motion is allowed when there are no cross-linkers bound to the filament pair, and $\eta = 10^{-3}\ pNs/nm$ is the viscous damping constant of an individual actin filament. Averaged over many intervals of $n = 0$ and $n \neq 0$ states, which is valid under the assumption that many intervals occur in motion to a new cross-link position $l_o \pm \Delta$, i.e. $\eta\Delta^2/\epsilon \gg \bar{\tau}_b^{cl} + \bar{\tau}_u^{cl}$, the $(1-\delta_n)$ term can be separated from the average and evaluated explicitly as the probability of the $n = 0$ state during simulation to provide a full mean-field solution. This assumption bounds the kinetic rates considered to $\bar{\tau}_u^{cl} << 1s$. We express this probability in terms of the cross-linker binding energy as $P(n=0|l_o) = \bar{\tau}_b^{cl}/(\bar{\tau}_b^{cl} + \bar{\tau}_u^{cl}) = (1 + v^{-1}\exp(\epsilon/k_bT))^{-l_o/\Delta}$ with $v = v_m/v_b$. This bears similar resemblance in its form to the statistical mechanics problem of Langmuir absorption. We now have a final equation of motion, where we change variables $\tilde{l}_o$ to indicate the interval-averaged overlap:

$$2\eta\frac{d\tilde{l}_o}{dt} = \left(\frac{\epsilon}{\Delta}P_o^{cl} - 2K_t\tilde{l}_o\right)(1 + v^{-1}e^{\epsilon/k_bT})^{-\tilde{l}_o/\Delta}. \tag{3.7}$$

This equation predicts a near-linear contractile regime in the short-time limit with a constant velocity: $l_o \propto V_o^{cl}t$. This is followed by an exponentially decaying relax-

ation to steady state $l_o^{ss} - l_o \propto e^{-t/\tau_{ss}}$ (details of the asymptotic analysis are given in Section B.3). In general, $V_o^{cl}$ is directly proportional to the bond energy and occupancy of cross-linkers in absence of non-equilibrium effects, and $\tau_{ss}$ is inversely proportional to the occupancy of the available binding sites. This is observed in our simulations with predicted $V_o^{cl} \propto \epsilon/(1 + v \cdot e^{-\epsilon/k_bT})$ and $\tau_{ss} \propto (1 + v^{-1}e^{\epsilon/k_bT})^{l_o/\Delta}$ asymptotic behaviors, as shown in Fig 3.3(b). At infinitely long time, the equation of motion predicts the steady state overlap,

$$l_o^{ss}(\epsilon) = \frac{1}{2\Delta K_t} \frac{\epsilon}{1 + v \cdot e^{-\epsilon/k_bT}}, \tag{3.8}$$

which is shown in Fig 3.3a as the upper bound of the finite-time solutions which contain kinetic arrest. This steady-state prediction diverges from measurements during the laboratory timescale (i.e. $\tau_{ss} \gg \tau_{lab}$) when $\epsilon$ passes a threshold of 6 $k_bT$, which we denote as $\epsilon_{lab}$. Therefore, our results indicate the sharp onset of a glass-like behavior which produces a transition to far-from-equilibrium filament states. This greatly limits force production of the filament pair when cross-linker affinity becomes greater than $\epsilon_{lab}$. It is important to note that increasing the cross-link concentration in solution $[L]$ would linearly increase the stochastic rate constant of cross-link binding (Eq 3.2), thus altering the onset of contractile behavior described in Eq 3.7.

This analysis shows that a passively cross-linked filament dipole can produce low $pN$ scale forces, in agreement with recent works [81, 101, 179, 200], *only if* the cross-links are sufficiently favored to bind to the filament pair from the surrounding

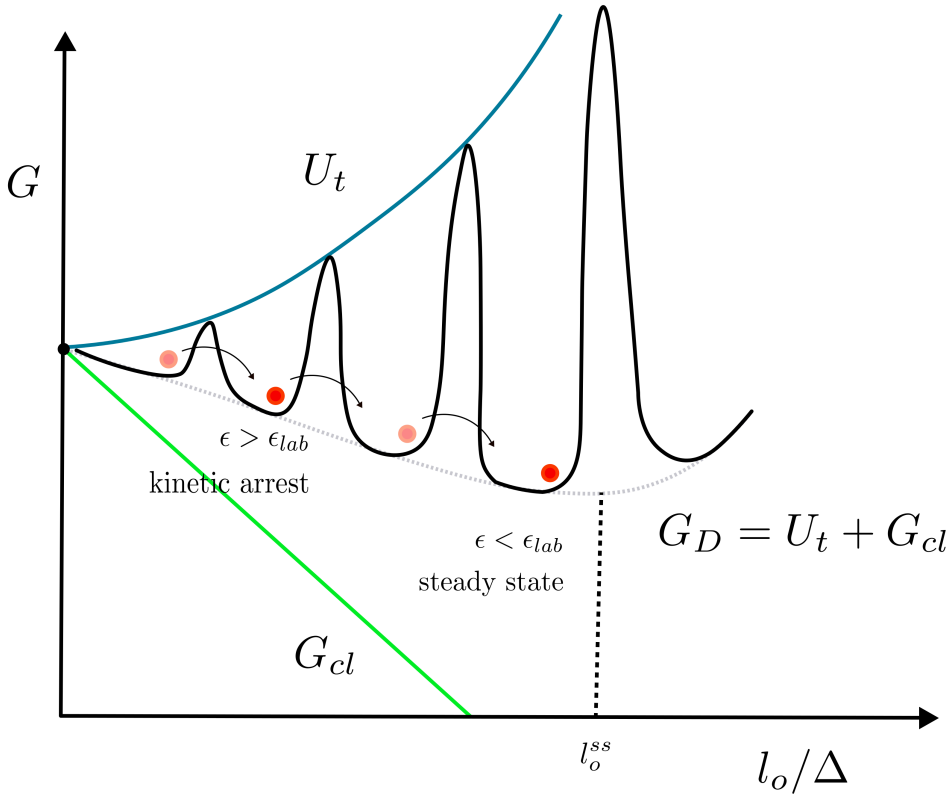


Figure 3.4: The free energy landscape in a force dipole.The total free energy $G_D$ is a summation of cross-link ($G_{cl}$) and tether ($U_t$) contributions. $G_{cl}$ is a linear function of overlap and the slope of this line can be thought of as the average free energy difference per addition of a single binding site in the dipole (since the number of binding sites $n_p \propto l_o/\Delta$). The dipole's timescale of approach to steady state overlap (dipole overlap shown as red dots in $G - l_o/\Delta$ diagram) is in general an exponential function of cross-link binding affinity such that a dipole can become kinetically arrested on the laboratory timescale if $\epsilon > \epsilon_{lab}$, and thus $\tau_{lab} \ll \tau_{ss}$. Otherwise, the dipole can reach the steady-state free energy minimum overlap $l_o^{ss}$. Figure is from [93], Copyright 2018 American Physical Society.

solution, forming a funneled free-energy landscape with respect to filament overlap in the force dipole. Despite the manifest non-equilibrium nature of this contraction process, the stochastic trajectories of the dipole could be well understood by treating cross-linkers as exerting a mean-field mechanical driving force of thermodynamic origin. Furthermore, our analysis predicts that this driving force acts to not

only favor but also eventually arrest filament overlap depending on the nature of cross-linker binding. A graphical description of this energy landscape with kinetic restrictions is given in Fig 3.4.

## 3.4 Active force dipoles in one dimension

### 3.4.1 Numerical results

We also show a positive feedback mechanism which produces an force amplification of the one-dimensional cross-linked filament pair when in the presence of active fluctuations. As highly transient myosin II motor filaments are added (the mechanochemical model for motor filaments is outlined in Section B.1) to form an active force dipole (aFD) in absence of cross-linkers, the frequent unbinding of the motor filament causes a continual build and release of contractile tension over the simulation duration, resulting in minimal force generation ($\approx 0.3\ pN$ against $K_t = 0.01\ pN/nm$ springs). However, when cross-linkers are present, 3- to 17-fold amplifications are observed compared to the original forces generated in absence of the motor filament (Fig 3.5) at an $\epsilon_{lab} \approx 5\ k_bT$. This is shifted from the pFD case, mainly due to myosin II now counter-acting restoring tension in the boundary springs, reducing overall tension on cross-linkers in the overlap region and decreasing their effective unbinding rate, consistent with slip-bond feedback. We also observe an overall sharp increase in transient motor filament force production when increasing stiffness of external springs, consistent with the myosin II's catch bond nature [49, 175].

At higher external stiffness $K_t = 0.1\ pN/nm$, motor filaments alone are more effective than cross-linkers at generating contractile forces for a range of binding affinities ($\epsilon \approx 0 - 10\ k_bT$) but are still minimally contractile compared to when both passive and active elements are present, which produces 22 $pN$ of force at peak binding affinity. The collective behavior of the one-dimensional actomyosin-cross-linker system is shown in Fig. 3.5b)-c) - a "ratcheting" behavior in which the motor, although becoming (un)bound frequently, can steadily produce force over the entire simulation interval, helped by cross-linkers transiently stabilizing filament overlaps. A graphical summary of this behavior is shown in Fig. 3.5d).

### 3.4.2 Deriving kinetic behavior of active dipole

It is clear that cross-linker trapping of contractile configurations drastically affects the dynamics of an actomyosin dipole. To investigate this effect, we defined in our subsequent analysis two random variables (explicitly dependent on initial filament overlap) which both quantify a change in overlap between filament pairs in a single ratcheting cycle: a contraction function $\chi(l_o)$ in which ($n = 0$, $m = 1$) and a extension function $\xi(l_o)$ in which ($n = 0$, $m = 0$). Both events terminate when $n \neq 0$ and have distance units. Then, by collecting the observed overlap change in simulations for each ratcheting cycle, binned by the dipole's initial overlap, we constructed an effective inter-filament velocity profile of the aFD, representing the rate at which overlap increases in the filament pair: $V_{eff}(l_o) = \chi(l_o) \cdot \omega_\chi(l_o) - \xi(l_o) \cdot \omega_\xi(l_o)$, where $\omega_\chi(l_o)$ and $\omega_\xi(l_o)$ represent the frequencies of the respective stochastic events from

simulations. Figure 3.6 shows the simulation results - as binding energy is raised from $\epsilon < \epsilon_{lab}$ to $\epsilon \approx \epsilon_{lab}$, contractile velocities decrease significantly at low filament overlaps but become positive at large overlaps due to structural ratcheting, driving maximal contraction of the force dipole at $\epsilon \approx \epsilon_{lab}$. In agreement with a transition to kinetic arrest observed previously, in the regime $\epsilon > \epsilon_{lab}$, contraction events are efficient and extension events minimal, but filament motion is severely hindered at large overlaps. This contraction and extension behavior can be reproduced analytically by averaging over the possible kinetic events of contraction and extension in the element - this is derived in Section B.4.

Therefore, the energy landscape induced by transient cross-linking in a passive force dipole was directly observed in the non-equilibrium aFD in our one-dimensional simulations, although in general the steady state and glassy behavior, unlike the pFD dynamics, is not analytically tractable. This active driving resulted in an amplification of contractile forces produced by the dipole, via the ratcheting of motors on the original funneled energy landscape created by cross-linking. Hence, passive cross-linking can play an essential role in contractility, even at the scale of a force dipole containing a single myosin II mini-filament.

## 3.5 Active force dipoles in three dimensions

### 3.5.1 *MEDYAN* simulations

Until now, we have been considering actin filaments in one-dimensional force dipoles, treating the actin filaments as non-deformable under passive and active mo-

tion. This is usually a valid assumption for non-muscle myosin II mini-filaments in an idealized geometry, since motor forces presumably operate under a critical buckling threshold of actin filament segments [2]. Motors interacting with deformable actin filaments and cross-linkers in disordered networks, however, may produce buckling and shearing at the formed cross-linking junctions, providing a channel for active stress dissipation. Therefore, we finally consider the more realistic scenario of semi-flexible actin filaments and cross-linkers interacting in three-dimensional geometries.

To investigate the implications of this mechanical feature, we use the recently developed *MEDYAN* active network model [148], built on previous cytoskeletal modeling efforts in our laboratory [77, 78, 100, 211], to generate an *in silico* three-dimensional force dipole. Our setup would correspond to a hypothetical *in vitro* dual optical trap experiment. More specifically, this model is comprised of: (1) two semi-flexible actin filaments, tethered to springs at their plus ends (to represent optical traps with stiffness $K_t$ as will be discussed), coarse-grained into cylindrical segments, containing bending and stretching modes and a volume exclusion of pair-wise segments, and (2) transient passive cross-linkers and active myosin II motor filaments (both at $1\mu M$) which can diffuse via a stochastic subvolume reaction-

[2] Assuming a critical buckling force for a cross-linked segment of the form $f_c \approx \pi^2 k_b T l_p / L^2$ where $l_p = 17\mu m$ for an actin filament [54], and the inter-cross-link distance of the actin filament network being $L = 0.4\ \mu m$ [50], which is representative of lamellar actin concentrations of 30 $\mu M$, the estimated critical buckling force for these network segments is 4.3 $pN$. Assuming ten motor heads of non-muscle myosin II (isoform A) are available for binding to an actin segment, predictions for force generation of this small ensemble is well below 5 $pN$ due to the stochastic nature of the non-processive motor heads [49, 175]. We also confirm this in our force dipole simulations

diffusion scheme and (un)bind to neighboring filament segments, coupling them mechanically. A simulation snapshot of this setup is given in Fig 3.7. In this simulation protocol, motor filaments can stochastically walk between filament segments when bound, generating active network stress similar to the one-dimensional model. The simulation protocol iteratively performs stochastic-reaction diffusion simulation and equilibrates the resulting mechanical deformations due to localized motor motion after a set of chemical events. Details of the simulation protocol are given in Section B.1, with relevant simulation parameters and observables in Table B.1.

As expected, generated force in the three-dimensional dipole is a strong function of cross-linking affinity, as seen in Fig. 3.7b). Overall, 16 independent trajectories of dipoles were run for varying cross-link energy $\epsilon$ and tether stiffness $K_t$. An overall amplification of overlap and tether force generation is observed compared to the transient motor forces alone at each stiffness (up to 3-fold for $K_t = 0.1\ pN/nm$). Furthermore, we again see a transition to kinetic arrest as evident by a non-linear decrease in cross-linker fluctuations at all stiffnesses tested (Fig 3.7c)). On the other hand, these simulations indicate a noticeable transition to a monotonically saturating force at high trap stiffness, unlike the one-dimensional case which almost entirely decays at large bond energies. We attribute this effect to the ability of cross-linked filaments to rotate from their initial bond position when bound to the anti-parallel filaments. Because of cross-linker pivoting, myosin II active motion can then open new possible binding sites by shearing the dipole, without waiting for complete cross-linker unbinding. In particular, extremely high-affinity cross-linkers can arrest those short-lived configurational fluctuations, providing a significant increase in sustained

dipole tension. This overall behavior occurs when the characteristic length scale of overlap approaches $l_o \approx \Delta$, which corresponds to boundary stiffnesses of $K_t = 0.1$, 1 $pN/nm$ in our simulation.

### 3.5.2 Comparison to one-dimensional numerical model

Next, we compare force production observed in our 3D *MEDYAN* simulations with the corresponding predictions of the 1D model described above. First, let's define the probability of cross-link site occupancy $P_o^{cl} = (1 + ve^{-\epsilon/k_bT})^{-1}$. A power law relation can be fit by using the 1D steady-state prediction when $\epsilon < \epsilon_{lab}$, raised to an arbitrary exponent $\alpha$:

$$F_D^{ss} \propto \left(\epsilon P_o^{cl}\right)^{\alpha}, \tag{3.9}$$

where $\alpha$ is obtained by fitting *MEDYAN* simulation data. In one dimension, $\alpha = 1$.The power law is shown in Fig. 3.7 and gives exponents of $\alpha = 0.4$, 0.24, and 0.05 for external stiffnesses of $K_t = 0.01$, 0.1, 1 $pN/nm$, respectively. A decrease in $\alpha$ indicates a transition to a motor-dominated regime of force production due to the motor's catch bond nature, as predicted at stiffnesses greater than 1 $pN/nm$ for myosin IIA [175]. Therefore, dipole contractility is most amplified by cross-linking when external stiffness is below this threshold.

We also tested whether initial overlap of the actin filament pair, as well as initial incidence angle (as long as initially within pairwise binding range of myosin II) have intuitive effects on dipole dynamics. If the actin filaments have some initial

overlap $l_o^i$ while still initially in a $\langle F_D \rangle = 0$ state (starting at $t = 0$), the overall tension produced in the dipole on $\tau_{lab}$ is decreased due to newly available binding sites causing additional kinetic friction as previously described. Still, these simulations display characteristics of the passive cross-linker energy landscape and follow a similar $F_D$ vs $\epsilon$ trend. Overall, actomyosin dipoles provide force in an overlap-dependent manner - this is shown in Fig 3.7d). Incidence angle of filaments, in contrast, has no effect on their resulting contractile force, since the combination of myosin II and passive cross-linking drives the filaments to tense anti-parallel orientations relative to the dual traps, regardless of initial crossing geometry.

In summary, cross-linker deformability in a three dimensional force dipole results in new channels active stress dissipation, as well as a transition to monotonically saturating forces at high binding energies. Surprisingly, actin filament deformability had no effect on overall dynamics in our analysis - increasing the bending modulus of actin filaments four-fold caused no significant changes in force production at all cross-linker binding energies. This data is not shown for brevity.

## 3.6 Discussion

In this chapter, we have investigated the ability of a pair of actin filaments to contract by rectifying thermal and active motions in stochastic models with varying complexity. The contraction of these elements is essential in understanding the macroscopic dynamics of cross-linked actin gels undergoing myosin II rearrangement in non-muscle systems, but differs from the classic sarcomeric contractility mech-

anisms that neglect passive cross-linkers as potential force producers. We found that the free energy landscape induced by the favorable binding of passive cross-linkers can create noticeable contractile force in a one-dimensional filament pair, however, typically in a biphasic window of binding affinities. This adds a crucial regime of behavior to the continuum description of Walcott et al., who predicted a monotonic contractile filament sliding with cross-linker bond energy without this arrested state [200].

While passive cross-linkers in absence of myosin II in our simulations lead to force production within the pair of filaments, these forces in general are smaller than forces generated by myosin II motors. The latter by themselves also become rather inefficient, however, due to overlap slippage caused by restoring forces when myosin II transiently dissociates, which is frequent because of their low processivity at low external stiffness [49, 175]. Hence, in this work, we have discovered that simultaneous combination of all three components, namely actin filaments, cross-linkers with a sufficient binding affinity, and myosin II, can produce a highly contractile active force dipole due to a stochastic amplification mechanism where cross-linkers trap contractile states as transient motors (un)bind frequently. Also, importantly, cross-linker deformability must be considered for a realistic representation of actomyosin force dipole dynamics. In particular, myosin II's ability to actively shear the dipole and produce additional binding sites without complete cross-linker dissociation generates a specific mode of contraction which is monotonically dependent on passive cross-linker binding affinity. This should be observed in systems where the characteristic distance between cross-links is on the same order of magnitude as

the generated overlap between filaments. Otherwise, cross-linkers' effect on overlap generation should be biphasic.

Our simulations give predictions for a possible optical trapping experiment, similar to [52, 101], but including a dual trap with two actin filaments anchored to separate beads, which can then transiently interact with cross-linking proteins and myosin II motor filaments. This setup would measure the time evolution of trap restoring forces $\langle F_t^r \rangle$ and $\langle F_t^l \rangle$ upon interacting with motor filaments and cross-linkers. Mainly, we would predict a strong amplification of the original $\langle F_D \rangle$ vs $[L]$ relation (i.e. the passive force dipole force production) when motor filaments are added to the system, producing force greater than the sum of individual motor and cross-linker contributions. We also expect to observe a strongly biphasic behavior of contractile force with respect to variation of concentration $[L]$ or cross-link binding affinity $\epsilon$, with a kinetic arrest regime where cross-linker and filament fluctuations decay exponentially, including shift to monotonic force production at trap stiffnesses greater than $0.1 pN/nm$.

While we have chosen to use $\epsilon$ as the main control variable in this paper, our description can also predict behavior with respect to variation in cross-linker concentration $[L]$, mainly that in the dual optical trapping experiment, $F_D^{ss} \propto [L]^{\alpha}$ at steady state, where $\alpha$ is sub-linear ($\alpha = 0.4$, 0.24, and 0.05 in our simulations for $K_t = 0.01 - 1\ pN/nm$). Similarly, we also predict an exponential increase in relaxation timescales with increasing overlap and cross-linking affinity, in qualitative agreement with recent experiments by Lansky et al. of exponentially increasing friction with bound cross-linkers in microtubule assays [101].

In summary, we have shown that robust contraction can occur in the fundamental non-muscle actomyosin building block due to a mechanism arising from the energetic favoring of increased passive cross-linking, independent of mechanical network symmetry breaking (i.e. buckling of filaments as previously shown [128, 171]). Overall, we envision a disordered actomyosin network to be comprised of highly contractile pFD's and aFD's, where the emergent contractility of an entire network, in general, is not a linear combination of dipole-like contractions in the comprising elementary units. In this case, the relative importance of these elements should be largely determined by boundary conditions and steady-state network microstructures. It will be an interesting continuation of this study to investigate those non-linear emergent behaviors in more realistic three-dimensional environments using the dipole theory presented.

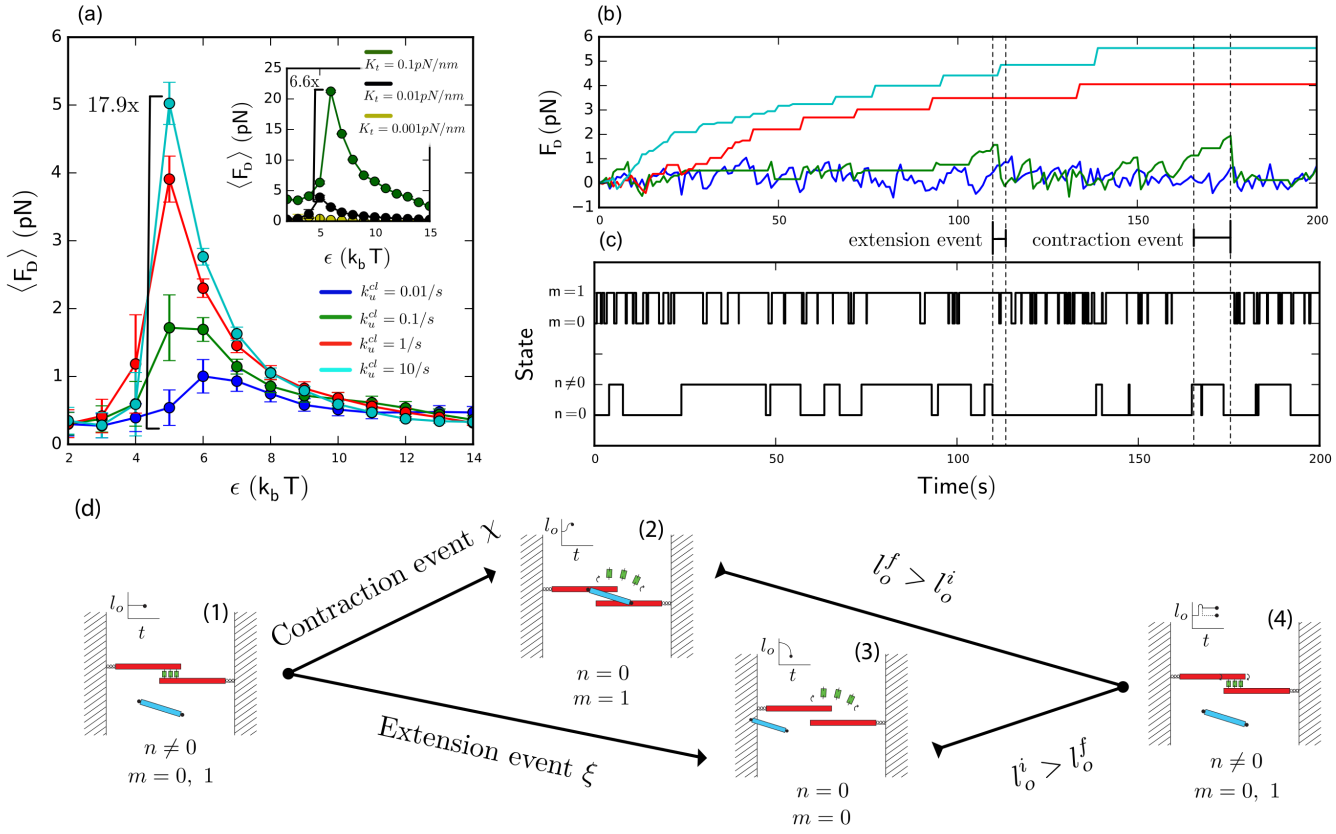


Figure 3.5: a) Variation of average dipole force $\langle F_D \rangle$ produced on $\tau_{lab} = 200s$ shows similar biphasic behavior compared to a pFD, but is amplified greatly due to the presence of the stochastic motor against a 0.01 $pN/nm$ tether. Amplifications from the transient motor force are shown ($\approx 0.3$ $pN$). Inset shows the effect of varying external stiffness of the diplole $K_t$ for a fixed $k_u^{cl} = 1/s$. The catch-bond nature of myosin II is apparent in the overall increase in generated force at high stiffness. b) Stochastic force production of the dipole at $\epsilon = 5\ k_bT$ shows a step-like approach to steady state. Increasing kinetic rates maximize overlap generated on $\tau_{lab}$. c) The corresponding state trajectory of the same force dipole with $k_u^{cl} = 0.1/s$, which correspond to contraction and extension events in b). $m = 0, 1$ represents the unbound and bound states of the motor, respectively. $n = 0$ and $n \neq 0$ represent the cross-linker state. d) The proposed ratcheting process in an active force dipole. (1) The process starts at a stable configuration $n \neq 0$. The motor can be either bound or unbound ($m = 0$ or $+1$). (2) Cross-linkers then unbind from the dipole ($n = 0$). If $m = +1$, a contraction event occurs, contracting the filaments to a new overlap $l_o^f > l_o^i$. (3) If $m = 0$, an extension event occurs in which the filaments lose overlap such that $l_o^f < l_o^i$. (4) Cross-linkers re-bind ($n \neq 0$), stabilizing the $l_o^f$ achieved in (1)-(3) - in a contracted or extended configuration. This process repeats as pairwise overlap is created between the anti-parallel pair, generating contractile force. Figure is from [93], Copyright 2018 American Physical Society.

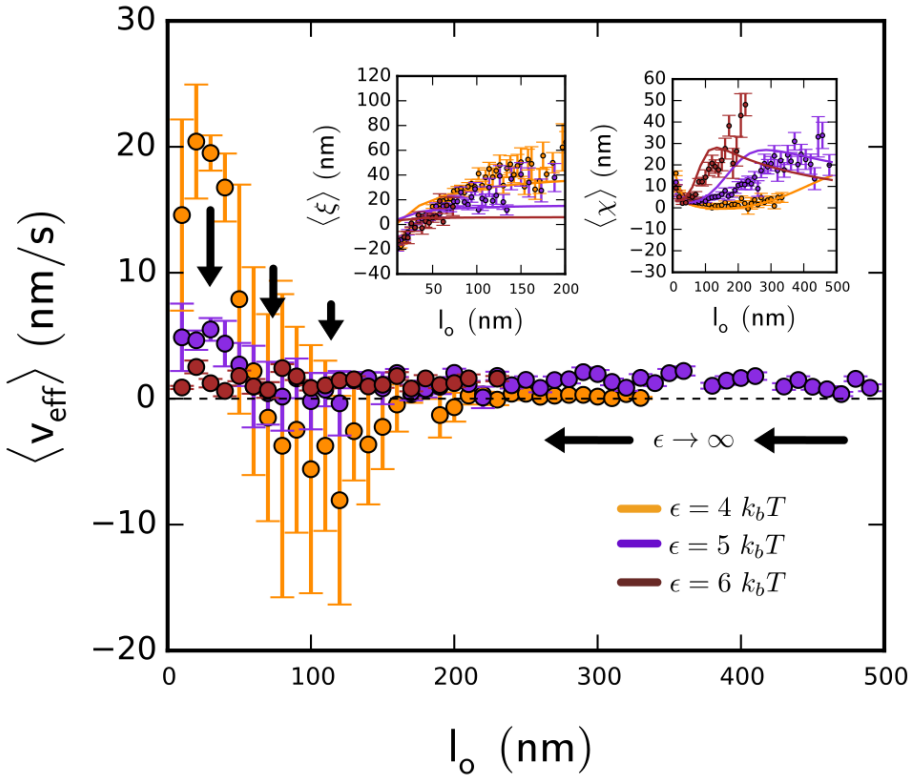


Figure 3.6: Effective inter-filament velocity in the one-dimensional active force dipole as a function of pairwise overlap, with $k_u^{cl} = 10/s$ against $K_t = 0.01\ pN/nm$ tethers. This plot can be interpreted as the contractile force-velocity relation of the structural element, since pairwise filament overlap $l_o$ is directly proportional to the restoring force on filaments due to external tethers. The effective inter-filament velocity of the dipole (i.e. the rate at which filament overlap increases) is calculated by combining the change in overlap and frequency of contraction and extension events: $V_{eff}(l_o) = \chi(l_o) \cdot \omega_\chi(l_o) - \xi(l_o) \cdot \omega_\xi(l_o)$. Cross-linking in an optimal range amplifies forces produced by the dipole and is apparent in the effective contractile velocity of the filament pair at large overlaps. $\chi(l_o)$ and $\xi(l_o)$ are also shown in the inset. Analytic approximations for the expected value of these events are showed as filled lines. Figure is from [93], Copyright 2018 American Physical Society.

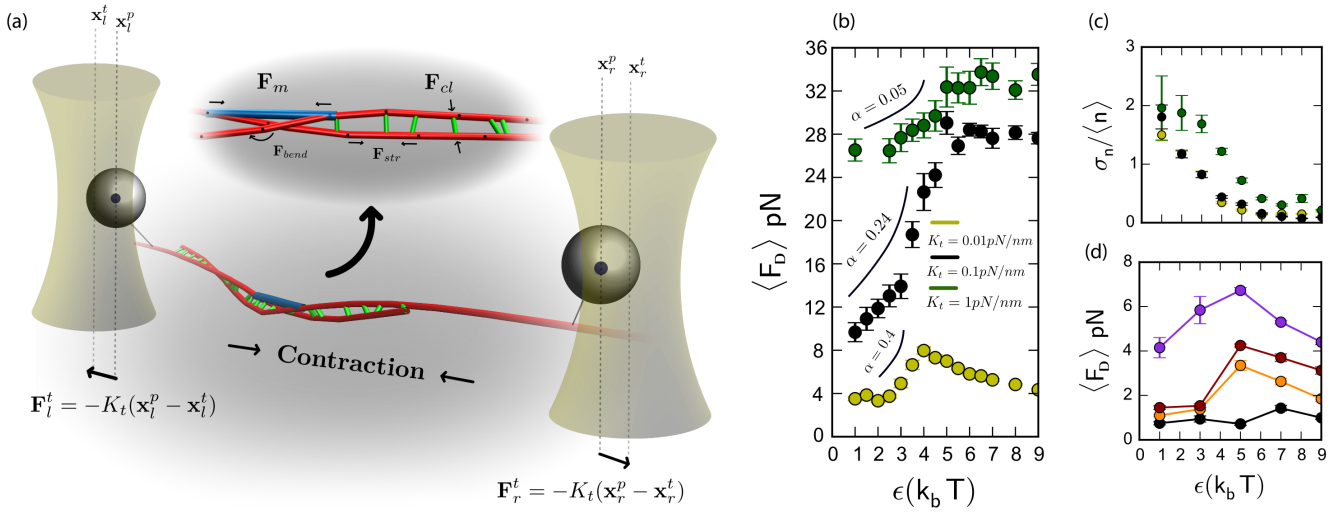


Figure 3.7: a) A schematic of the three-dimensional *MEDYAN* simulation setup, very similar to the one-dimensional model shown in Fig 4.1. Two filaments (red), now containing three-dimensional bending and stretching modes, are oriented to that their plus ends ($\mathbf{x}_l^p = (0,0,0)$ $\mu m$ and $\mathbf{x}_r^p = (4,0,0)$ $\mu m$, respectively at $t = 0$) are connected to elastic, stationary tethers at $\mathbf{x}_l^t$ and $\mathbf{x}_r^t$ (initially $\mathbf{x}_{l,r}^p = \mathbf{x}_{l,r}^t$). As contraction is produced by myosin II filaments (blue) walking towards the plus ends of each actin filament, cross-linkers (green) and actin filaments can bend and stretch according to polymer potentials outlined in Chapter 2. b) The averaged dipole force after $200s$, $\langle F_D \rangle$, is shown as a function of $\epsilon$. The steady-state data follows the power laws $F_D^{ss} \propto (\epsilon P_o^{cl})^\alpha$ where $\alpha = 0.4$, 0.24, and 0.05, respectively for increasing $K_t$. The probability of a single site occupancy $P_o^{cl}$ is given by $(1 + ve^{-\epsilon/k_b T})^{-1}$. A diminishing effect of cross-linker ratcheting is explained by myosin II's ability to increase its binding lifetime under stress, allowing for more stable walking and force generation at $K_t = 1$ $pN/nm$. c) Fluctuations of bound cross-linkers (defined as $\sigma_n/\langle n \rangle = \langle n - \langle n \rangle \rangle / \langle n \rangle$) shows a sharp onset of kinetic arrest at $\epsilon = \epsilon_{lab}$, similar to the one-dimensional case. d) Average dipole force produced for varying initial overlap $l_o^i = 1000$, 500, 200, 0 $nm$, with $l_o^i = 0$ as the top curve. Increasing initial overlap $l_o^i$ will decrease contractile force produced in simulation ($\tau_{lab} = 200s$) due to kinetic friction.Figure is from [93], Copyright 2018 American Physical Society.

# Chapter 4: Moving to a disordered network

*This chapter is adapted from: James Komianos and Garegin Papoian. "Passive and Active Cross-linking Provides the Dual Mechanisms of Actomyosin Contractility". In preparation (2018)*

## 4.1 The contractility problem in three dimensions

As we have discussed throughout the previous chapters, actomyosin is able to produce contractility in a wide variety of disordered structures which lack sarcomeric polarity organization. Most work that we have reviewed points to three constituent proteins being essential in this process: actin filaments, providing the "molecular scaffold" for force generation, active myosin II motors, which cross-link and pull pairwise actin filaments in a directional manner to create "force dipoles", and passive cross-linkers, which cross-link at typically shorter ranges than myosin II and have been proposed to propagate forces throughout a network. Understanding the molecular interactions of these disordered systems and their phase transitions is of great importance to many areas of biomedical research, where motor and cross-linking deficiencies can promote a variety of abnormal cell behaviors [133].

Many theories have been introduced to answer why disordered actomyosin is robustly contractile *in vivo*, all suggesting a symmetry breaking mechanism in

actomyosin force dipoles which can transmit tensile forces and not compressive ones at the network level. Mainly, actin filament buckling under compressive loads [103, 128, 156, 171], myosin II deformation [103] and rotation to stable contractile configurations [40] and the role of actin filament treadmilling in reorganizing actin structures [117, 137] have been proposed to accomplish this task. It has also been shown analytically that a free energy gradient created by passive cross-linker binding can cause filaments to favor overlap in the absence of motors [179, 200], which could provide a thermodynamically driven symmetry breaking mechanism. Being interested in this particular phenomenon, we developed an analytical and computational model of a tethered force dipole, and found when a highly transient myosin II motor is present in a sufficiently favorable free energy gradient, many $pN$ of tension can be produced by the motor ratcheting on the original cross-linker landscape [93]. While one can imagine such a mechanism could tune the phases of contractility in a disordered network, we still have little understanding of how a disordered system of those dipoles can organize in three-dimensional space and subsequently develop network-level mechanical tension. This collective process may be telescopic in nature on an *in vitro* length scale (tens of $\mu m$), with contractile velocity scaling with area [110] or bundle length [182]. In a small enclosed volume such as the cytokinetic furrow or actin cortex ($2 - 5\mu m$), however, we also should consider the diffusivity of force dipoles and subsequent inter-dipole aggregation must be investigated in contributing to network organization.

To begin to answer this question, it is also helpful to explicitly consider the nature of macroscopic contractile behavior in many works. Actomyosin network

contractility has been studied *in vitro* as mostly an inward, geometric collapse of actomyosin networks with no tethering to external substrates [4, 12, 48, 89, 90, 171]. Other works have described contractility in reconstituted networks as the production of tensile force against such mechanical constraints [128, 182]. Likewise, in modeling actomyosin contractility, many studies measure negative normal stress produced by a disordered network on stiff boundary conditions [40, 82, 103] whereas some study free-boundary, aggregative processes [102, 203, 204], even in full or partial periodic boundary conditions [82, 176]. While all of these networks are "contractile" in a broad sense, to investigate the detailed emergence of contractility and its requirements, a clear differentiation must be made between geometric collapse, which may require minimal internal dipole tension, and tension generation against an external resistance. We must consider that an actin network may require various sets of cross-linking components to achieve both types of contractility. This consideration will resolve an accurate phase map of all possible modes of contractile behavior, since it is likely that both mechanisms are harnessed by a cell, such as when free networks are developed by cofilin severing actin filaments [139, 155], or when actin filaments are highly tethered by linkers to a membrane in the cortex area [160].

Using the distinction presented, in this Chapter, we describe a phase diagram elucidating the dual mechanisms of actomyosin contractility and their dependence on cross-linker affinity, motor driving, and boundary tethering conditions. Our main result is that the combinations of cross-linking included in a network, passive or active, can directly tune these dual mechanisms. In particular we will show that active force dipoles containing uni-directional myosin II are not necessarily

needed to induce large-scale geometric collapse of an actin network if passive cross-linking is present. However, these force dipoles are essential in generating network tension against external tethering to hard-wall boundaries, with added consequence of super-diffusive dipole motion and network geometric expansion. Comparing the contractile behaviors in each part of the phase diagram, we display the properties of a contractile energy landscape created by passive cross-linking in the disordered network, closely following the dipole energy landscape derived in [93].

## 4.2 Disordered network setup

We use the *MEDYAN* active network model [148], as shown in Fig 4.1, to generate an *in silico* actomyosin network containing the essential components involved in actomyosin contraction: (1) dynamically polymerized and semi-flexible actin filaments, coarse-grained into cylindrical segments, containing bending and stretching modes and a novel volume exclusion of segments, (2) passive cross-linkers that can stochastically bind and unbind to pairwise filament segments within $35 \pm 5nm$ and (3) active motors, kinetically modeled as transient, uni-directional non-muscle myosin II, can stochastically, bind, unbind, and walk between filament segments within $200 \pm 20nm$, generating network stress. All cross-linkers and motors are represented as harmonic bonds between actin cylinders, with binding, unbinding and walking governed by a Gillespie stochastic simulation algorithm [64]. As in recent modeling efforts [148], to represent the stochastic (un)binding dynamics of motors which are in reality coarse-grained mini-filaments with a number of individ-

ual motor heads, we again use a simplified version of the Parallel Cluster Model of Erdmann et al. [49] as in Chapters 2 and 3. This mechanochemical model takes into account the transient nature of small myosin II filaments, as well as explicit catch-bond nature of actin-myosin bond [68, 95].

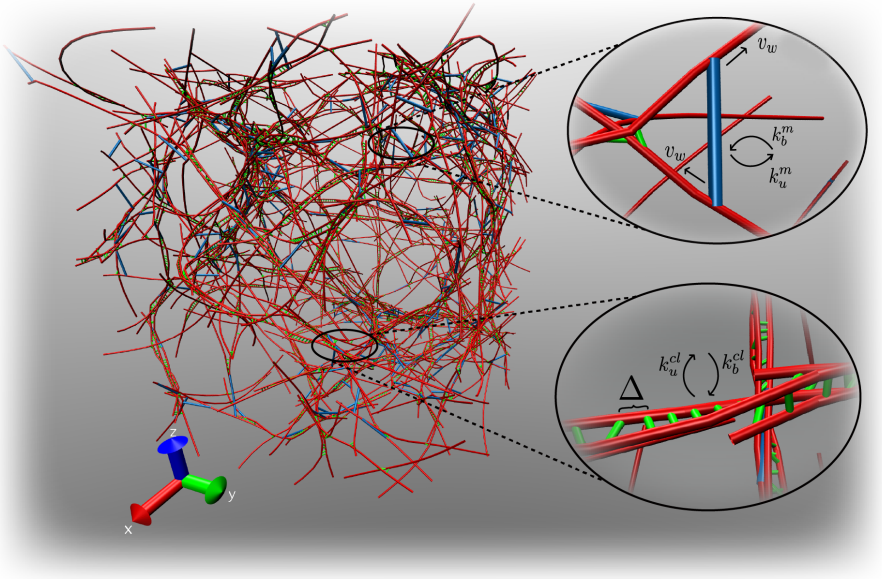


Figure 4.1: Actomyosin contractility investigated using *MEDYAN* computer simulations. In the model, semi-flexible actin polymers (red) can be reversibly linked by passive cross-linkers (green) with kinetic rates $k_u^{cl}$ and $k_b^{cl}$ and displaced by active myosin II motors (blue) which walk along filaments with velocity $v_w$ and can reversibly (un)bind with rates $k_u^m$ and $k_b^m$. The separation between binding sites for both active and passive molecules on actin filaments is $\Delta = 21nm$. Mechanochemistry of cross-linkers and motors closely follows previous work [93]. Mechanical deformations produced by local motor motion adiabatically follow stochastic chemical reactions as they occur. All simulation details are given in Supplemental Information.

The *MEDYAN* simulation protocol iteratively performs stochastic-reaction diffusion simulation and equilibrates the resulting mechanical deformations, due to localized motor motion, after a set of chemical events. Details of the simulation protocol are given in Appendix and details of mechanochemical models used in our work are given in [93]. All disordered actomyosin networks were simulated for $\tau_{sim} =$

$1000s$ in a cubic 27 $\mu m^3$ enclosed reaction-diffusion volume with steric boundary repulsion using 12 $\mu M$ actin monomers and 400 initial filaments, 1 $\mu M$ cross-linkers, and 2 $\mu M$ myosin II, where the latter are coarse-grained as bipolar mini-filaments with $N_t = 30$ heads per side. In general, most networks reach steady state (or kinetic arrest in some phases) after $700s$ (indicated by saturating $R_g$, number of cross-linkers bound $n_{cl}$ and $\sigma_w$ vs. $t$), where we subsequently perform our analysis. For each chemical configuration of cross-linking, motor activity, and boundary conditions, 4 independent trajectories were run. Configuration output, including coordinates of all reacting elements and compartments of species are output every $t_s = 5s$ of simulation time. Together, approximately $150,000$ hours of computing time were used on Maryland's Deepthought2 cluster for these simulations.

## 4.3 Geometric collapse.

First we focus on conditions required for geometric collapse in an actin network with no tethering to its boundaries. This will describe the first half of the phase diagram. Initially we expect that geometric collapse in such a configuration should depend strongly on the strength of cross-linking, and spontaneous overlap formation of actin filaments should be biphasic in nature with respect to that parameter [93]. So, a good parameter choice is $\epsilon$, the binding energy of passive cross-linkers, which relates to the stochastic on-off rates in simulation as $K_D = \frac{k_{off}}{k_{on}} = \frac{v_b}{v_m} e^{-\epsilon/k_b T}$ [93]. We use a fixed $k_{off} = 1/s$ and molecular constants $v_b$ to represent the approximate bound volume of the cross-link to actin and $v_m = V/N$ to represent the monomer

volume in solution. The form presented takes into account entropic and enthalpic contributions of the cross-linker's free energy of binding.

A strong first-order transition to geometric collapse exists in simulation data for increasing $\epsilon$. We measure the contraction of the network by its radius of gyration: $R_g^n = \left\langle (\mathbf{r}_i - \mathbf{r}_{GC}^n)^2 \right\rangle$, where $\mathbf{r}_{GC}^n$ represents the geometric center of mass for the entire network of actin, and averaging occurs at steady state $\tau_{ss} = 700s$. This transition follows the power law $R_g \propto \epsilon^{0.66}$ as shown in Fig 4.2. Looking more closely at the individual polymer radius of gyration $R_g^p$, defined as the average radius of gyration of a single polymer chain in the network, there is a noticeable transition at $\epsilon = 6k_bT$ to buckled filaments. Together this shows significant contraction by favorable filament sliding before this threshold (for example, at 6 $k_bT$, $R_g$ had decreased by 25 percent while $R_g^p$ decreased by under 2 percent). Beyond the transition point, motors are able to further buckle filaments into highly aggregated three-dimensional states, with saturation of $R_g^n$ and $R_g^p$ at high cross-linker affinities. For the duration of the chapter we will use $\epsilon_{lab} \approx 6k_bT$ as in Chapter 3 to represent the energetic contribution of cross-linking which creates buckled networks at $\tau_{ss} = 700s$. This transition to kinetically arrested structures can also be observed in the development of long-range displacement correlations above $\epsilon_{lab}$ as shown in $\Gamma(r, \Delta t)$ (calculation and plots are shown in Fig C.4).

The requirements for geometric collapse of free-boundary actomyosin can be further tested using non-physiological bi-directional motors which walk in either plus or minus end direction on actin filaments as opposed to the physiologically motivated uni-directional motor. In our simulation setup, bi-directional motors include the

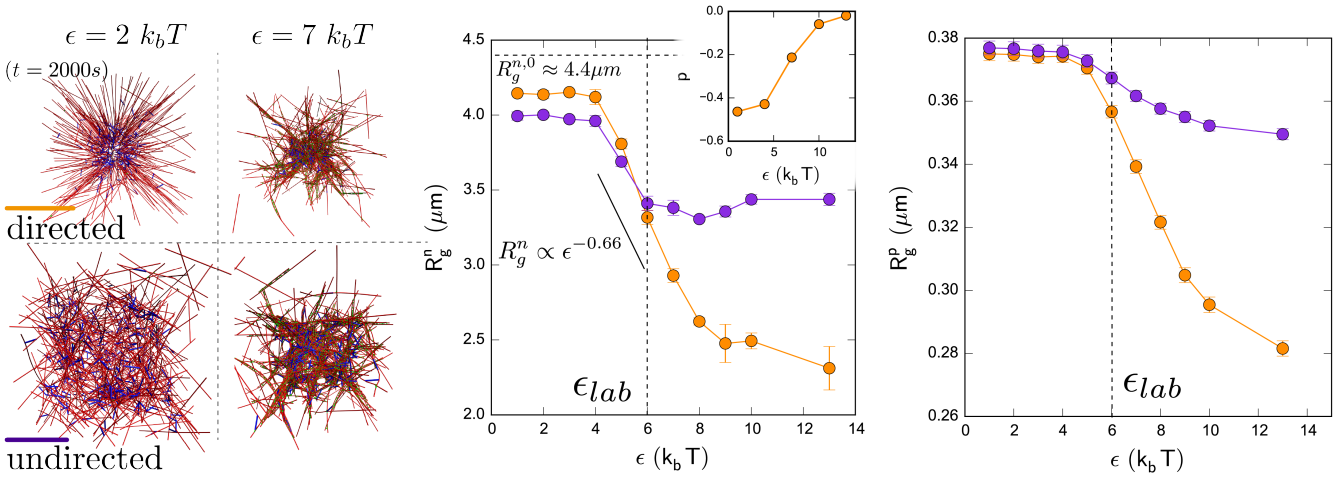


Figure 4.2: Actomyosin geometric collapse with free boundaries as a function of cross-linker binding energy $\epsilon$. Left: Snapshots (at $t = 1000s$) of various steady-state configurations with bi- and uni-directional motors. Uni-directional motors are able to produce aster structures if run to $t = 2000s$ when $\epsilon < \epsilon_{lab}$, where $R_g^n$ changes minimally after $1000s$. Center: Network radius of gyration $R_g^n$ as a function of $\epsilon$ for bi- and uni-directional motors at steady state. Both types of motor driving give a power law $R_g^n \propto \epsilon^{-0.66}$ in the regime $\epsilon < \epsilon_{lab}$. Inset shows strong transition from radially polar to non-polar structure observed at $\epsilon_{lab}$. Right: Individual polymer $R_g^p$ as a function of $\epsilon$. A transition to buckling at $\epsilon_{lab}$ is found for the uni-directional motor case, which differs significantly from bi-directional motor architecture.

same mechanochemical models for catch bond and stall velocity behavior (in both stepping directions). While losing the "sarcomeric"-like organization of force dipoles provided by uni-directional motors, a similar $R_g^n$ contraction pattern results in the bi-directional motor case following the power law $\epsilon^{-0.66}$ in Fig 4.2. This contractility also occurs in absence of significant buckling events (less than five percent decrease in $R_g^p$ for all chemical configurations). A divergence in the collapsed structure above the defined $\epsilon_{lab}$, however, arises due to the inability of bi-directional motors to buckle filaments via sustained directional stepping. In all, we have displayed that if motors are sufficiently transient, collapse is similar with bi-directional and uni-directional motors when $\epsilon < \epsilon_{lab}$. A divergence in collapsing behavior at $\epsilon_{lab}$ is also apparent

in both the $g(r)$ pairwise density distributions for the network of cylinders in both motor cases (calculation and plots are shown in Fig C.4).

The last consideration for a network with free boundaries is the polarity organization of resulting microstructures. To measure polarity organization we define a polarity measure $p$ based on the normal direction $\mathbf{n}_i$ from minus to plus end of the $i$th cylinder $p = \left\langle \mathbf{n}_i \cdot \mathbf{n}_r \right\rangle$ where $\mathbf{n}_r$ is a radial vector from the center of the volume outward to the cylinder point. Overall, structures developed by uni-direcitonal motors have strong polarity as observed in $p$ (Fig 4.2) when $\epsilon < \epsilon_{lab}$, as compared to bi-directional motor driving which cannot organize filament polarity. This is intuitive since uni-directional motors can migrate towards actin filament plus ends. However, we notice that full polarity organization is on a different timescale than the highly aggregative processes observed around $\epsilon_{lab}$ and above. If run for $2000s$ simulation time, which is achievable in our framework when $\epsilon < \epsilon_{lab}$, actomyosin networks form nearly perfect aster structure with minimal radius of gyration change from the original $\tau_{sim} = 1000s$ (shown as snapshot in Fig 4.2).

## 4.4 Network tension.

It is clear that networks can geometrically collapse with uni- or bi-directional motors if sufficient passive cross-linking is present. How does the nature of contractility change when the filament network is tethered to its boundaries? Generation of tension against such a boundary may rely on a different mechanism beyond the geometric collapse of a network. To test tethered boundary conditions

and its dependence on motor driving and $\epsilon$ in the next half of the phase diagram, we ran another set of simulations, attaching any filament end within 250 $nm$ of a boundary after $10s$ of simulation time. Filament ends denoted as $\mathbf{x}_i$, are pinned to their instantaneous positions $\mathbf{x}_i^0$ by elastic tethers with a restraining potential $U^{wall} = \frac{K_t}{2}(\mathbf{x}_i - \mathbf{x}_i^0)^2$. We use a tether stiffness $K_t = 1pN/nm$. This restraining potential on all tethered filament ends is then included in mechanical equilibration of the network following stochastic chemical dynamics. As tension is created in the elastic tethers, a total (normal) contractile stress exerted by the network can be calculated as $\sigma_w = \frac{1}{A}\sum_{i=1}^{N_t} K_t(\mathbf{x}_i - \mathbf{x}_i^0) \cdot \mathbf{n}_s^i$ where $N_t$ is the number of initialized tethers at $t = 10s$, $\mathbf{n}_s^i$ is a normal vector of the corresponding surface (pointing inward) connected to the tether, and $A = 54\mu m^2$ is the total surface area of the enclosed simulation volume.

A main result from our recent work [93] was that passive cross-linking in absence of motor activity should produce a "passive" dipole force $F_D \propto \epsilon P_o^{cl}$ in a pair of tethered actin filaments, where $P_o^{cl} = (1+\frac{v_m}{v_b} \cdot e^{-\epsilon/k_bT})^{-1}$ represents the probability of occupancy for a single pairwise binding site [93]. This relation represents that for a distance between cross-links $\Delta$ a filament pair experiences a mean-field driving force of thermodynamic nature $\epsilon P_o^{cl}/\Delta$. So, we expect that tension generation in a bi-directional motor network should also be strongly dependent on cross-linker energy. Plotting the steady-state wall stress as a function of cross-linking energy, we obtain a near-linear power laws $\sigma_w \propto \epsilon$ in the bi-directional motor case. While a strong agreement with our prediction, the power law is independent of $P_o^{cl}$. This could likely due to an overall network fluidity and loss of dipole organization compared

to one dimension, disallowing resolution of single dipole interactions. But, overall, dipole contractility based on the energetic contribution of cross-linker binding is manifested in the disordered network.

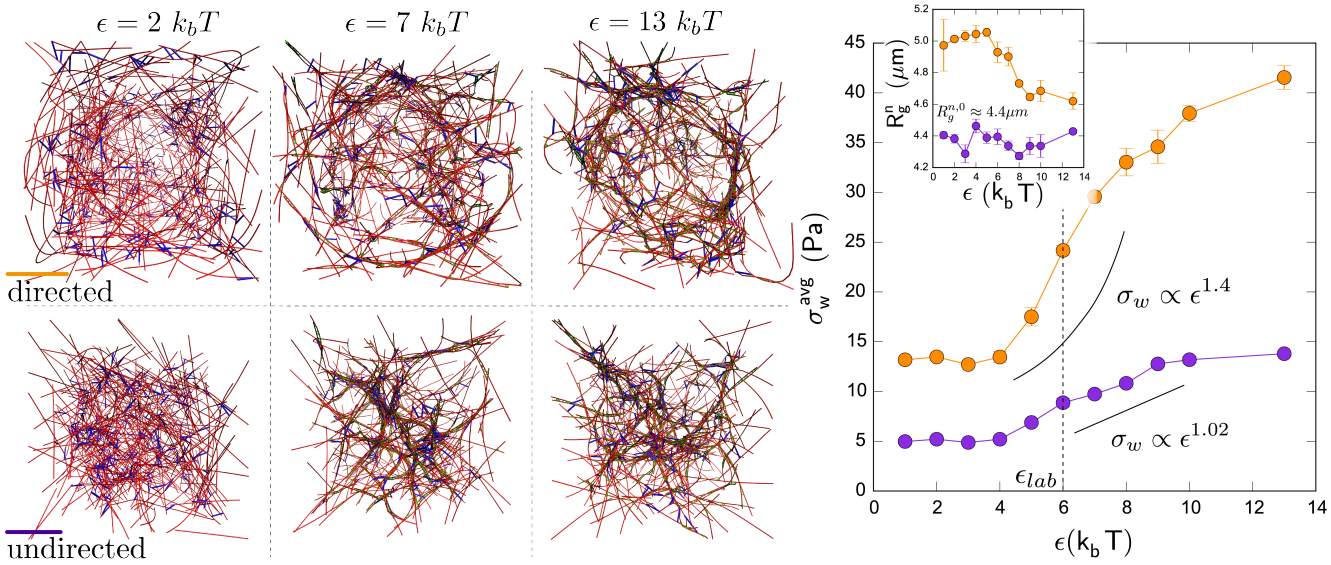


Figure 4.3: Network tension generated by tethered-boundary actomyosin. Left: Snapshots of networks under $1pN/nm$ boundary constraints of periphery filaments for varying $\epsilon$. Bi-directional motors produce significant actin reorganization and bundling in the center of the simulated volume, compared to uni-directional motors which expand to boundaries at all $\epsilon$ simulated. Inset on the right shows $R_g^n$ for both networks, displaying significant geometric expansion in the uni-directional motor case. Right: Average wall stress $\sigma_w^{avg}$ at steady state as a function of $\epsilon$. A dependence on $\epsilon$ is observed for both types of motor driving ($\sigma_w \propto \epsilon^{1.4}$ and $\sigma_w \propto \epsilon^{1.02}$), in agreement with a derived energy landscape driving force dipole tension [93].

Last we compare the bi-directional vs uni-directional tension generation in a tethered-boundary network. By our previous work there should be a large amplification of the original passive dynamics at a similar transition energy when using uni-directional motors. Uni-directional motors at all $\epsilon$ are able to produce up to a three-fold increase in contractile stress generated in $\tau_{sim}$ in comparison to bi-directional motor filaments. This occurs in absence of difference in average walk

length or bound time of motor (distributions of these variables at steady-state shown in Fig C.1). A power law $\sigma_w \propto \epsilon^{1.4}$ is obtained in this case, showing similar transition energy compared to bi-directional motors. Along with increased force generation by an apparent ratcheting mechanism of the uni-directional motor-cross-linker system [93], networks driven by uni-directional motors significantly *expanded* within the boundary geometrically and do not display collapse. This would be initially difficult to deem as contractile without differentiating between mechanical tension production and geometric collapse. In this case, while boundary dipoles are mostly constrained by tethering, interior dipoles that are not tethered can be super-diffusive and expand to boundaries for overall geometric expansion of the network. Super-diffusive MSD values of actin filaments in the uni-directional motors are shown in Fig 4.4. In comparison, no geometric expansion nor collapse is observed in these bi-directional motor systems and MSD values indicate a passive diffusive process of bundle generation. This is also plotted in Fig 4.4.

## 4.5 Discussion

Our main question in this work was how can actomyosin force dipoles organize to produce the dual mechanisms of contractility, identified as geometric collapse and tension generation. The phase diagram constructed for our simulations representing these mechanisms is shown in Fig 4.5. The main factors involved are cross-linking energy ($\epsilon$), motor directionally (UD/BD), and boundary tethering (FB/TB). In particular, under free boundary conditions uni-directional motors can aid but are not

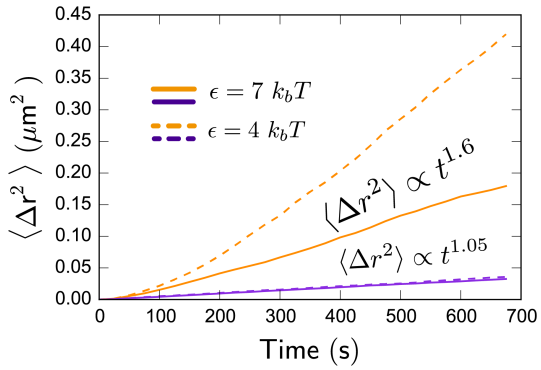


Figure 4.4: Mean-square displacement of actin filaments for various cross-linking energies in a tethered-boundary network. The same color scheme for uni-directional and bi-directional motor motion are used. Actin filament MSD values are calculated as $\left\langle \Delta r^2(t) \right\rangle = \left\langle [\mathbf{r}_i(t) - \mathbf{r}_i(0)]^2 \right\rangle$. When uni-directional motors are present, networks can remain super-diffusive due to interior dipole super-diffusion. In the case of bi-directional motors, ratcheting cannot occur and networks remain diffusive.

needed in such a passively driven collapse mechanism unless kinetic arrest is present $\epsilon > \epsilon_{lab}$. However, when tethering of boundary filaments occurs, uni-directional motors are required for a ratcheting mechanism [93]. A consequence of this ratcheting is that interior dipoles become super-diffusive, providing an expansive network geometry within the enclosed volume. Together, in all parts of the phase diagram, networks contracted following an energy landscape due to cross-linking, derived as the free energy gradient of pairwise filament overlap [93]. As a supplement, we also have simulated variations in bending modulus of actin filaments to test the contributions of a buckling mechanism [105,128,182] in tension generation as well as collapse of a network with static cross-linking which is assumed by a recent model [48]. We have shown that static cross-linker connectivity can create an altered phase behavior with respect to cross-linker presence, indicating an importance of transient linkages creating a favorable landscape for overlap formation. These cases are both shown

in Fig C.2.

Based on this analysis, we propose an *in vitro* oil drop experiment to confirm our simulation results with respect to the predicted phase behavior as a function of cross-link binding energy $\epsilon$, or somewhat equivalently of cross-linker concentration. This experiment could prepare an actomyosin network with cross-linking and uni-directional myosin II motors in a capillary between two drops of oil as done with a cytoskeletal extract in [12]. We believe it is essential that these motors be non-muscle myosin II mini-filaments due to significantly differing kinetics between non-muscle and muscle filament assemblies. In this experiment, one could alter the stiffness of the oil droplet surface by modulating its solvent composition, similar to our *in silico* setup when adding tethering to boundaries. In the stiff boundary case one could then obtain the Laplace pressure of this oil and water interface as a function of $\epsilon$ by measuring its overall curvature. In particular, we expect the predictions $R_g \propto \epsilon^{0.66}$ under near-zero resistance and $\sigma_w \propto \epsilon^{1.4}$ under significant resistance to hold if cross-linker kinetics is varied in accordance with our derived expression. If filaments are tracked using super-resolution fluorescence microscopy methods during this experiment, we should observe a biphasic filament velocity dependence on $\epsilon$ (shown in Fig C.5).

It is worth addressing the lack of biphasic contractility in our simulations, compared to other in vitro [12, 48, 89] results, and even our own analytically-motivated study of a single force dipole [93], showing that cross-linking beyond a certain threshold value inhibits overall contractility of actomyosin. In this study, we found that contractility is robustly monotonic with respect to cross-linker binding strength,

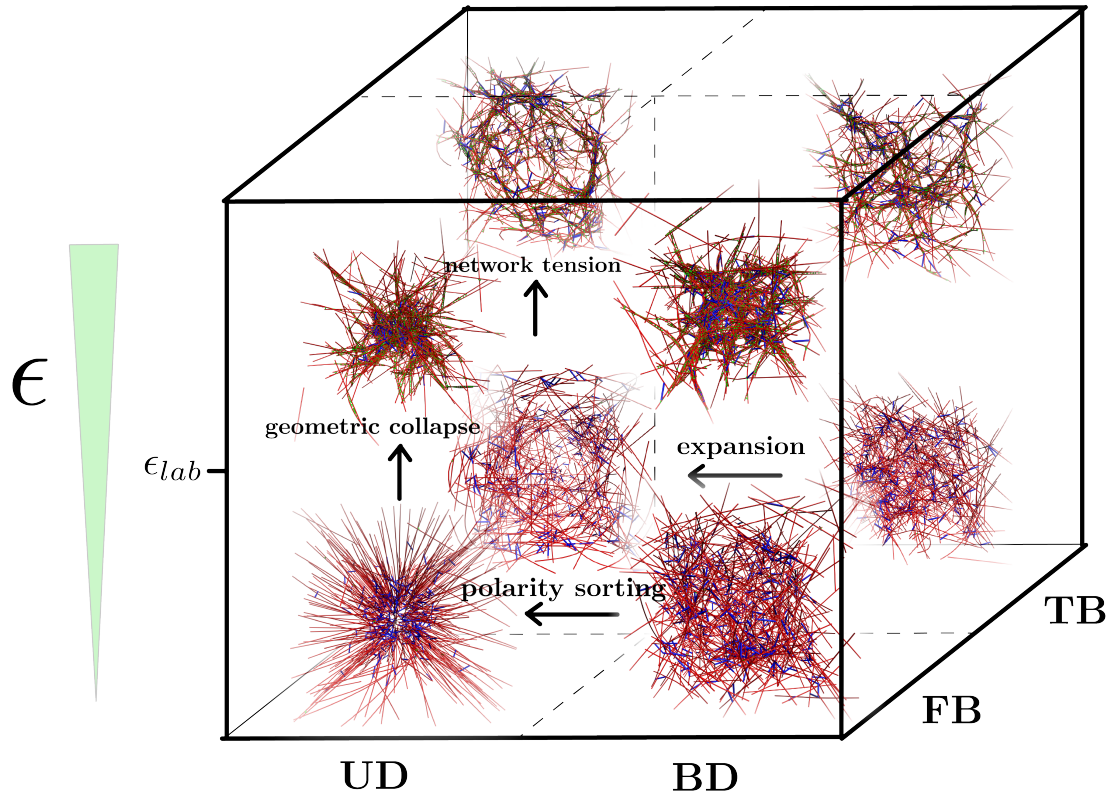


Figure 4.5: Phase diagram actomyosin contractility mechanisms constructed from disordered network simulations. The main axes of the diagram are cross-linking energy ($\epsilon$), motor directionally (UD/BD), and boundary tethering (FB/TB). Front: Free-boundary regions of the diagram display similarity between bi- and uni-directional dynamics under $\epsilon_{lab}$, with the latter developing polar aster structures. Above $\epsilon_{lab}$ networks with either motor condition collapse, and uni-directional motors are able to buckle filaments into highly collapsed structures. Back: In tethered-boundary networks, disparity in contractile behavior with respect to motor directionality occurs due to a dipole ratcheting mechanism of the uni-directional motor. This super-diffusive behavior creates net network expansion and highly increased tension. Bi-directional motors in the tethered case produce an aggregating process with moderate tension generation.

except (marginally) for the bi-directional motor case under free boundary conditions. This could be related to the difference in length scales when comparing *in silico* vs *in vitro* studies. One could imagine that our simulations are well below the length scales to observe percolation transitions [5], and on length scales comparable to a single actin filament, a network can always robustly collapse by the forced unbinding of cross-linkers by local motor motion. This may not be possible in larger macro-scale connected structures that have many inter-connected filament units. But, since we predict that $\approx 3\mu m$ contractile clusters would have polar structure when $\epsilon < \epsilon_{lab}$ and not otherwise, the subsequent contraction of sub-domains at larger length scales ($10\mu m$ or above) could in fact be biphasic - when transitioning through $\epsilon_{lab}$, polarity of local clusters would become disordered, thus eliminating all anti-parallel filaments connecting those clusters. This must be investigated with larger simulations of disordered actomyosin.

While little quantitative study exists in *in vivo* with regard to variation in cross-linking properties altering actin microstructure of live cells, mutations of actin cross-linking proteins have produced monotonically altered cellular stress responses using traction microscopy [9, 46]. Experiments of this nature will be interesting to study in future work, possibly using a detailed membrane and focal adhesion model combined with the actomyosin phase behavior presented. Biphasic contractility with respect to cross-linking strength, however, to the best of our knowledge, has not been observed *in vivo*. To deepen our understanding of the dynamics of these complex cytoskeletal systems, our modeling should be improved to include realistic effects of actomyosin contractile behavior from both a biochemical and physical perspective.

This includes accurately studying the kinetics of non-muscle myosin II assemblies *in vitro*, modeling the effects of specific biochemical regulators of the actin and motor filament complexes *in vivo*, as well as hydrodynamic effects of filament motion which may produce altered microstructures and dynamics in actomyosin aggregates. Finally, time-resolved super-resolution imaging of individual actin filaments inside a cell along with *in vitro* work will lead to deeper insights into intra-cellular dynamics.

# Chapter 5: Final discussion and outlook

In this thesis we have considered the physical modeling of complex actomyosin processes and their emergent behaviors. The need for a cytoskeletal modeling framework which contained truly mechanochemical coupling for its constituent filaments, including cytosolic reaction-diffusion and polymer mechanics, was clear and we hope that our simulation framework *MEDYAN* fits this need (summarized in Chapter 2 discussion). This has allowed us to consider a number of phenomenon that would have not been possible otherwise, including actomyosin polarity alignment transitions due to the interplay of filament treadmilling and motor activity and the emergence of contractility due to transient cross-linking. Along with the research presented in this work, the *MEDYAN* framework as a software package has been developed and documented for easy use by cytoskeletal researchers. Since its inception in 2016, it has been used by researchers at the University of Maryland, Rice University, Georgia State University, and Ohio State University. The codebase currently has over 15 active branches to develop new cytoskeletal simulation tools and analysis. We hope that the framework will be used to study many cytoskeletal systems, including microtubule networks and intermediate filament systems along with the already shown actin-based microstructures.

In the future, efforts to advance *MEDYAN* could mainly focus on membrane morphology and the coupling of a membrane with focal adhesions to approach modeling full cellular structures such as contracting motile cells. Focal adhesions are heterogeneous protein structures, connected in the cell interior to actomyosin bundles, which regulate force transmission to the extracellular matrix as well as help in sensing environmental stiffness [61, 76]. While traction forces on a substrate can be measured in motile cells, it is typical that overall motility of a cell and traction forces has no simple correlation to actin or focal adhesion density [69]. Modeling such mechanochemical structures in *MEDYAN* can take steps in uncovering this black box. For this type of advanced modeling, membrane deformation due to the actin cytoskeleton must be accurately performed, while also enforcing a rigorous exclusion among actin filaments, the membrane surface, and focal adhesion sites. Crossing of those elements, similar to the problem of non-crossing among pairwise actin filaments, could occur readily during polymerization of a leading edge into the membrane or filament buckling in the focal adhesion site. Members of our lab (Haoran Ni and Aravind Chandrasekaran) have recently begun a coarse-grained membrane model and focal adhesion model for *MEDYAN* to pursue simulations of this nature.

For many future scientific goals computational complexity will be an issue, and continual modeling improvements will be made to implement efficient algorithms for the complex assembly and dynamics of cytoskeletal filaments. In particular, GPU computing can speed up many-particle computations involved during mechanical equilibrations and volume exclusion calculations. Recently a member

of our lab (Aravind Chandrasekaran) has used GPU computing to parallelize the original mechanics equilibrations of *MEDYAN*, achieving over 100+ fold speedup in large actomyosin networks containing components presented in this work. This will allow for timescales achievable to observe *in vivo* actomyosin processes on the order of 5-10 $\mu m$ in length for the simulated domain. We believe with this addition have out-reached the timescales of many other competing actomyosin modeling approaches [48,82,132,176], still on a single CPU core. Of course beyond computational efficiency, to represent accurate cellular dynamics in a general cytoskeletal network, hydrodynamics of the assemblies may also need to be considered along with membrane and filament deformations. This is conceivable to combine with *MEDYAN* by using Lattice-Boltzmann particle streaming methods interacting with cylindrical actin filament segments, or by adopting a Langevin-based polymer scheme as in other works [82,132]. An excluded volume model of myosin II and its true dumbbell structure along with actin might also allow for more realistic modeling of bundles and dense, kinetically arrested assemblies. With these additions, we will be able to approach the morphological modeling of full live cells with all main cytoskeletal components in 3-5 years.

We believe that the emergence of contractility in disordered actomyosin based on cross-linker free energy gradients (summarized in Chapter 3 and 4 discussions) is a plausible mechanism to occur inside cells. This mechanism relies on the ability of cross-linkers, through binding and unbinding processes, to create a funneled landscape towards overlapped filament states. This can then be amplified by motor filaments walking transiently on actin, generating a collective ratcheting mechanism

against external tethering. As shown in a disordered network in Chapter 4, along with reorganization and expansion of a ratcheting network, this mechanism can also induce the geometric collapse of networks against free boundary conditions, dependent on the same landscape. In the future, other passive forces merit consideration in an actin network as well, including entropic forces as shown in microtubule networks [101]. But, this must be considered carefully in actin networks due to the helicity of actin filaments, which may disallow cross-linker diffusion between binding sites. Overall, based on our theory, there are some testable predictions for the force generation and organization of actomyosin-cross-linker networks when controlling cross-linking. To test our simulation results, *in vitro* actomyosin networks can be setup with short actin filaments (under 1.5 $\mu m$) and non-muscle myosin II (mini-filaments of 28-30 heads explicitly) to explicitly recreate 1) the alignment mechanisms presented in Chapter 2, possibly at various concentrations of capping proteins which would alter turnover rate of filaments and 2) the force produced by actomyosin when altering concentrations of cross-linker, first in an optical trapping setup with two filaments, or oil-drop disordered network experiment as presented in Chapters 3 and 4. This should be done using PALM/STORM super-resolution methods [16, 209] to accurately resolve filament microstructure and motions within a few $nm$. We would hope that future studies could investigate the dynamics of non-muscle myosin II mini-filaments on a molecular level further as well, also using more optical trapping experiments to measure mini-filament force generation and residence times to input into our coarse-grained stochastic models.

We finally briefly discuss outstanding questions related to the dynamics of an

actomyosin network. Recently it has been found that phase separation of myosin isoforms in an actomyosin occurs in many cell types [92, 167, 191]. This mechanism of phase separation in an actomyosin network has been shown to organize the polarity of cells in motility, and when myosin IIB is inhibited, motility is halted and cells tend to significantly decrease their projection area as recently shown by Shutova et al [166]. We have studied this using *MEDYAN* in the past year, demonstrating the ability for kinetic variations in myosin II isoforms to produce altered actin microstructures, which is testable *in vitro*. But, kinetic behavior or mechanosensitivity differences, even in mixtures of myosin IIA/IIB in simulation, could not produce phase separating behavior in our *in silico* experiments. Based on these mostly negative results, we believe that a plausible mechanism for the phase separation of these networks is copolymerization of myosin II isoforms into heterogeneous filaments as suggested by Shutova and Svitkina [166]. This hypothetically occurs due to the fast recycling of myosin IIA at the cell front while myosin IIB sustains attachment to rear-ward flowing actin bundles. This copolymerization will be explored with *MEDYAN* in the near future when combining with membrane mechanics and focal adhesion models. In recent work we have coded the functionality of heterogeneous myosin II polymerization into our simulation framework.

Another interesting consequence of the non-equilibrium nature of actomyosin is the ability to form pulsatile contractions *in vivo*. For example, it has been shown that pulsing contractions are responsible for many types of signaling in tissue morphogenesis [10, 116]. The type of motor driving directly affects pulsatile contraction, as myosin IIA is necessary for pulsatile behavior and not IIB [10]. Physically, it is

plausible that the combination of myosin II activity and actin filament turnover produces pulsatile contractions due to cycles of contraction, filament disassembly and subsequent formation of new filaments. Along with investigating the phase separating of myosin IIA/IIB inside cells, we hope to uncover pulsatile contractile behaviors with our modeling approach. To fully model this type of system, recent membrane modeling efforts may need to be included, as well as adhesion models to link actomyosin assemblies to it in a realistic manner - it is possible that collective mechanosensing between cells and reorganization of actin networks plays a large role in this pulsatility. In general, the ability of cells to form actomyosin microstructures that result in such non-linear behaviors will be of interest to researchers in the near future.

# Appendix A: Supporting information for Chapter 2

## A.1 Model details.

### A.1.1 Chemical model details.

Simulation space is divided into discrete compartments, with the Kuramoto length chosen in a similar manner as recent work [77]. We do not consider mechanical interactions between diffusing chemical species, or their exact positions within the compartments. The compartment size is fixed throughout the simulation. The polymers in the system do not move or slip in the simulation space unless acted on by an external force, which is controlled by the potentials outlined in the Mechanical Model. All reactions are chosen and controlled by the Gillespie algorithm [64, 65]. Diffusion (and other forms of transport), polymerization, capping, and branching nucleation reactions occur as in previous work [77, 78, 100, 210, 212]. The chemical reactions new to the MEDYAN model are outlined below:

- If we denote $L$ and $M$ as cross-linker and motor species, respectively, the binding and unbinding reactions can be described as follows:

$$P_1 + P_2 + L \leftrightarrow P_1 L P_2, \text{and} \tag{A.1}$$

$$P_1 + P_2 + M \leftrightarrow P_1 M P_2, \tag{A.2}$$

where $P_1$ and $P_2$ are both polymers. Both equations A.1 and A.2 assume that the polymers are within the reaction range of this cross-linker or motor species.

- A motor can walk along either polymer it is bound to with the following form:

$$M_n \leftrightarrow M_{n+1}, \tag{A.3}$$

where $n$ denotes the binding site on the polymer. This implicitly assumes that the next binding site to move to on the polymer is not occupied. The rates of these reactions can be affected by external stresses as well.

- A non-branching filament nucleation reaction can occur in the bulk where two monomer species bind to form a new polymer. This reaction can occur with the following form:

$$X_1 + X_2 \rightarrow P, \tag{A.4}$$

where $X_1$ and $X_2$ are any diffusing species in the system. This creates a new polymer $P$ with chemical composition $X_1 X_2$. Nucleated polymers are placed randomly in the simulation space corresponding to the compartment location of their reactant monomers.

- Polymers can also be severed implicitly with the following form:

$$P_0 \rightarrow P_1 + P_2, \tag{A.5}$$

where $P_1$ and $P_2$ denote the polymers resulting from a split of polymer $P_0$. This reaction keeps in tact the chemical composition of the original polymer.

- In the case of actin filaments, monomers can undergo an aging reaction corresponding to the steps of F-actin ATP hydrolysis. This reaction takes the form:

$$X_{1,f} \rightarrow X_{2,f}, \tag{A.6}$$

where $X_{1,f}$ and $X_{2,f}$ represent two distinct chemical species in the filament.

### A.1.2 Mechanical effects of various chemical reactions.

Most chemical reactions have distinct mechanical effects on the network. We outline the chemical reactions and their mechanical effect below:

- Polymerization and depolymerization can occur at either end of a polymer. When a polymerization event occurs, the equilibrium length $l_0$ will increase by a monomer size, denoted by $l_{mon}$. When $l_0$ has reached its maximum size, which we will denote by $l_{cyl}$, this cylinder stops growing and a new cylinder with $l_0 = l_{mon}$ is created. Similarly, when a depolymerization event occurs, $l_0$ will decrease by $l_{mon}$, and when $l_0 = l_{mon}$, the cylinder will be removed.

- Motor and cross-linker binding can occur on neighboring polymers. When a binding reaction occurs, the respective interaction is created between the two binding cylinders as outlined in the Mechanical Model. The positions $\alpha$ and $\beta$ are determined stochastically at binding. When unbinding, the interaction is removed from the two cylinders.

- Motor walking can occur on a polymer. When a walking reaction occurs, the positional parameter $\alpha$ (or $\beta$, depending on which side of the motor is walking) will increase by some discrete value. The motor may change cylinders due to a walking reaction, which would effectively reset the positional parameter and move the motor onto the next cylinder int the polymer chain. This movement will in turn generate a stress in the motor, and will eventually be equilibrated.

- Branching nucleation can occur on a polymer. When a branching nucleation reaction occurs, a new cylinder with $l_0 = l_{mon}$ is created at a branching site on the mother cylinder, which is determined stochastically. The respective interaction is created between the two cylinders as outlined in the Mechanical Model. This branched cylinder can now polymerize or depolymerize normally at its leading end. When branch unbinding occurs, this interaction is removed between the two cylinders, effectively freeing the daughter polymer.

### A.1.3 Mechanical minimization details.

Mechanical equilibration is performed with any choice of force fields (which are outlined in the Mechanical Model) after a number of chemical reaction steps.

Mechanical equilibration is performed using a conjugate gradient energy minimization algorithm. The system can be minimized to any force minimization tolerance $g_{tol}$. Depending on the size and nature of the active network being simulated, $g_{tol}$ as well as the timestep per mechanical equilibration, denoted as $t_{min}$, can be chosen accordingly. For examples of choosing these parameters for a simulated active network see the later section, which describes choosing a reasonable $g_{tol}$ and $t_{min}$ for the example actomyosin systems presented in the paper.

### A.1.4 Software implementation

The MEDYAN model has been implemented in a serial C++ code which uses efficient data structures and object-oriented programming paradigms to simulate active networks with the scheme described in earlier sections. Fig A.1 shows the implemented software's general workflow. Upon reading user input regarding chemical species and reactions, mechanical interactions, and mechanochemical feedback relationships of constituent elements defined in the system, as well as various simulation parameters and algorithm specifications for these interactions in a number of system input files, the simulation system is constructed with all necessary data structures needed for the updating and management of key simulation components. By allowing a flexible creation of simulation elements, interactions, and algorithms, this software implementation of the MEDYAN model is able to perform simulations for a range of active matter systems with customizable components under various user-defined conditions. Additionally, this software has been constructed in highly

compartmentalized fashion such that modifications and additions to the individual mechanical and chemical components, including interactions as well as algorithms, can be easily implemented.

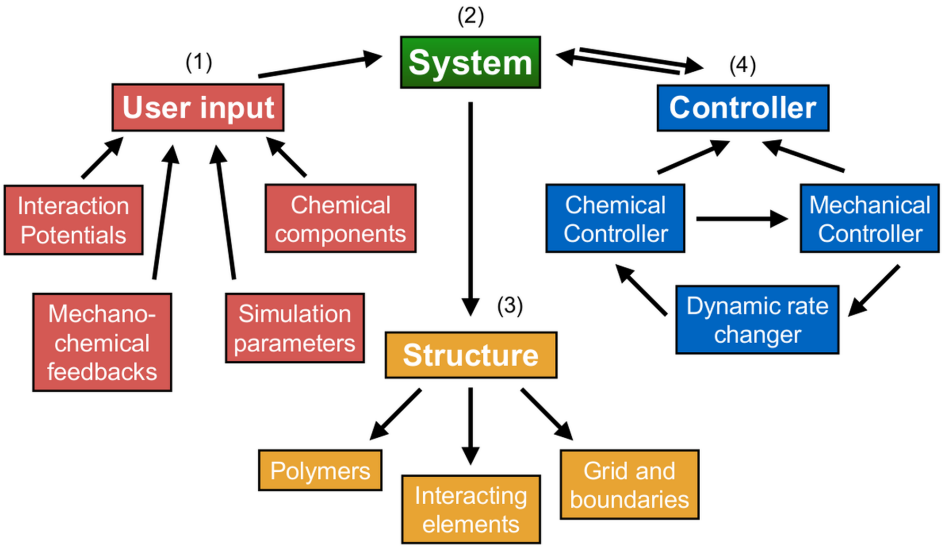


Figure A.1: *MEDYAN* simulations perform the following protocol: (1) User input is given to create the (2) simulation system, which involves (3) setting up the necessary structures (4) and initializing the system controllers. During a simulation, (2-4) constantly communicate via an efficient callback system. We note that many less essential elements of the simulation workflow are omitted from this diagram.

After the system is initialized with the above components, the system controller object, which acts as the simulation driver, is responsible for evolving the system in time via chemical and mechanical interaction controllers. These child controllers, which also are initialized using user-defined parameters and are responsible for executing the specified simulation algorithms for stochastic reaction-diffusion and mechanical equilibration, then iteratively evolve the simulation system in time.

The time evolution and subsequent deformations and growth of the simulated network, including the addition or deletion of components and other interactions that may affect the structure of the network, are then updated in the system by the main controller using an efficient callback system. In this way, chemical reactions, as well as mechanical interactions and deformations, can efficiently update system elements only when needed.

This software package, including source code for the serial C++ MEDYAN implementation, documentation on usage and compilation, and a trajectory visualization tool, is publicly available for general scientific use (www.medyan.org). It is encouraged that users create new patches to the existing code, tailoring it for many scientific purposes. In future work, this implementation will be made to run on parallel architectures, using some of the many available C++ parallelization tools, including the OpenMP and MPI libraries.

## A.2 Parameters used in actomyosin simulations

Below are all parameter values used in the MEDYAN work. In later chapters, all parameters used in simulation of actomyosin networks are the same unless otherwise noted.

| **Reaction** | **Symbol** | **Value [for simulation]*** | **Reference** |
|---|---|---|---|
| Actin diffusion | $k_{actin,diff}$ | 20 $\mu m^2 \cdot s^{-1}$ [80 $s^{-1}$] **a** | - |
| $\alpha$-actinin diffusion | $k_{\alpha,diff}$ | $k_{actin,diff}/10$ $s^{-1}$ **a** | - |
| NMIIA mini-filament diffusion | $k_{NMIIA,diff}$ | $k_{actin,diff}/100$ $s^{-1}$ **a** | - |
| Actin polymerization at plus end | $k_{actin,poly,+}$ | 11.6 $\mu M^{-1}s^{-1}$ [0.151 $s^{-1}$] **b** | [57] |
| Actin polymerization at minus end | $k_{actin,poly,-}$ | 1.3 $\mu M^{-1}s^{-1}$ [0.017 $s^{-1}$] **b** | [57] |
| Actin depolymerization at plus end | $k_{actin,depoly,+}$ | 1.4 $s^{-1}$ | [57] |
| Actin depolymerization at minus end | $k_{actin,depoly,-}$ | 0.8 $s^{-1}$ | [57] |
| NMIIA head binding | $k_{NMIIA,bind}$ | 0.2 $s^{-1}$ | [96] |
| NMIIA head unbinding (zero load) | $k^0_{NMIIA,unbind}$ | 1.7 $s^{-1}$ **c** | - |
| $\alpha$-actinin binding | $k_{\alpha,bind}$ | 0.7 $\mu M^{-1}s^{-1}$ [0.009 $s^{-1}$] | [199] |
| $\alpha$-actinin unbinding (zero load) | $k^0_{\alpha,unbind}$ | 0.3 $s^{-1}$ | [199] |

Table A.1: Reaction parameters used in simulation. *- The value in brackets is the constant used in simulation, calculated based on a compartment volume of (500 $nm$)$^3$. **a**- See the Kuramoto calculation section for more details. **b**- All polymerization rates specified are assumed to be under no external load. **c**- This rate was calculated based on $k_{NMIIA,bind}$, determined by Kovacs et al. [96], as well as the known duty ratio of NMIIA that was also confirmed in the same work.

| Parameter | Symbol | Value | Reference |
|---|---|---|---|
| Length of actin filament segment | $l_{cyl}$ | 27 $nm$, 108 $nm$ **a** | [138] |
| Actin filament bending energy | $\varepsilon_{actin,bend}$ | 2690 $pN \cdot nm$, 672 $pN \cdot nm$ **b** | [138] |
| Actin filament stretching constant | $K_{actin,str}$ | 100 $pN/nm$ **c** | - |
| Actin filament volume constant | $K_{actin,vol}$ | $10^5$ $pN/nm^4$ **d** | - |
| NMIIA head stretching constant | $K_{NMIIA,stretching}$ | 2.5 $pN/nm$ **e** | [196] |
| $\alpha$-actinin stretching constant | $K_{\alpha,stretching}$ | 8 $pN/nm$ | [42] |
| Boundary repulsion energy | $\varepsilon_{boundary}$ | $k_bT$, 4.1 $pN \cdot nm$ | [78] |
| Boundary repulsion screen length | $\lambda_{boundary}$ | 2.7 $nm$ | [78] |

Table A.2: Mechanical parameters used in simulations. **a**- The two values shown are for the different $l_{cyl}$ lengths used in the smaller and larger system simulations; a more aggressive coarse-graining scheme was used in the latter. **b**- Calculated based on the persistence length of actin filaments, which was determined by Ott et al. [138]. The bending energy for a cylinder with $l_{cyl}$ ($= 27$ or $108$ $nm$) in our system was calculated as $\varepsilon_{actin,bending} = l_p \cdot k_bT/l_{cyl}$ where $l_p$ is the persistence length of an actin filament. The two values shown are for the $l_{cyl}$ lengths used in the smaller and larger system simulations. **c**- This value was chosen to be smaller than the known stretching rigidity of actin filaments, experimentally determined by Kojima et al. [91]. This allowed for higher computational efficiency in this study. [85,181] also make similar assumptions, and have shown that this affects actomyosin dynamics very little in both models. While this constant is low, in comparison to other mechanical constants in the system it is still sufficiently high such that cylinder linear deformations are extremely small in simulation (the fraction of cylinders that are linearly stretched or compressed beyond 10% of their equilibrium length after mechanical minimization is zero in all simulated cases). **d**- Chosen to mimic rigid body repulsion, keeping in mind that the diameter of an actin filament is about 6 $nm$ [173]. **e** -This value will be multiplied by the number of heads in the NMIIA ensemble to obtain a mini-filament stretching constant.

| Parameter | Symbol | Value | Reference |
|---|---|---|---|
| Duty ratio of NMIIA head | $\rho$ | 0.1 | [96] |
| Unbinding force of NMIIA head | $F_{NMIIA,unbind}$ | 12.6 $pN$ | [49] |
| Stall force of NMIIA head | $F_{stall}$ | 15 $pN$ **a** | - |
| NMIIA binding kinetics parameter | $\alpha$ | 1.0 **b** | - |
| NMIIA unbinding kinetics parameter | $\beta$ | 0.2 **b** | - |
| NMIIA bound heads parameter | $\gamma$ | 0.05/$pN$ **b** | - |
| NMIIA stall force dependence parameter | $\zeta$ | 0.1 **b** | - |
| Characteristic unbinding force of $\alpha$-actinin | $F_{\alpha,unbind}$ | 17.2 $pN$ | [52] |
| Characteristic polymerization force | $F_{actin,poly}$ | 1.5 $pN$ | [54] |

Table A.3: Mechanochemical parameters used in simulation. **a**- Calculated as $K_{NMIIA,stretching} \cdot d_{NMIIA,step}$. **b**- Chosen to produce realistic attachment and walking times for NMIIA ensembles under zero load, as well as stall loads. We will later discuss details on choosing reasonable parameters for NMIIA mini-filaments.

| Parameter | Symbol | Value |
|---|---|---|
| Number of compartments in each dimension | $N$ | 2 |
| Compartment length | $l_{comp}$ | 500 $nm$ **a** |
| Gradient minimization tolerance | $g_{tol}$ | 1 $pN$ **b** |
| Timestep between mechanical equilibrations | $t_{min}$ | 0.1 $s$ |

Table A.4: Other MEDYAN-specific simulation parameters. **a**- Choosing this compartment length is dependent on the Kuramoto length of the actomyosin systems. **b**- See section regarding choosing conjugate gradient minimization tolerances.

## A.3 Determining key simulation parameters for the actomyosin systems.

### A.3.1 Calculation of the Kuramoto length and diffusion rate.

The calculation of the Kuramoto length for the system of interest is as follows: assuming a diffusion constant $D$ of 20 $\mu m^2 s^{-1}$ for G-actin as in previous work [77],

the Kuramoto length $l_k$ of the system is defined as

$$l_k = \sqrt{6D\tau}, \tag{A.7}$$

where $\tau$is the timescale of the fastest chemical reaction in the system. For this system, actin polymerization is the fastest reaction (see Table 1A in S1 Table for reaction rates used in the actomyosin systems), and with an initial concentration of $[A] = 20\ \mu M$, the timescale of this reaction is

$$\tau = \frac{1}{k_{actin,poly,+}[A]} = 0.003s, \tag{A.8}$$

giving a Kuramoto length of 0.64 $\mu m$. We will choose the compartment length to be 0.5 $\mu m$. It is noted that this is a highly conservative choice of compartment size, since eventually in simulation the actin concentration stabilizes around 0.2 $\mu M$. The rate of the diffusion reactions between compartments using this 0.5 $\mu m$ length, with the diffusion rate as before, is 80 $s^{-1}$.

Unfortunately, there exists little data on the diffusion constants of $\alpha$-actinin and NMIIA mini-filaments, especially in our reconstituted *in vitro* system. To calculate a diffusion rate between compartments for the these molecules, we will assume both of these molecules have a diffusion constant $D$ that is a factor of 10 and 100 less than the diffusion constant of actin, respectively, due to their size and shape. Using the chosen compartment length, this will give a diffusion rate between compartments of 8 $s^{-1}$ and 0.8 $s^{-1}$, respectively, for those molecules. It is noted that actin filaments of any length do not diffuse in our simulation.

### A.3.2 Choosing the gradient minimization tolerance.

In order to determine an appropriate gradient tolerance $g_{tol}$ for mechanical equilibration, we have performed benchmarks to describe the performance and displacement error in polymer deformations under various $g_{tolerance}$. Based on these results, we chose a $g_{tolerance} = 1\ pN$, which produces sufficiently small displacement errors on the order of nanometers, which already is way beyond the desired resolution of this model.

### A.3.3 Choosing the timestep between mechanical equilibration.

In order to determine an appropriate timestep between mechanical equilibrations, denoted as $t_{minimization}$, we can take into account the frequency of walking events of NMIIA mini-filaments along actin filaments, which will define a reasonable timestep between motor walking events, and thus the time allowed between mechanical minimizations in simulation, since this is the only molecule in the system producing large forces, and thus significant deformations in the network.

The zero-force walking rate between cylinders of an average-sized NMIIA mini-filament in our mechanochemical model is about 0.4 $s^{-1}$. With the given concentrations simulated, which correspond to between 2-8 NMIIA mini-filaments in the smaller actomyosin systems, it is reasonable to choose a $t_{minimization}$ of 0.1 $s$, which will correspond to 0.1-0.3 walking events per minimization, respectively. For the larger actomyosin systems, we will use the same timestep, as motor walking events will be distributed throughout the simulation volume and the chances of direct inter-

actions of walking events between motors within $t_{minimization}$ is extremely unlikely.

## A.4 Mechanochemical models used in the actomyosin systems.

It is noted before beginning this section that all values of reaction rates and mechanochemical parameters used in the mechanochemical models outlined below can be found in S1 Table.

### A.4.1 Non-muscle myosin IIA.

Myosin II, in muscle and non-muscle isoforms, has been shown by many to have distinct mechanochemical properties that allow the molecule to respond to stresses in the cytoskeleton [95, 113, 134, 142]. We outline a simple model proposed for myosin II mini-filament binding, unbinding, and walking in the case of non-muscle myosin IIA (NMIIA). Much of this work is an extension of the results for the Parallel Cluster Model of small, non-processive myosin motor ensembles introduced by Erdmann et al. [49], and is adopted to fit our coarse-grained description. We assume the following regarding mechanics for our implicit model of NMIIA mini-filaments:

- NMIIA mini-filaments are comprised of 10-30 implicit subunits [182], and the number of subunits is randomly chosen when a binding event occurs. Mechanical constants are recalculated accordingly based on the number of subunits selected. We will denote the number of subunits as $N_{total}$, since this value also represents the number of head groups (or heads) on each side of the bipolar

filament.

- The forces that will occur in this network are not large enough for the NMIIA ensemble to exhibit slip bond behavior, so that the mechanochemical effect of increased pulling force will be a catch bond. The form of this relationship will be outlined below.

- The stiffness of a single NMIIA head has been determined experimentally by Vilfan et al. [196]. The stiffness of the entire mini-filament is then calculated based on the number of subunits.

We also assume the following regarding the single NMIIA cross-bridge cycle and associated chemistry:

- We assume a simplified cross-bridge cycle, as in work by Stam et al. [175] that has two states, bound and unbound:

$$\text{Bound state: } AM \cdot ADP$$

$$\text{Unbound state: } M \cdot ADP \cdot Pi$$

- The duty ratio $\rho$ of NMIIA is low, and this duty ratio defines the mechanochemical effects of force on unbinding and walking, as will be elaborated on in the later section. We use the duty ratio and reaction rate values found by Kovacs et al. [96].

- The bound state of NMIIA is the only state that is mechanochemically affected. Isoforms of myosin II show a decreased dissociation rate of ADP when

bound to actin with increased pulling force in the lower force regime [68]. The chosen form of this mechanochemical effect will be show below.

The binding rate of a NMIIA mini-filament to a pair of actin filaments can be defined as

$$k_{fil,bind} = \alpha \cdot k_{NMIIA,bind} \cdot N_{total} \tag{A.9}$$

since there are $N_{total}$ NMIIA heads in the mini-filament that can bind to F-actin, and $k_{NMIIA,bind}$ is the binding rate of a single NMIIA head to an actin filament. $\alpha$ is a parameter that can be chosen to mimic NMIIA mini-filament binding kinetics; this will be elaborated on below.

Due to the molecule's catch bond behavior, the unbinding rate of a NMIIA mini-filament from a pair of actin filaments can be written as

$$k_{fil,unbind} = \frac{\beta \cdot k^0_{NMIIA,unbind}}{N_{bound}} \cdot \exp\left(\frac{-F_{ext}}{N_{bound} \cdot F_{NMIIA,unbind}}\right), \tag{A.10}$$

where $F_{ext}$ is the total stretching force of the NMIIA mini-filament and $F_{NMIIA,unbind}$ is the characteristic unbinding force, determined by thermal energy and the NMIIA head unbinding distance. This relationship has been shown by [49]. $\beta$ is another parameter chosen for NMIIA mini-filament unbinding kinetics.

In our model, $N_{bound}$, the number of currently bound NMIIA heads to actin filaments, is implicit. The number of bound heads can be approximated to increase linearly with force in the regime we are considering [49, 142]. So, we can express $N_{bound}$ as

$$N_{bound} = \rho \cdot N_{total} + \gamma \cdot F_{ext}, \tag{A.11}$$

where $\rho$ is the duty ratio under no load, and $\gamma$, similarly to $\alpha$ and $\beta$, is a parameter chosen to fit NMIIA mini-filament unbinding kinetics.

As shown by Hill et al. [71] generally for motor ensembles, and nicely rearranged by [49], the walking rate of a NMIIA mini-filament under a constant external load can be written as

$$k_{ens,walk} = k^0_{ens,walk} \cdot \frac{F_{stall} - \frac{F_{ext}}{N_{total}}}{F_{stall} + \frac{F_{ext}}{N_{total}\zeta}}, \tag{A.12}$$

where $F_{stall}$ is the stall force of a NMIIA head, and and $F_{ext}$ is the pulling force on the NMIIA mini-filament in the direction opposite of walking movement, and $\zeta$ is chosen to match NMIIA mini-filament walking kinetics. Erdmann et al. showed that this parameter, as well as the stall force $F_{stall}$ does not change for mini-filaments in the subunit range that we are considering [49].

In terms of our implicit model, $k^0_{ens,walk}$, which is the walking rate under no load, can be approximated, as by Erdmann et al., by using the number of unbound heads in the NMIIA ensemble, as well as the binding rate of a single NMIIA head [49]. So, we can express $k^0_{ens,walk}$ as

$$k^0_{ens,walk} = \frac{N_{total} - N^0_{bound}}{N^0_{bound}} \cdot k_{NMIIA,bind}, \tag{A.13}$$

where $N^0_{bound}$ is the number of bound NMIIA heads under no load, which is simply $\rho N_{total}$. It is noted that in our model, the walking rate must also be multiplied by a fraction of relative step size of a single motor head to the step size of the entire mini-filament in simulation, which is based on the number of binding sites per cylinder.

In choosing the mechanochemical parameters $\alpha$, $\beta$, $\gamma$, and $\zeta$ to be 1.0, 0.2, $0.05/pN$, and 0.1, respectively, the mechanochemical model outlined above gives an unloaded attachment time of 5 $s$ and an unloaded walking rate of 11 $nm/s$. Under stall conditions (i.e. $F_{ext} = \rho K_{NMIIA,stretching} d_{step}$), the model gives a loaded attachment time of 50 $s$ and a loaded walking velocity of 3 $nm/s$.

### A.4.2 $\alpha$-actinin.

$\alpha$-actinin is a cross-linking protein typically found in the cytoskeleton that has distinct mechanical and chemical properties. We outline a simple model for repre-

senting the mechanochemistry of this cross-linker, including binding and unbinding.

We assume the following regarding mechanics for our model of $\alpha$-actinin cross linkers:

- The stiffness of $\alpha$-actinin has been experimentally determined by Ferrer et al. [52].
- We ignore any unfolding domains and assume a constant length. Although there are known unfolding domains that may change network elasticity [42], these will not be included in our model. Forces in our network also will not be large enough to cause these unfolding events.

We also assume the following regarding $\alpha$-actinin binding and unbinding chemistry:

- Binding occurs at a constant rate unaffected by force, and has been experimentally determined by Wachsstock et al. [199].
- Unbinding is mechanochemically affected, and we will assume that it is a simple slip bond. The form of this mechanochemical effect will be shown below.

The rate of unbinding will be affected by the pulling force on the cross-linker, and can be expressed as

$$k_{\alpha,unbind} = k^0_{\alpha,unbind} \cdot \exp\left(F_{ext}/F_{\alpha,unbind}\right), \tag{A.14}$$

where $k^0_{\alpha,unbind}$ is the $\alpha$-actinin unbinding rate under no external load, $F_{ext}$ is the pulling force on the molecule, and $F_{\alpha,unbind}$ is the characteristic unbinding force of $\alpha$-actinin, determined by thermal energy and the $\alpha$-actinin unbinding distance.

### A.4.3 Actin filaments.

Actin filaments are dynamic species which can polymerize and depolymerize from either end. We outline the mechanochemical effect of filaments polymerizing under an external load, provided by a boundary. We assume the following regarding the mechanics of actin filaments:

- The stiffness and flexural rigidity has determined by experiments [91, 138].
- Both ends of the filament can experience an external load force from a boundary.

The polymerization rate of a filament tip under external load can be modeled by the Brownian Ratchet [141] with the following form:

$$k_{poly} = k^0_{poly} \cdot \exp\left(-F_{ext}/F_{actin,poly}\right), \tag{A.15}$$

where $k^0_{poly}$ is the polymerization rate under no external load, $F_{ext}$ is the external load force on the actin filament, and $F_{actin,poly}$ is the characteristic polymerization force of an actin filament, determined by thermal energy and the size of an actin monomer.

## A.5 Benchmarking and validation of MEDYAN.

It is noted that all benchmarking simulations were performed on Intel Xeon Ivy Bridge E5-4640v2 processors running at 2.20 GHz, with 25.6GB DDR3 memory at 1333 MHz, as provided by the Deepthought2 supercomputing cluster at the University of Maryland.

### A.5.1 Benchmarking and validation of the NRM algorithm in cytoskeletal stochastic reaction-diffusion.

We present a brief benchmarking and validation test of the optimized *Next Reaction Method* (NRM) algorithm [63] for stochastic reaction-diffusion that is used in MEDYAN, which provides huge optimizations for sparse chemical reaction networks (i.e. loosely coupled chemical reactions across the simulation domain). The original Gillespie algorithm, which is usually known as the Gillespie *direct method* (DM), which is used in previous works to describe the reaction-diffusion processes of lamellipodia [77,78] as well as filopodia [100,210–212] has been validated thoroughly in the papers mentioned, and as MEDYAN is built based on this original algorithm, we will not validate the correctness of this approach here.

To validate the correctness, as well as benchmark performance increases, of the NRM algorithm compared to the original Gillespie DM, we ran a set of simulations for a smaller $1 \times 1 \times 1$ $\mu m^3$ actin network with the same parameters as described in the Results section of the paper with both reaction-diffusion algorithms for 10 $s$ of

simulation time. These benchmarking systems had identical configurations to the systems in the Results section (20 $\mu M$ of diffusing actin and 50 filaments), but do not contain $\alpha$-actinin or non-muscle myosin IIA mini-filaments. Unless otherwise noted besides the previously mentioned changes, all parameters used in these test cases are identical in setup to the Results section, including compartment size and reaction constants. 4 trajectories were run for each configuration.

To validate the NRM algorithm, we compare the (i) the mean filament length over time for 10 $s$ of network evolution, and (ii) the critical concentration over time for 10 $s$ of network evolution, averaged over the 4 trajectories, using the NRM and original Gillespie DM method, as shown in Figs A.2 and A.3. We see excellent agreement between these algorithms, as well as reasonable critical concentration value $[A_c]$ reached for both algorithms, which can be solved analytically by using the polymerization and depolymerization rates of actin filaments in the simulation:

$$[A_c] = \frac{k_{actin,depoly,+} + k_{actin,depoly,-}}{k_{actin,poly,+} + k_{actin,poly,-}} = 0.17\mu M. \tag{A.16}$$

We anticipate our critical concentration value in simulation to be higher than this analytical value, as the mechanochemical effects included in this simulation (Brownian ratchet model of polymerizing filaments) disallow polymerizing filaments near a boundary to grow rapidly. We do, in fact, see a critical concentration reached in both algorithms of about 0.4 $\mu M$.

To measure performance, we can look at the computation time for the chemical stochastic reaction-diffusion elapsed over the 10 $s$ of simulation time, using both

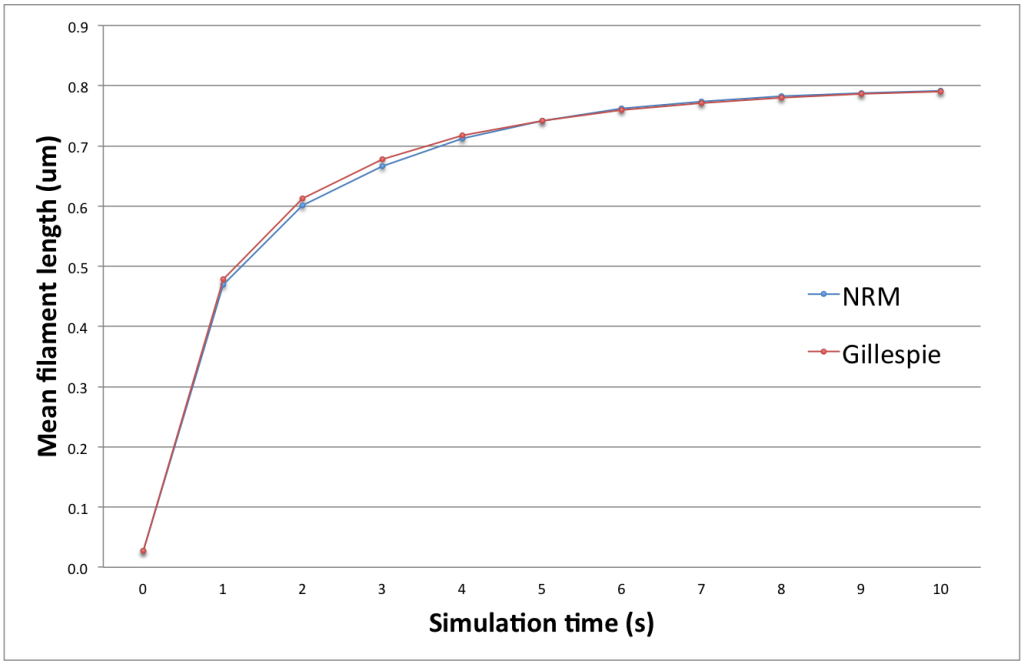


Figure A.2: Mean filament length over the 10 **s** of network evolution, using the NRM and Gillespie DM. The algorithms are in excellent agreement.

chemical algorithms, as shown in Fig A.4. It is noted that this measurement ignores any mechanical equilibration steps, which would add additional time to the overall simulation. We see that the NRM algorithm outperforms the Gillespie DM by over 100-fold for this actin network. Larger $3 \times 3 \times 3$ $\mu m^3$ actin networks were not benchmarked, as the Gillespie DM does not achieve 1 $s$ of simulation time within 12 hours of computation time.

### A.5.2 Benchmarking and validation of the coarse-grained polymer scheme in cytoskeletal systems.

We present a brief benchmarking and validation of the coarse-grained polymer scheme based on cylindrical monomer segments used in MEDYAN to simulate cy-

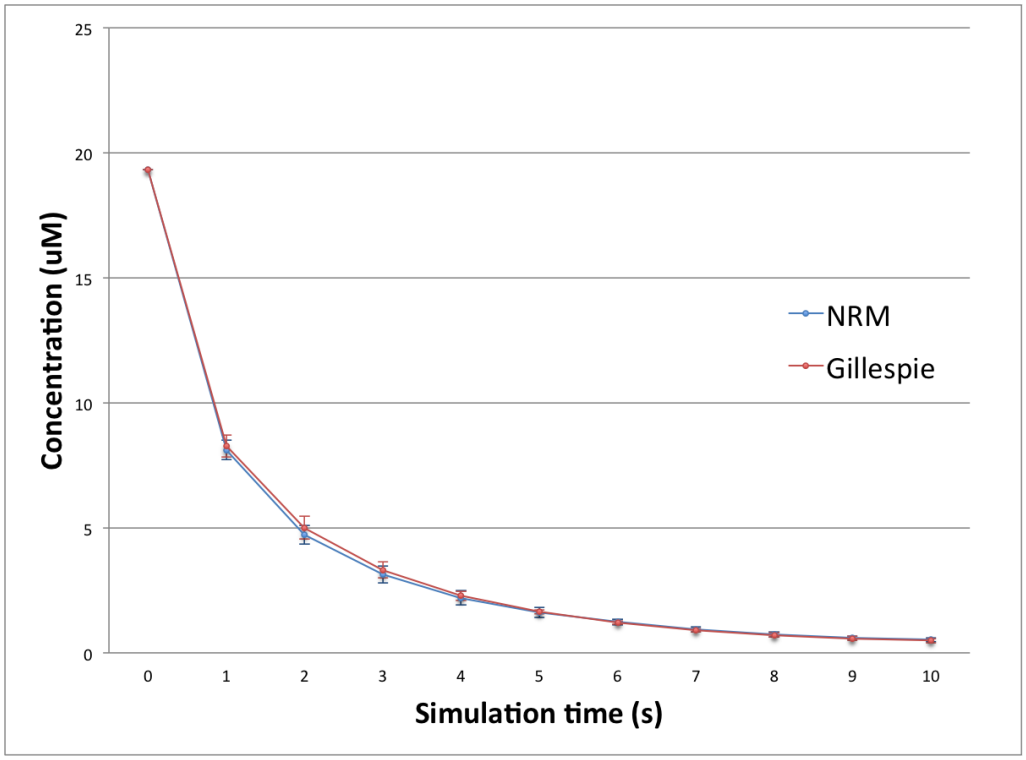


Figure A.3: Concentration of diffusing actin over the 10 **s** of network evolution for the actin system using the NRM and Gillespie DM. The algorithms are in excellent agreement.

toskeletal filaments. The bead-spring model of semi-flexible polymers to represent individual monomeric components has been used by many computational works and has been proven as a correct description of polymer chain mechanics, so we will benchmark our coarse-grained cylindrical scheme by comparing directly to the bead-spring monomeric model with gradient tolerance $g_{tol} = 1\ pN$, which is, in our model, the limit of cylinder segment length approaching a single monomer size.

To validate and test performance of various levels of cylindrical coarse-graining compared to a simple bead-spring monomer model, we equilibrated a single filament

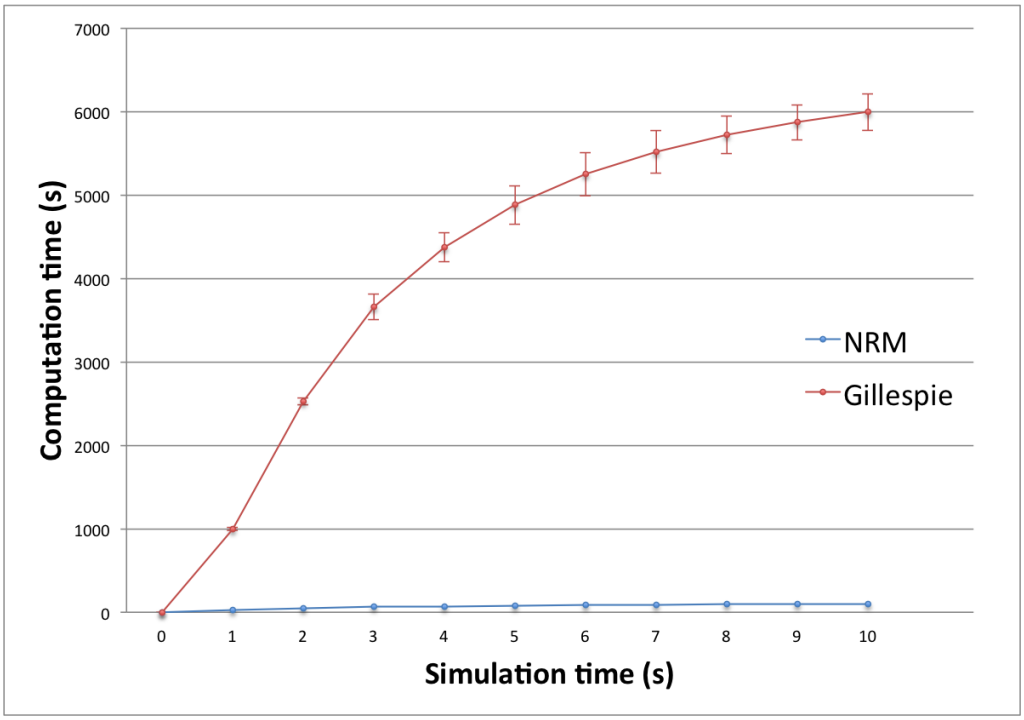


Figure A.4: Benchmarking speed of the two stochastic simulations algorithms implemented. There is a performance increase of over 100-fold for this actin system when using the NRM algorithm compared to Gillespie methods.

with length $L = 1\ \mu m$ with fixed endpoints undergoing a point force of 50 $pN$ at its center under varying equilibration parameter values and coarse-graining levels. Unless otherwise noted as changed, mechanical parameters for these filaments were taken as in the actin filament description in the Results section. It is, however, noted that the bending energy used between cylindrical segments scales inversely with the length of the cylindrical segments used, providing an accurate overall persistence length of the filament.

Figs A.5 and A.6 shows the various validation and benchmarking results. In Fig A.5, the displacement error of the filament after mechanical equilibration $e_d$

is shown for various coarse-grained cylindrical segment lengths $l_{cyl}$ and gradient minimization tolerances $g_{tol}$, which we define as:

$$e_d = \frac{|x_{bs} - x_{cg}|}{L} \tag{A.17}$$

where $x_{bs}$ represents the center point of the filament ($L/2$ along the length of the filament) after equilibration in the bead-spring model, and $x_{cg}$ is the same center point after equilibration with a coarse-grained cylindrical description.

We then performed a similar validation and benchmarking for a microtubule-like filament as also shown in Figs A.5 and A.6, which has an estimated persistence length of 5 $mm$ and an estimated monomer size of 2 $nm$. These parameters defined the bending energy used in the harmonic bending potential for the microtuble, which is increased in comparison to the bending energy of an actin filament cylindrical segment by a factor of over 1000. This benchmarking shows that a polymer with high stiffnesses can be simulated efficiently and accurately with this approach. As in the actin filament example, the bending energy used scales inversely with the length of the chosen cylindrical segment.

### A.5.3 A note on computational performance for simulations in Results section, and time comparisons to previous models.

Computation time used for simulations in the Results section was varying depending on the size and concentrations used in the various actomyosin networks. For a moderate-concentration actomyosin system in 1 $\mu m^3$ of simulation volume,

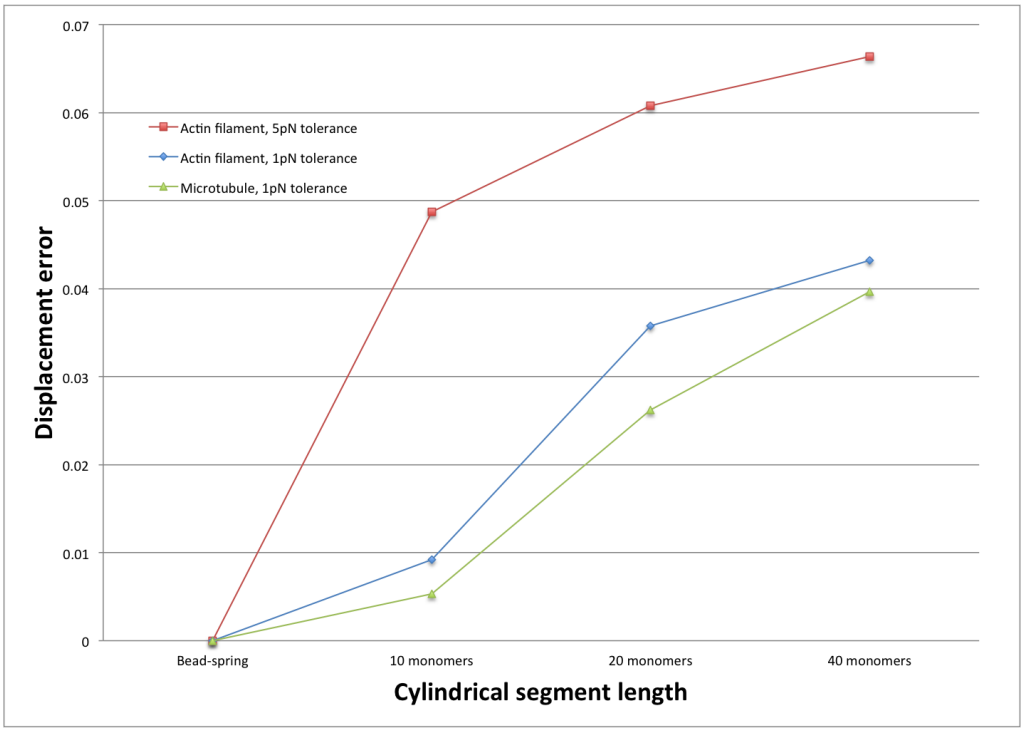


Figure A.5: Measured polymer displacement error for a typical conjugate gradient minimized energy function. Since this error compares to a bead-spring description, there is no error shown for the bead-spring model. Displacement errors stay under 5% of the total polymer length for all levels of coarse-graining used.

2000 $s$ of simulation time was reached in about 12 hours. For increasing concentrations in this smaller domain, computation time was increased up to 2 days. The larger actomyosin systems, which contain 27 $\mu m^3$ of simulation volume, ran to 500 $s$ of simulation time in about 6 days. It is noted that these performances measured are serial computations, as a parallel MEDYAN implementation has not yet been created.

In estimating performance increases of MEDYAN from previous versions of the model, the code of [78] was typically benchmarked to run 1 $s$ of simulation with

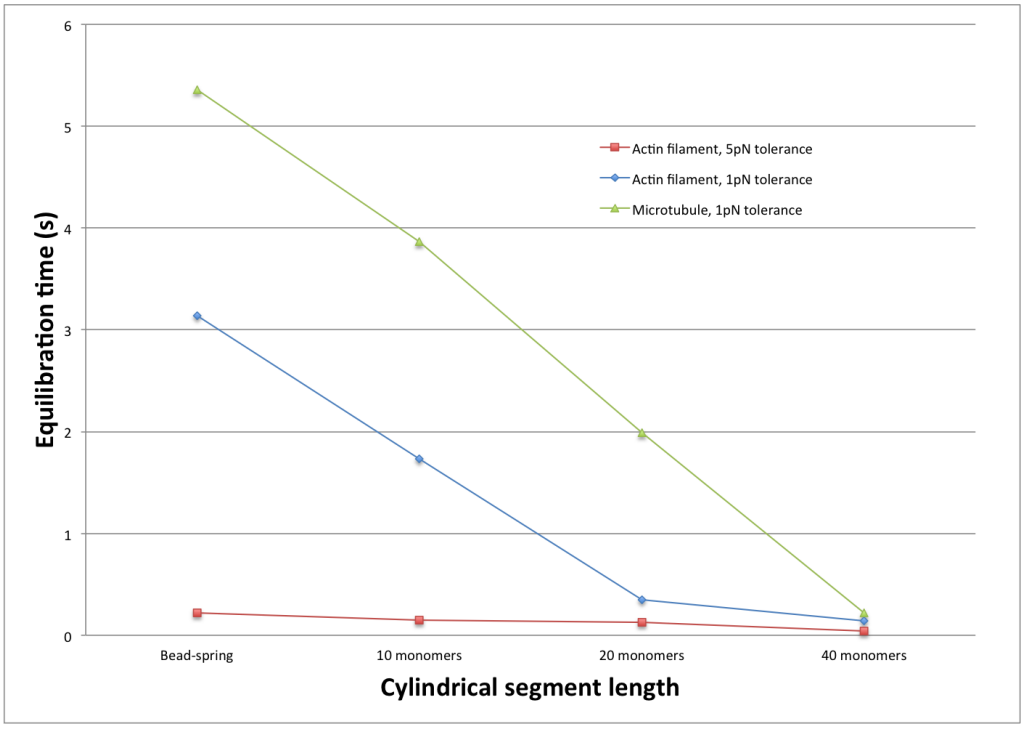


Figure A.6: The speed of equilibration time for conjugate gradient energy minimization of a filament. Equilibration speed ups are more apparent for the lower tolerance levels. Microtubules show similar equilibration times compared to actin filaments, and could probably benefit from even more coarse-graining.

reasonable concentrations of actin in a few micron sized domain in about 6 hours of computation time.

# Appendix B: Supporting information for Chapter 3

## B.1 Parameter considerations for the simulated proteins

The parameters chosen for our simulations are given in Table B.1, which includes experimentally measured mechanical stiffnesses as well as chemical kinetics of (un)binding for the proteins considered. Considering cross-linkers *in vivo*, the abundant cross-linker $\alpha$-actinin displays a bound lifetime of $2.5s$ and $\Delta G$ of $2-4$ $k_bT$ as addressed in recent reviews [127, 179]. Other abundant cytosolic cross-linker filamin has a lifetime of $\approx 1s$ and similar free energy of binding. Other cross-linkers not found in contractile actomyosin, such as fascin, have a much stronger binding of $\Delta G = 15$ $k_bT$. So, we choose to vary a binding energy control variable $\epsilon$ from 0 to 15 $k_bT$. We also use kinetic (un)binding rates for cross-linkers in the aforementioned physiological range while also testing slower kinetics: $k_u^{cl}$ is varied from $0.01/s$ to $10/s$.

Although the aim in this study is not to probe the effects of mechanochemical feedback between these proteins, we find it necessary to include key mechanochemical relationships for full model realism. For individual cross-linker bound to the filament pair, we employ a typical "slip" bond characterized by a decreasing bound lifetime with applied load [52] as $k_{u,eff}^{cl} = k_u^{cl} e^{F_{cl} x_{cl}/n_p k_b T}$ where $x_{cl}$ is a characteris-

tic unbinding distance, and $k_u^{cl}$ is the zero-force unbinding rate. We only consider pulling forces such that $F > 0$.

| Parameter | Description | Value |
|---|---|---|
| $k_bT$ | Thermal energy | 4.1 $pNnm$ |
| $x^0_{l,r}$ | Initial left ($l$) and right ($r$) actin filament midpoints | 1 $\mu m$, 3 $\mu m$ |
| $L$ | Length of actin filament | 2 $\mu m$ |
| $K_t$ | Boundary tether stiffness | $0.001 - 1$ $pN/nm$ |
| $\eta$ | Viscous damping constant | $10^{-3}$ $pNs/nm$ |
| $F_s$ | Stochastic force experienced by actin filaments | - |
| $l_o$ | Actin filament pairwise overlap | *Observable* |
| $F_t^{l,r}$ | Tether forces experienced by left ($l$) and right ($r$) actin filaments | *Observable* |
| $F_{cl}$ | Force experienced by bound cross-linkers | - |
| $F_m$ | Force experienced by motor filament | - |
| $F_D$ | Total dipole force (sum of left and right tether tensions) | *Observable* |
| $x_{l,r}$ | Instantaneous left ($l$) and right ($r$) actin filament midpoint | - |
| $l_o^m$ | Motor-preferred actin filament overlap | - |
| $l_o^{ss}$ | Steady-state overlap in pFD | - |
| $N_t$ | Number of single motor heads per side of motor filament | 10 **a** |
| $m, n$ | Number of bound motor filaments ($m$) and cross-linkers ($n$) | - |
| $n_p$ | Number of possible cross-link binding sites | - |
| $\epsilon$ | Cross-linker binding energy | $0 - 15$ $k_bT$ |
| $v_m$ | Effective volume of cross-linker in solution | $1 \cdot 10^{-3}$ $\mu m^3$ **b** |
| $v_b$ | Approximate bound volume of cross-linker | $3 \cdot 10^{-6}$ $\mu m^3$ **c** |
| $\Delta$ | Distance between cross-link binding sites | 10 $nm$ |
| $k_{b,u}^{cl,m}$ | (Un)binding rate of cross-linkers ($cl$) and motor ($m$) | For $cl$, $0.01 - 10/s$ |
| $\bar{\tau}_{b,u}^{cl,m}$ | Mean (un)binding time of cross-linkers ($cl$) and motor ($m$) | - |
| $d_s$ | Motor filament step size | 5 $nm$ |
| $k_{b,u}^{ms}$ | Single motor head (un)binding rate | $0.2/s, 1.7/s$ [95] |
| $F_s$ | Motor filament stall force | 24 $pN$ **d** |
| $v_w^0$ | Walking velocity of motor filament | 10 $nm/s$ **e** |
| $\alpha$ | Stall velocity mechanochemical parameter for motor filament | 0.2 [49] |
| $\beta$ | Catch-bond mechanochemical paramter for motor filament | 2 [49] |
| $x_{cl}$ | Characteristic slip-length for cross-linker | 0.5 $nm$ [52] |
| $x_m$ | Characteristic catch-length for single motor head | 1.6 $nm$ [68] |
| $K_{ms}$ | Stiffness of single motor head light chain | 0.5 $pN/nm$ [**?**, 201] |
| $K_m$ | Effective spring constant of motor filament | – |
| $\tau_{lab}$ | Timescale of laboratory measurements | 200$s$ |
| $\epsilon_{lab}$ | Divergence point of steady-state and laboratory measurements | – |
| $\chi$ | Stochastic contraction length of aFD | *Observable* |
| $\xi$ | Stochastic extension length of aFD | *Observable* |
| $\omega_\chi$ | Contraction frequency of aFD | *Observable* |
| $\omega_\xi$ | Extension frequency of aFD | *Observable* |
| $V_{eff}$ | Effective inter-filament velocity of aFD | *Observable* |



Table B.1: Glossary of variables and parameter choices for Chapter 3.

**a** - Geometric constraints of the bipolar motor filament may disallow all tens of heads to be available for binding to a pair of actin filaments due to its double-ended conic structure [20, 135]. Since the number of non-muscle myosin II heads per side of a mini-filament is 30 for isoform A [20], we assume for this study that a third of these heads are available for binding to the 1D actin filament. **b** - Calculated as the inverse of concentration $V/N$, assuming a bulk cross-linker concentration of 1 $\mu M$. **c** - Although the exact volume of a cross-linker binding pocket is unknown, this is an order of magnitude estimate based on the dimensions of $\alpha$-actinin [199], which is valid in the approximate expression of Eq. 3.2. Changes of this value would alter the effective stochastic rate constants of cross-linker (un)binding for a given $\epsilon$. **d** - An approximation using the stall force of a single myosin II head, $F_{ss} \approx 4pN$, multiplied by its duty ratio at stall and the number of motor heads available for binding, $F_s = \rho_s^m(F) N_t F_{ss} = 24\ pN$. **e** - Calculated using the analytic result of Erdmann et al. [49] for the zero-force walking rate based on individual motor head (un)binding rates. This value was also approximately obtained by Stam et al. [175] and is further motivated by the experimental results of Norstrom et al. [135].

We now consider the mechanochemical dynamics of the myosin II motor filament included in our model. These highly transient units, as described in the main text, must be regarded as a coarse-grained version of a more detailed stochastic (un)binding and walking process of many individually transient motor heads in a single bipolar mini-filament. We consider an effective unbinding rate of the coarse-grained overlap potential which mimics the mean unbinding time of a single side of the mini-filament with $N_t = 10$ heads. Since the overall motor filament unbinding rate $k_u^m$ is non-trivial compared to the single cross-linker case because of its non-linear dependence on the single motor head (un)binding rates $k_b^{ms}$ and $k_u^{ms}$ and individual motor head stochasticity, we use an approximate expression for the mean unbinding time of the ensemble of heads derived by Erdmann et al. [49] using a series expansion of an adjoint master equation for motor ensemble states:

$$\bar{\tau}_u^m \approx \frac{1}{k_b^{ms} N_t} \left[ \left( 1 + \frac{k_b^{ms}}{k_u^{ms}} \right)^{N_t} - 1 \right]. \tag{B.1}$$

We note that this form is only accurate under a zero-load assumption, but is reme-

died by combining with an exponential factor as shown below. In an approximation, we inherently assume a single exponentially-distributed process with rate $k_u^m = 1/\bar{\tau}_u^m$. For simplicity, we also consider motor filament binding to the pair of actin filaments as a single stochastic process with rate $k_b^m = k_b^{ms} N_t$, ignoring partially bound states which do not generate tension between the actin filament pair.

Individual myosin II motor heads have been shown to display "catch"-bond behavior, characterized by an increased bound lifetime with applied load [68,95,96]. We aim to describe the (un)binding and walking kinetics of an ensemble of motor heads with a simple set of parameters to capture the essential aspects of motor filament mechanosensitivity - a binding lifetime that increases exponentially with applied load $F$ and the number of motor heads in the filament $N_t$, motivated by the results of [49], and a walking velocity that is one of the celebrated Hill form [71]. Since the exponential dependence of motor head unbinding in the post power-stroke state has been directly observed in the bound lifetime of an entire ensemble of heads [49], we express the unbinding rate of the motor filament as:

$$k_{u,eff}^m = k_u^m e\left(\frac{-F x_m}{N_b(F) k_b T}\right), \tag{B.2}$$

where $x_{cl}$ is a characteristic unbinding distance of a single motor head, and $N_b(F)$ is the number of motor heads per side of the motor filament bound to actin. An essential characteristic of the myosin II motor filament to capture in this function is a near-linear increase in the number of bound heads with external load [43,49,142].

Since this expression is difficult to derive due to the stochastic nature of the motor heads, an approximate expression for $N_b(F)$, motivated by [49], can be written as $N_b(F) = \rho N_t + \beta F$ where the mechanosensitivity parameter $\beta$ has been chosen to mimic the response of a low-duty ratio motor like non-muscle myosin IIA. Upon a motor stepping event, the number of bound heads determines the effective spring constant of the bipolar mini-filament with $N_t$ heads bound per side to an actin filament in parallel, with stiffness $K_{ms}$ corresponding to the myosin II light chain connecting individual heads. The sides of the bipolar filament are mechanically connected by an extremely stiff motor filament heavy chain region, giving an effective spring constant of the ensemble $K_m = K_{ms}N_t/2$.

In the case of motor walking, we can include a force-dependent walking velocity $v_w(F_m)$ similar to a Hill-relation [71] for myosin II:

$$v_w(F) = 2v_w^0 \frac{F_s - F_m}{F_s + F/\alpha} \tag{B.3}$$

where $F_m$ is the instantaneous force on the motor, $\alpha$ is a parameter describing the concave nature of the velocity function which has been chosen to mimic a low-duty ratio motor, and the stall force of the motor filament $F_s$ is described in Table B.1. This equation accounts for two ensembles of heads walking with velocity $v_w^0$ in opposite directions on each actin filament. We note that in general, non-muscle myosin II filaments are highly transient compared to their muscle sarcomere counterpart, but this still has shown to be an effective representation of stall dynamics [49]. This transience is due to a small number of motor molecules $N_t \approx 28$ [20] as compared

to smooth or skeletal muscle filaments where $N_t \approx 500$ [142], causing frequent detachments of the motor head ensemble from the filament pair and tension release, which, in turn, raises serious slippage issues as discussed.

We have chosen in our stochastic representation to model non-muscle myosin II isoform A, which displays a faster head (un)binding dynamics and less mechanosensitivity compared to isoform B, another abundant motor filament in the eukaryotic cytosol [96]. In *in vitro* sliding assays, myosin II head sliding velocities vary significantly, ranging from 50 $nm/s$ to as slow as 10 $nm/s$ under varying ATP concentration for isoform B [20, 135]. Although to our knowledge, no single-molecule kinetic study of isoform A mini-filaments *in vivo* has been performed - we use a prediction from Erdmann et al. [49] to obtain an average isoform A sliding velocity of $v_w^0 = 10nm/s$ based on the isoform and number of binding heads we are considering in the mini-filament:

$$k_w^m = ({\rho_{ms}}^{-1} - 1)k_b^{ms} \tag{B.4}$$

where $\rho_{ms} \approx 0.1$ is the zero-force duty ratio of a single motor head determined experimentally [96].

## B.2 Model validation

We validated all separate components of our simulation. We first began by validating the Langevin dynamics of tethered individual actin filaments. We ran Langevin dynamics for a tethered actin filament initially at $x = 0$ for various tether

stiffnesses $K_t$ and Langevin timestep $\Delta t = 0.1\ ms$ for a total simulation time of 100 $s$. To test the validity of these simulations, we fit the ideal infinite-time Gaussian distribution for tethered Brownian motion [151]:

$$P(x) = \frac{1}{\sqrt{2\pi k_b T / K_t}} e^{\frac{-x}{2\pi k_b T / K_t}}. \tag{B.5}$$

We also validated the equilibrium distribution of $x$ to agree with the equipartition theorem, which ensures $\langle E \rangle = \frac{1}{2} k_b T = \frac{1}{2} K_t \langle x^2 \rangle$, within 5% tolerance. Fig. B.1(a) shows the distributions $P(x)$ for various $K_t$ varying from 0.001 $pN/nm$ to 1.0 $pN/nm$, and all simulations fit the expected ideal distribution in Eq. B.5 well. All average energies also matched the expected equipartition result within the given tolerance.

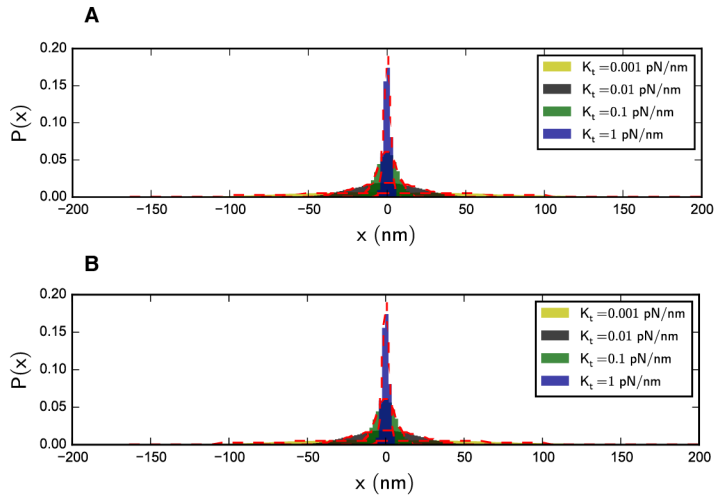


Figure B.1: Validation of Langevin motion of tethered actin filaments. (a) Single-filament case for various $K_t$. All distributions match the expected form in Eq. B.5, with the ideal distribution for each $K_t$ plotted in red dotted lines. (b)Two-filament case. All distributions match the expected form in Eq B.5 with double the variance, with the ideal distribution for each $K_t$ plotted in red dotted lines.

We then, as a brief integration test, validated the dual motion of two tethered

actin filaments starting at $x_l = 0\ \mu m$ and $x_l = 4\ \mu m$. Fig. B.1(b) shows the resulting $l_o$ distributions for varying $K_t$ in the two-filament system. Ideally, the distribution of $l_o$ should have double the variance of the Gaussian distribution in Eq. B.5, which is indeed the case as shown in the previous figure. It is expected that the average energy $\langle E \rangle = \frac{1}{2} K_t \langle l_o^2 \rangle$ should also double for the two-filament system - this is achieved within the tolerance specified in the single-filament case.

To validate motor filament force production between two actin filaments, we start with the same filament configuration as in the no motor case and run Langevin dynamics with motor filament movement for a total simulation time of 100 $s$ for varying $K_t$. We note that motors do not bind and unbind in this benchmark, but stay bound and walk for the duration of the simulation, with walking velocity updated using Eq. B.3. Fig. B.2 shows the force production of the motor with varying zero-force walking velocity $v_0 = 10\ nm/s$. We observe distinct mechanosensation behavior which is characterized by a sharp transition to force generation above $K_t = 0.1\ pN/nm$, consistent with previous computational works [1, 175]. For all stiffer $K_t$ values, the motor filaments show a convergence in force generation to 12 $pN$.

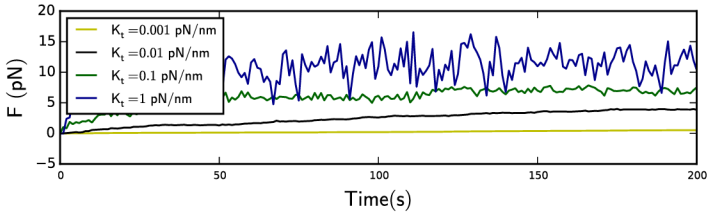


Figure B.2: Validation of motor force production for zero-force velocity $v_0 = 10$ $nm/s$. All values above $K_t = 0.1\ pN/nm$ converge to the expected stall force of 12 $pN$, with a sharp transition to force generation above this stiffness.

Finally, to briefly validate the Gillespie stochastic simulation of cross-linker binding and unbinding, we ran the simulator for a set $n_p = 100$ possible binding sites, with filaments remaining static for the duration of a simulation of $10^6$ chemical reaction steps. Fig. B.3 shows the number of bound cross-linkers $n$ for varying cross-linker binding and unbinding rates $k_{on}^{cl}$ and $k_{off}^{cl}$. From simple kinetic theory, we know that the probability of a bound site being occupied will be $P(bound) = k_{on}^{cl}/(k_{off}^{cl} + k_{on}^{cl})$ such that the average number of bound cross-linkers $\langle n \rangle = n_p P(bound)$. As Fig. B.3 shows, this agreement is achieved with our simulator.

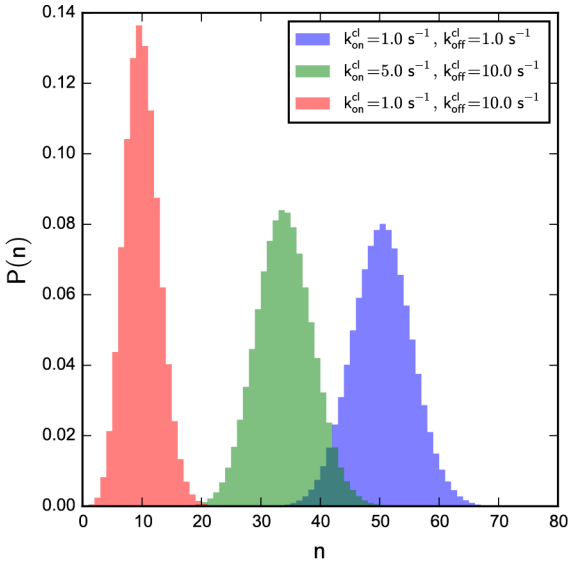


Figure B.3: Gillespie stochastic simulations for varying $k_{on}^{cl}$ and $k_{on}^{cl}$. The $\langle n \rangle$ for each set of kinetic parameters agrees well with the expected value from $P(bound)$.

## B.3 Power-law behavior of the passive force dipole

We here perform a short-time and asymptotic analysis of the contraction equation presented in this paper (Eq 3.7). We rewrite the original contraction ODE as:

$$\frac{dl_o}{dt} = ae^{-\gamma l_o} - bl_o e^{-\gamma l_o}, \tag{B.6}$$

where $a \equiv \epsilon/(1+v\cdot e^{-\epsilon/k_bT})2K_t\eta$, $b \equiv K_t/\eta$, and $\gamma \equiv ln(c)/\Delta$ where $c \equiv 1+v^{-1}e^{\epsilon/k_bT}$. We can also write the predicted steady-state overlap as $l_o^{ss} \equiv \frac{b}{a}$. This equation is now separable and yields:

$$\mathrm{Ei}(-\gamma l_o^{ss}) - \mathrm{Ei}\Big(\gamma\Big(l_o - l_o^{ss}\Big)\Big) = bte^{-\gamma l_o^{ss}} \tag{B.7}$$

where $\mathrm{Ei}(\cdot)$ represents the exponential integral $\mathrm{Ei}(x) = -\int_{-x}^{\infty} e^{-x}dx/x$. We can expand in the short time limit, i.e. at $l_o \to 0$, $\mathrm{Ei}(\gamma(l_o - l_o^{ss})) \approx \mathrm{Ei}(-\gamma l_o^{ss}) - (l_o/l_o^{ss})e^{-\gamma l_o^{ss}} + O(l_o^2)$ to give a linear force-generating regime:

$$l_o \approx \frac{\epsilon}{(1 + v \cdot e^{-\epsilon/k_bT})}\frac{1}{2\Delta\eta}t. \tag{B.8}$$

Thus the predicted sliding velocity of the filaments is $V_o^{cl} = \frac{\epsilon P_o^{cl}}{2\Delta\eta}$ in absence of kinetic arrest. In the long time limit we can expand around $l_o = l_o^{ss}$ such that approximately $\mathrm{Ei}(\gamma(l_o - l_o^{ss})) \approx \ln(\gamma(l_o^{ss} - l_o))$. This immediately gives an exponentially decaying overlap function to steady state:

$$l_o \approx l_o^{ss} - \left[\frac{1}{\gamma}\mathrm{Ei}(\gamma l_o^{ss})\right]e^{-bc^{-l_o^{ss}/\Delta}t} \tag{B.9}$$

where the timescale of approaching steady state is given as $1/\tau_{ss} = bc^{-l_o^{ss}/\Delta} = \frac{K_t}{\eta}(1 + v^{-1}e^{\epsilon/k_bT})^{-l_o^{ss}/\Delta}$. To differentiate between the two power law regimes, a transition time $\tau_{trans}$ is chosen when the slope of the time-series in $l_o$ deviates by

10% for each cross-linker energy $\epsilon$.

## B.4 Kinetic behavior of the active force dipole

We here derive the governing equation of the dynamics of the motor filament and cross-linkers in the two-filament system. First, expressions are needed to define the distance in which the filament pair moves, over a time $\tau$, in the various states where inter-filament movement occurs ($m = 0, +1$, and $n = 0$). We first consider the extension event ($m = 0$, $n = 0$). Solving the simple kinematic equation for a relaxation against the $K_t$ tether, with starting position $l_o$, one obtains an extension distance:

$$\xi_0(l_o, \tau) = l_o\Big(1 - \exp\Big(\frac{-K_t}{2\eta}\tau\Big)\Big). \tag{B.10}$$

Similarly, for the contraction distance, considering the ($m = 1$, $n = 0$) state relaxation over a time $\tau$:

$$\chi_0(l_o, l_w, \tau) = \Big(\frac{K_m}{K_{eff}}(l_o + l_w) - l_o\Big)\Big(1 - \exp\Big(\frac{-K_{eff}}{2\eta}\tau\Big)\Big), \tag{B.11}$$

where we have defined $K_{eff} = K_m + K_t$. The contraction distance $r$ also depends on the walk length of the motor $l_w$, which will be derived. If we are considering a chemical reaction with rate constant $k_r$ in our system which stops the contraction or extension motion, we must average $\chi$ and $\xi$ over the possible holding times of that reaction, $P(\tau|k_r) = k_r\exp(-k_r\tau)$. Evaluating $\bar{\xi}(l_o) = \int_0^\infty \xi_0(l_o, \tau)P(\tau|k_r)d\tau$ and $\bar{\chi}(l_o, l_w) = \int_0^\infty \chi_0(l_o, l_w, \tau)P(\tau|k_r)d\tau$, we have

$$\bar{\chi}(l_o, k_r) = l_o\left(1 + \tfrac{2\eta k_r}{K_t}\right)^{-1}, \text{and} \tag{B.12}$$

$$\bar{\xi}(l_o, l_w, k_r) = \left(\tfrac{K_m}{K_{eff}}(l_o + l_w) - l_o\right)\left(1 + \tfrac{2\eta k_r}{K_{eff}}\right)^{-1}. \tag{B.13}$$

We must now consider the walk length of the motor filament in a time $\tau$, $l_w = \int_0^\tau v_w dt$, since it fundamentally depends on the kinetics of the reactions leading up to a contraction event. We consider the motor filament walking in the $n \neq 0$ state such that $F_m \approx K_m l_w$. The motor filament walk length time is controlled by cross-linker unbinding, since we must consider another kinematic process once $n = 0$. We approximate the motor filament stall-force relation in Eq. B.3 as:

$$v_w(F) \approx v_w^0(1 - K_m l_w / F_s). \tag{B.14}$$

This is simply a linear approximation of Eq. B.3 which accounts for the $F = 0$ and $F = F_s$ behavior. Integrating this equation for $l_w$, and averaging over all possible cross-linker unbinding times with rate $k_u^{cl}$ as $\bar{l}_w(l_o) = \int_0^\infty l_w(l_o, \tau) P(\tau | k_u^{cl}) d\tau$, we have:

$$\bar{l}_w^{n=0}(l_o) = \frac{F_s}{K_m}\left(1 + \frac{F_s k_u^{cl}(l_o)}{K_m v_w^0}\right)^{-1}. \tag{B.15}$$

We can then write the final contraction equation as:

$$\bar{\chi}(l_o, k_r) = \left[\frac{K_m}{K_{eff}}\left(l_o + l_w^{n=0}(l_o)\right) - l_o\right]\left(1 + \frac{2\eta k_r}{K_{eff}}\right)^{-1}. \tag{B.16}$$

To write full expressions for $\chi(l_o)$ and $\xi(l_o)$ as observed in simulation, we must consider the possible series of reaction events and their probabilities when a contraction or extension event takes place. Because all random variables considered are

exponential holding times, we can easily compute probabilities of events $E_a$ and $E_b$ happening in succession via the memoryless property: $P(\tau_a > \tau + \tau_b) = P(\tau_a > \tau)$. $P(\tau_a < \tau_b)$, which describes the probability of $E_a$ occuring before $E_b$, is simply:

$$P(\tau_a < \tau_b) = \int_0^\infty \int_0^{d\tau'} k_a e^{-k_a \tau} k_b e^{-k_b \tau'} d\tau d\tau' = \frac{k_a}{k_a + k_b}. \tag{B.17}$$

We now use a first-moment approximation of the actual distribution of contraction distances by considering the succession of kinetic events possible, their mean behavior and their probabilities of occurence. With this in mind, the contraction function $\chi(l_o)$ can be written as:

$$\begin{aligned}\chi(l_o) \approx \quad & \underbrace{\left[\bar{\chi}(l_o, k_b^{cl}) + \bar{l}_w^{n\neq 0}(l_o)\right]}_{n\to 1} P(\tau_b^{cl} < \tau_u^m) + \underbrace{\left[\bar{\xi}\left(\bar{\chi}_\infty, k_b^{cl}\right)\right]}_{m\to 0,\ n\to 1} P(\tau_u^m < \tau_b^{cl}) P(\tau_b^{cl} < \tau_u^m) \\ & \underbrace{\left[\bar{\xi}\left(\bar{\chi}_\infty, k_b^{m}\right) + \bar{l}_w^{n\neq 0}(l_o)\right]}_{m\to 0,\ m\to 1,\ n\to 1} P(\tau_u^m < \tau_b^{cl}) P(\tau_b^{m} < \tau_b^{cl}) P(\tau_b^{cl} < \tau_u^m) + ...\end{aligned} \tag{B.18}$$

We have denoted the function $\bar{l}_w^{n\neq 0}(l_o)$ for the walk length of a motor filament walking against the $K_t$ tether in the approximation $K_t << K_m$ such that $F_m \approx K_t l_w$, in a similar manner to Eq. B.15. The first term in this equation describes the simple probabilistic pathway where $n \to 1$ before motor filament unbinding. The latter branches are the various pathways in which the motor filament can become (un)bound before cross-linkers rebind. We have defined $\bar{\chi}_\infty$ to be the long-time limit of Eq. B.16 such that $k_r \to 0$. Since this pathway is only probable if $P(\tau_u^m < \tau_b^{cl})$, we can safely assume that $\bar{\chi}$ relaxes fully in this case since $\tau_u^m >> K_m/2\eta$. The second branch describes the series of events in which $m \to 0$ and $n \to 1$ occur

in succession. The third branch describes the motor re-binding before cross-linker binding such that $m \to 0$, $m \to 1$, and $n \to 1$ occur in succession. The frequency of the ratcheting $w_\chi(l_o)$ is simply:

$$w_\chi(l_o) \approx \left( \frac{\bar{\tau}_b^{cl}(l_o) + \bar{\tau}_u^{cl}(l_o)}{\rho_m} \right)^{-1} \tag{B.19}$$

where we have defined the motor duty ratio in the zero-force limit: $\rho_m = k_u^m/(k_u^m + k_b^m)$. In a similar manner to $\chi(l_o)$, an extension function $\xi(l_o)$ can be written in a first-moment approximation as:

$$\begin{aligned} \xi(l_o) \approx \quad & \underbrace{\left[ \bar{\xi}(l_o, k_b^{cl}) \right]}_{n \to 1} P(\tau_b^{cl} < \tau_b^m) + \\ & \underbrace{\left[ \bar{\xi}(l_o, k_b^m) + \bar{l}_w^{n \neq 0}(l_o) \right]}_{m \to 1,\ n \to 1} P(\tau_b^m < \tau_b^{cl}) P(\tau_b^{cl} < \tau_u^m) + ... \end{aligned} \tag{B.20}$$

with a frequency:

$$w_\xi(l_o) \approx \left( \frac{\bar{\tau}_b^{cl}(l_o) + \bar{\tau}_u^{cl}(l_o)}{1 - \rho_m} \right)^{-1} \tag{B.21}$$

where the first branch describes $n \to 1$ before motor filament binding. The second branch then describes the case of $m \to 1$ and $n \to 1$ in succession. The steady-state solution for $l_o$ by solving $V_{eff} = 0$, i.e. $\rho_m \bar{\chi}(l_o) = (1 - \rho_m)\bar{\xi}(l_o)$, is not analytically tractable.

## B.5 MEDYAN parameters used in three-dimensional force dipoles

| **Parameter** | **Description** | **Value [for stochastic kinetics]** |
|---|---|---|
| $D_a$ | Actin diffusion coefficient | 20 $\mu m^2 \cdot s^{-1}[80 s^{-1}]$ * |
| $D_{cl}$ | $\alpha$-actinin diffusion coefficient | $D_a/10$ $uM^{-1} \cdot s^{-1}$ |
| $D_m$ | Motor filament diffusion coefficient | $D_a/100$ $uM^{-1} \cdot s^{-1}$ |
| $k_{b,u}^{cl}$ | Cross-linker unbinding rate | $\epsilon$-dependent, 1.0 $s^{-1}$ [95] |
| $l_c$ | Length of actin filament segment | 108 $nm$ |
| $l_p$ | Actin filament persistence length | 17 $\mu m$ [138] |
| $\epsilon_{bend}$ | Actin filament bending energy | 672 $pN \cdot nm$ |
| $K_{str}$ | Actin filament stretching constant | 100 $pN/nm$ |
| $K_{vol}$ | Actin filament excluded volume constant | $10^5$ $pN/nm^4$ |
| $N$ | Number of compartments in each dimension | $6, 6, 6$ |
| $l_K$ | Kuramoto (compartment) length | 500 $nm$ * |
| $g_{tol}$ | Gradient minimization tolerance | 0.1 $pN$ * |
| $t_{min}$ | Timestep between mechanical equilibration | 0.05 $s$ * |

Table B.2: Parameters chosen to mimic a typical system of actin filaments, cross-linkers, and non-muscle myosin IIA motor filaments in three-dimensional *MEDYAN* simulations of an actomyosin force dipole. All other parameters and models used in the one-dimensional stochastic "toy" representation, but not included in this table, are directly implemented as in the previous model. This includes motor and cross-linker mechanosensitivity. * - An explanation of this parameter is given in the original *MEDYAN* paper [148].

## B.6 Supplemental data

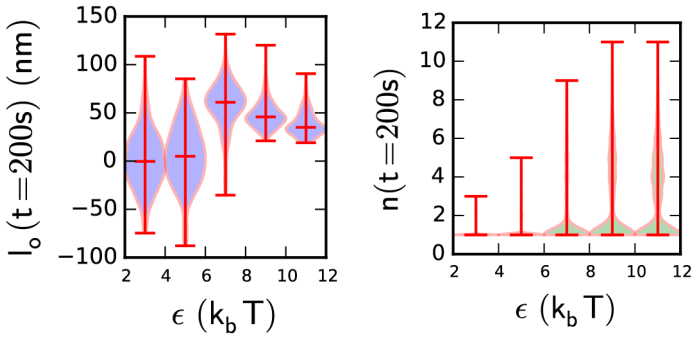


Figure B.4: Distribution of cross-linkers bound to the actin filament pair and overlap in one dimensional dipole. As $\epsilon$ is varied, overlap distributions transition to non-Gaussian. Number of bound cross-linkers follow a bimodal distribution.

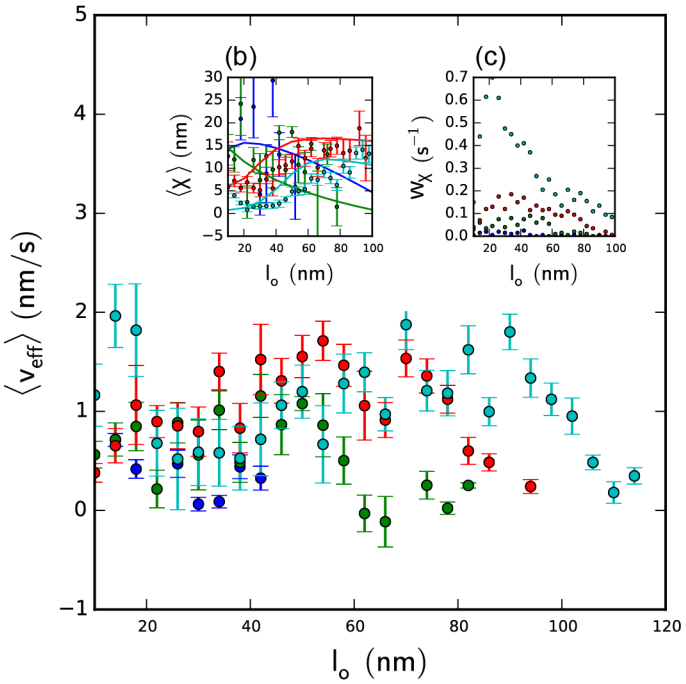


Figure B.5: Effect of kinetics in one-dimensional force dipole. As $k_u^{cl}$ is increased, approaching the thermodynamic limit, the dipole can more efficiently ratchet with less slippage. $k_u^{cl}$ is plotted at 0.01, 0.1, 1, and 10 /s in blue, green, red, and cyan, respectively.

# Appendix C: Supporting information for Chapter 4

## C.1 Correlation functions in supplemental information

For a representation of local pairwise filament structure, a radial distribution function $g(r)$ of the cylinder ensemble can be written as:

$$g(r) = \frac{1}{4\pi r^2 \rho N} \Big\langle \delta(r - |\mathbf{r}_i - \mathbf{r}_j|) \Big\rangle. \tag{C.1}$$

This function is a representation of the relative local density of actin cylinders in the vicinity $r$ of any given cylinder for a system with overall system concentration $\rho = N/V$. Here, averaging occurs over all pairs of cylinders. With this we will be able to see when actin structures transition in local density when sufficiently adding passive and active cross-links.

To extend to spatiotemporal behavior, we introduce a displacement correlation function $u(r, \Delta t)$ dependent on both a spatial distance $r$ and time delay $\Delta t$, but similar in form to $g(r)$:

$$u(r, \Delta t) = \frac{\Big\langle \mathbf{u}_i(\Delta t) \cdot \mathbf{u}_j(\Delta t) \delta(r - |\mathbf{r}_i - \mathbf{r}_j|) \Big\rangle}{\langle \mathbf{u}(\Delta t) \rangle^2 4\pi r^2 \rho N} \tag{C.2}$$

This relates the correlation in displacement vectors $\mathbf{u}_i$ over a time $\Delta t$ as a function

of particle separation $r$, giving a measure of correlations in displacement rather than purely position as in $g(r)$. Similar to $g(r)$ this averaging occurs over pairs of cylinders. From this, an "excess" displacement correlation function is given by $\Gamma(r, \Delta t) = u(r, \Delta t)/g(r) - 1$, which normalizes the local density contribution in displacement correlation.

## C.2 Simulation parameters

| Parameter | Description | Value [for stochastic kinetics] |
|---|---|---|
| $D_a$ | Actin diffusion coefficient | 20 $\mu m^2 \cdot s^{-1}[80 s^{-1}]$ ** |
| $D_{cl}$ | $\alpha$-actinin diffusion coefficient | $D_a/10\ uM^{-1} \cdot s^{-1}$ |
| $D_m$ | Motor filament diffusion coefficient | $D_a/100\ uM^{-1} \cdot s^{-1}$ |
| $k_{b,u}^{ms}$ | Single motor head (un)binding rate | $0.2/s, 1.7/s$ [95] * |
| $k_{b,u}^{cl}$ | Cross-linker unbinding rate | $\epsilon$-dependent, 1.0 $s^{-1}$ [95] |
| $N_t$ | Number of single motor heads per side of motor filament | 30 [20] |
| $\epsilon$ | Cross-linker binding energy | $0 - 15\ k_bT$ |
| $v_m$ | Effective volume of cross-linker in solution | $1 \cdot 10^{-3}\ \mu m^3$ * |
| $v_b$ | Approximate bound volume of cross-linker | $3 \cdot 10^{-6}\ \mu m^3$ * |
| $\Delta$ | Distance between cross-link binding sites | 21 $nm$ |
| $d_s$ | Motor filament step size | 5 $nm$ [129] |
| $F_s$ | Motor filament stall force | 35 $pN$ * |
| $l_0$ | Length of actin filament segment | 108 $nm$ |
| $l_p$ | Actin filament persistence length | 17 $\mu m$ [138] |
| $\epsilon_{bend}$ | Actin filament bending energy | 672 $pN \cdot nm$ |
| $K_{str}$ | Actin filament stretching constant | 100 $pN/nm$ |
| $K_{vol}$ | Actin filament excluded volume constant | $10^5\ pN/nm^4$ |
| $K_{ms}$ | Motor head stiffness | 0.5 $pN/nm$ [187] |
| $K_{cl}$ | Cross-linker stiffness | 8 $pN/nm$ [201] |
| $v_w^0$ | Walking velocity of motor filament | 10 $nm/s$ * |
| $\alpha$ | Stall velocity mechanochemical parameter for motor filament | 0.2 [49] |
| $\beta$ | Catch-bond mechanochemical paramter for motor filament | 2 [49] |
| $x_{cl}$ | Characteristic slip-length for cross-linker | 0.5 $nm$ [52] |
| $x_m$ | Characteristic catch-length for single motor head | 1.6 $nm$ [68] |
| $K_t$ | Boundary tether stiffness | 1 $pN/nm$ |
| $N$ | Number of compartments in each dimension | 6 |
| $l_K$ | Kuramoto (compartment) length | 500 $nm$ ** |
| $g_{tol}$ | Gradient minimization tolerance | 5 $pN$ ** |
| $t_{min}$ | Timestep between mechanical equilibration | 0.1 $s$ ** |

Table C.1: Model parameters chosen to mimic a typical system of actin filaments, cross-linkers, and non-muscle myosin IIA motor filaments. * - An explanation of this parameter is given in the accompanying work [93]. ** - An explanation of this parameter is given in the original MEDYAN paper [148].

## C.3 Supplemental data

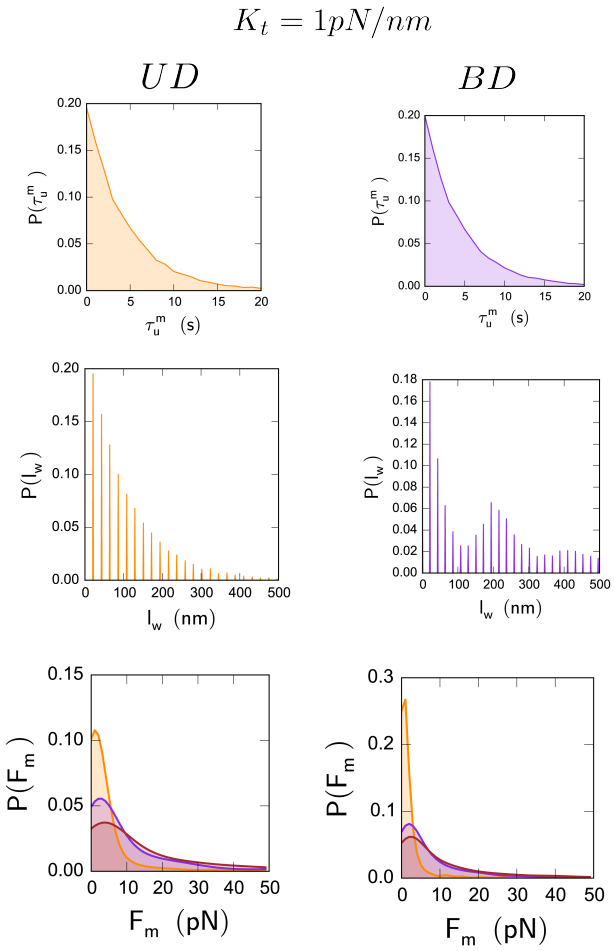


Figure C.1: Motor bound lifetimes, walk lengths, and force in a tethered disordered network. Motor observables remain quite similar in the free boundary case. Top: Probability distribution of bound lifetimes of motor (mean unbinding time) $P(\tau_u^m)$ stays similar over all $\epsilon$ simulated for both uni- and bi-directional case - $\epsilon = 7k_bT$ is shown. This indicates little activation of the myosin II catch bond in dynamics. Middle: Discrete probability distribution of walking length in motors $P(l_w)$ in increments of $\Delta = 21nm$. Interestingly, the bi-directional motor has a multimodal walk length distribution. This can be explained by the extra conformational freedom of the bi-directional motor to walk in direction of decreased stress, unlike the uni-directional motor which necessarily walks and stalls towards the plus end. Bottom: Probability distribution of forces in motors $P(F_m)$ shows increase for $\epsilon$ values with both motor types.

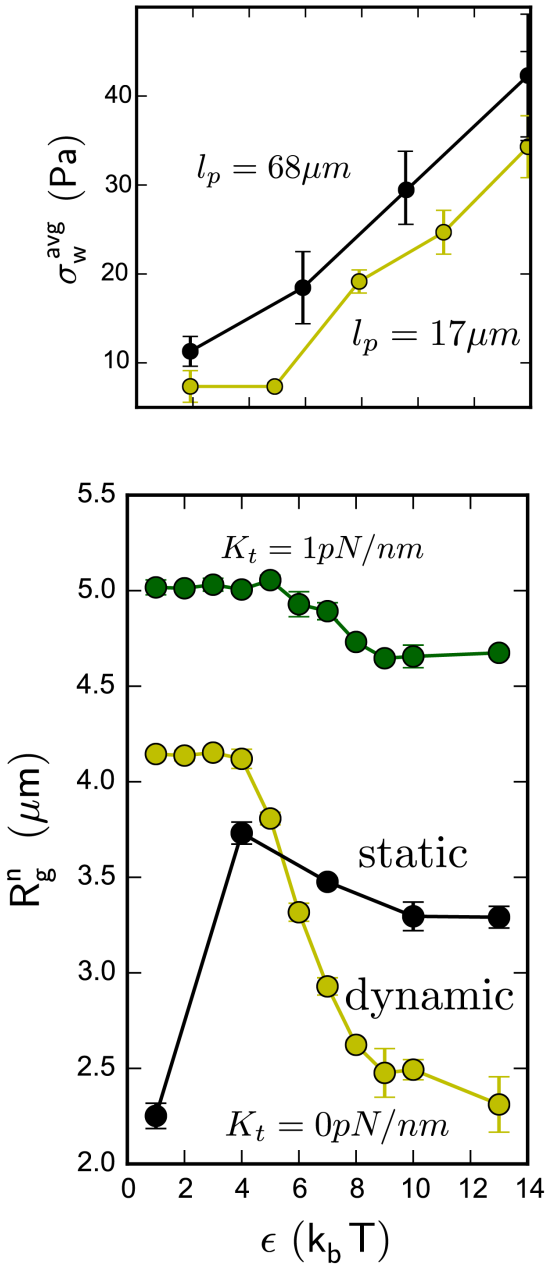


Figure C.2: Effect of persistence length and static connectivity in disordered network. Top: An increased persistence length $l_p = 68\mu m$ compared to the physiological $l_p = 17\mu m$ shows little effect on overall stress produced by the disordered network. Bottom: We also compare geometric collapse in the case of static cross-linkers (black) with same probability of occupancy as in the transient case: $P_o^{cl} = (1 + \frac{v_m}{v_b} \cdot exp(-\epsilon/k_bT))^{-1}$. This gives an interesting effect - networks highly collapse with minimal yet non-zero static linkages and directional motor activity. At higher static connectivities, network collapse is minimal as expected. This overall gives a monotonically decreasing collapse with cross-linker affinity, unlike when cross-linkers are dynamic.

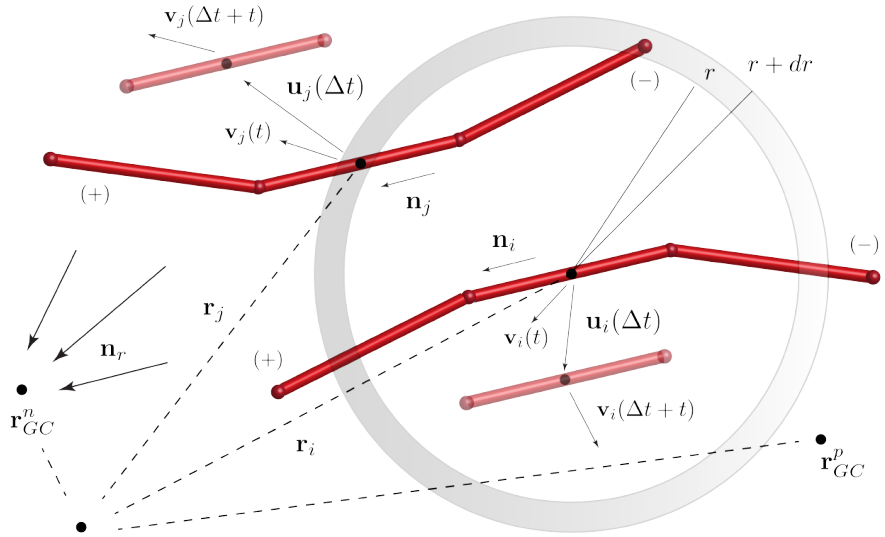


Figure C.3: Actomyosin network geometry used in correlation analysis. Actin filaments are cylindrical elements connected by hinge-points with defined plus and minus ends. The vector $\mathbf{r}_i$ represents the cylinder position (center of mass) in space and the vector $\mathbf{n}_i$ represents its normal direction from minus to plus end. The cylinders' geometric orientation relative to the radial vector $\mathbf{n}_r$ can be taken as a dot product. In the case of pairwise correlation functions, averaging of pairwise interactions occurs over all cylinders $i$ and $j$ in range $r$ to $r + dr$. In some time delay $\Delta t$ the displacement $\mathbf{u}_i$of the $i$th cylinder can be calculated and included in the pair distribution. For velocity auto-correlation, a cylinders instantaneous velocity (at minimum snapshot frequency $t_s = 5s$) is compared to itself at a different time $t + \Delta t$.

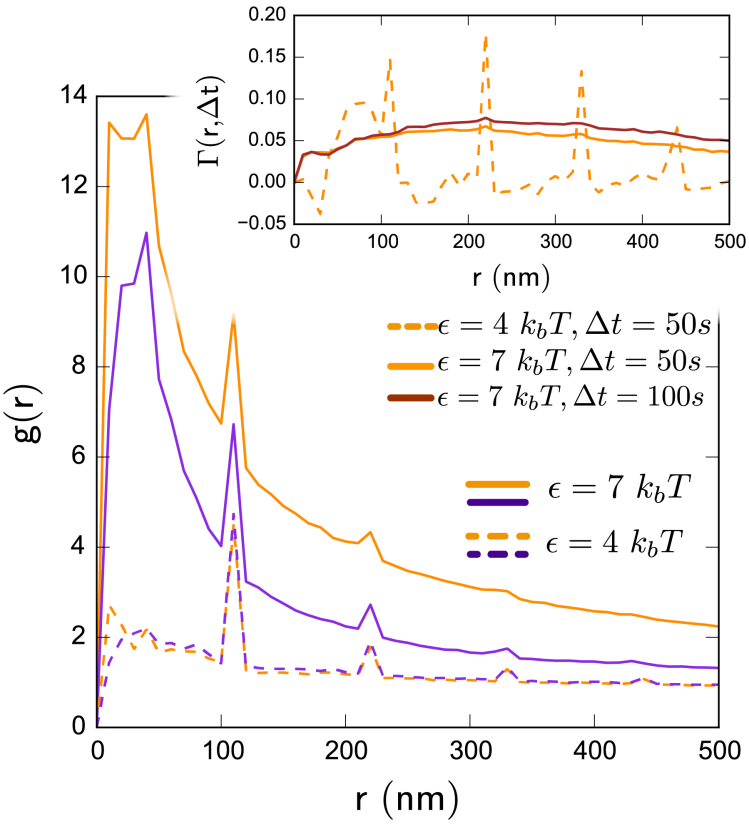


Figure C.4: Structure and dynamics of geometrically contracted actomyosin as a function of cross-linker binding strength $\epsilon$. Colors for uni-directional and bi-directional motors are similar to main text $g(r)$ pairwise distribution of actin filament cylindrical segments with various energies $\epsilon$ shown as additional dotted lines at steady-state. At $\epsilon_{lab}$, a sharp transition to large local density occurs synonymously with global aggregation. Significant peaks also result due to $108nm$-spaced cylinder neighbors on the same polymer chain. Bottom: $\Gamma(r, \Delta t)$ displacement correlation function for uni-directional motors only with varying $\epsilon$. At significant time delays, this function shows a transition to correlations at large length scales at $\epsilon_{lab}$. Below this threshold, the system displays correlation due to cross-linking at a length $\sim 75nm$.

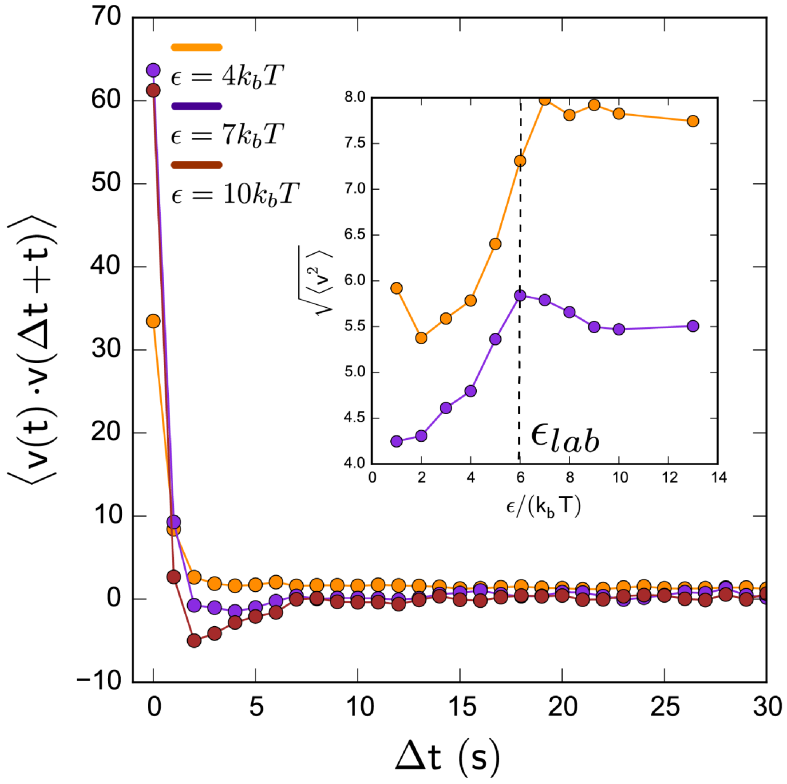


Figure C.5: Velocity-velocity autocorrelation function $v(\Delta t) = \left\langle \mathbf{v}(\Delta t + t) \cdot \mathbf{v}(t) \right\rangle$ for various energies and uni-directional motor driving against $K_t = 1pN/nm$ external tethers, as a function of time delay $\Delta t$. As $\epsilon$ is varied through $\epsilon_{lab}$, a transition from sustained correlations of velocity at large time delay to a more typical profile containing recoil at short time delays is observed. Inset shows the mean-square velocity of cylinders at steady state, which shows the biphasic relationship between cross-linking and filament motion analytically derived in [93].

# Bibliography


[1] Albert, P. J., Erdmann, T., and Schwarz, U. S. Stochastic dynamics and mechanosensitivity of myosin II minifilaments. *New J. Phys. 16* (2014).

[2] Alberts, B., Johnson, A., Lewis, J., Raff, M., Roberts, K., and Walter, P. *Molecular biology of the cell*, 4 ed. Garland Science, New York, 2002.

[3] Alberts, J. B., and Odell, G. M. In silico reconstitution of Listeria propulsion exhibits nano-saltation. *PLoS Biol. 2*, 12 (2004), e412.

[4] Alvarado, J., Sheinman, M., Sharma, A., MacKintosh, F. C., and Koenderink, G. H. Molecular motors robustly drive active gels to a critically connected state. *Nat. Phys. 9*, 9 (2013), 591–597.

[5] Alvarado, J., Sheinman, M., Sharma, A., MacKintosh, F. C., and Koenderink, G. H. Force percolation of contractile active gels. *Soft Matter 13*, 34 (2017), 5624–5644.

[6] Andrews, S. S., and Bray, D. Stochastic simulation of chemical reactions with spatial resolution and single molecule detail. *Phys. Biol. 1*, 3-4 (2004), 137–151.

[7] Andrianantoandro, E., and Pollard, T. D. Mechanism of Actin Filament Turnover by Severing and Nucleation at Different Concentrations of ADF/Cofilin. *Mol. Cell 24*, 1 (2006), 13–23.

[8] Atilgan, E., Wirtz, D., and Sun, S. X. Morphology of the lamellipodium and organization of actin filaments at the leading edge of crawling cells. *Biophys. J. 89*, 5 (2005), 3589–3602.

[9] Azatov, M., Goicoechea, S. M., Otey, C. A., and Upadhyaya, A. The actin crosslinking protein palladin modulates force generation and mechanosensitivity of tumor associated fibroblasts. *Sci. Rep. 6* (2016), 28805.

[10] Baird, M. A., Billington, N., Wang, A., Adelstein, R. S., Sellers, J. R., Fischer, R. S., and Waterman, C. M. Local pulsatile contractions are an intrinsic property of the myosin 2A motor in the cortical cytoskeleton of adherent cells. *Mol. Biol. Cell* (2016).

[11] Bastian, P., Lang, K., Niggemann, B., Zaenker, K. S., and Entschladen, F. Myosin regulation in the migration of tumor cells and leukocytes within a three-dimensional collagen matrix, 2005.

[12] Bendix, P. M., Koenderink, G. H., Cuvelier, D., Dogic, Z., Koeleman, B. N., Brieher, W. M., Field, C. M., Mahadevan, L., and Weitz, D. a. A quantitative analysis of contractility in active cytoskeletal protein networks. *Biophys. J. 94*, 8 (2008), 3126–3136.

[13] Berardi, R., Fava, C., and Zannoni, C. A GayBerne potential for dissimilar biaxial particles. *Chem. Phys. Lett. 297*, 1-2 (1998), 8–14.

[14] Bernstein, B. W., and Bamburg, J. R. ADF/Cofilin: A functional node in cell biology. *Trends Cell Biol. 20*, 4 (2010), 187–195.

[15] Bertling, E., and Hotulainen, P. New waves in dendritic spine actin cytoskeleton: From branches and bundles to rings, from actin binding proteins to post-translational modifications. *Mol. Cell. Neurosci.*, May (2016).

[16] Betzig, E., Betzig, E., Patterson, G. H., Sougrat, R., Lindwasser, O. W., Olenych, S., Bonifacino, J. S., Davidson, M. W., Lippincott-schwartz, J., and Hess, H. F. Imaging Intracellular Fluorescent Proteins at Nanometer Resolution. *Science 1642*, 2006 (2013), 1642–1646.

[17] Bi, E., Maddox, P., Lew, D. J., Salmon, E. D., McMillan, J. N., Yeh, E., and Pringle, J. R. Involvement of an actomyosin contractile ring in Saccharomyces cerevisiae cytokinesis. *J. Cell Biol. 142*, 5 (1998), 1301–1312.

[18] Bi, E., and Park, H. O. Cell polarization and cytokinesis in budding yeast. *Genetics 191*, 2 (2012), 347–387.

[19] Bidone, T. C., Tang, H., and Vavylonis, D. Dynamic Network Morphology and Tension Buildup in a 3D Model of Cytokinetic Ring Assembly. *Biophys. J. 107*, 11 (2014), 2618–2628.

[20] Billington, N., Wang, A., Mao, J., Adelstein, R. S., and Sellers, J. R. Characterization of three full-length human nonmuscle myosin II paralogs. *J. Biol. Chem. 288*, 46 (2013), 33398–33410.

[21] Bishop, A. L., and Hall, A. Rho GTPases and their effector proteins. *Biochem. J. 348 Pt 2* (2000), 241–55.

[22] Blackwell, R., Sweezy-Schindler, O., Baldwin, C., Hough, L. E., Glaser, M. A., and Betterton, M. D. Microscopic origins of anisotropic active stress in motor-driven nematic liquid crystals. *Soft Matter 12*, 10 (2016), 2676–2687.

[23] Blanchoin, L., Amann, K., Higgs, H., Marchand, J., Kaiser, D., and Pollard, T. Direct observation of dendritic actin complex and WASP / Scar proteins. *Nature 171*, 1994 (2000), 1007–1011.

[24] Blanchoin, L., Boujemaa-Paterski, R., Sykes, C., and Plastino, J. Actin Dynamics, Architecture, and Mechanics in Cell Motility. *Physiol. Rev. 94*, 1 (2014), 235–263.

[25] Burroughs, N. J., and Marenduzzo, D. Three-dimensional dynamic Monte Carlo simulations of elastic actin-like ratchets. *J. Chem. Phys. 123*, 17 (2005), 174908.

[26] Butt, T., Mufti, T., Humayun, A., Rosenthal, P. B., Khan, S. S., Khan, S. S., and Molloy, J. E. Myosin motors drive long range alignment of actin filaments. *J. Biol. Chem. 285*, 7 (2010), 4964–4974.

[27] Cao, Y., Li, H., and Petzold, L. Efficient formulation of the stochastic simulation algorithm for chemically reacting systems. *J. Chem. Phys. 121*, 9 (2004), 4059–4067.

[28] Carlsson, A. E. Growth velocities of branched actin networks. *Biophys. J. 84*, 5 (2003), 2907–2918.

[29] Carlsson, A. E. Contractile stress generation by actomyosin gels. *Phys. Rev. E - Stat. Nonlinear, Soft Matter Phys. 74*, April (2006), 1–6.

[30] Carrillo, J.-M. Y., MacKintosh, F. C., and Dobrynin, A. V. Nonlinear Elasticity: From Single Chain to Networks and Gels. *Macromolecules 46*, 9 (2013), 3679–3692.

[31] Cavalier-Smith, T. The origin of nuclei and of eukaryotic cells. *Nature 256*, 5517 (1975), 463–468.

[32] Cavalier-Smith, T. The phagotrophic origin of eukaryotes and phylogenetic classification on protozoa, 2002.

[33] Chu, J.-W., and Voth, G. A. Coarse-grained modeling of the actin filament derived from atomistic-scale simulations. *Biophys. J. 90*, 5 (2006), 1572–1582.

[34] Craig, E. M., Dey, S., and Mogilner, A. The emergence of sarcomeric , graded-polarity and spindle-like patterns in bundles of short cytoskeletal polymers and two opposite molecular motors. *J. Phys. Condens. Matter 23*, 37 (2011), 374102.

[35] Cramer, L. P., Siebert, M., and Mitchison, T. J. Identification of Novel Graded Polarity Actin Filament Bundles in Locomoting Heart Fibroblasts: Implications for the Generation of Motile Force. *J. Cell Biol. 136*, 6 (1997), 1287–1305.

[36] Cyron, C. J., Müller, K. W., Bausch, A. R., and Wall, W. a. Micromechanical simulations of biopolymer networks with finite elements. *J. Comput. Phys. 244* (2013), 236–251.

[37] Cyron, C. J., Müller, K. W., Schmoller, K. M., Bausch, A. R., Wall, W. A., and Bruinsma, R. F. Equilibrium phase diagram of semiflexible polymer networks with linkers. *Europhys. Lett. 102*, 3 (2013), 38003.

[38] Cyron, C. J., and Wall, W. A. Finite-element approach to Brownian dynamics of polymers. *Phys. Rev. E - Stat. Nonlinear, Soft Matter Phys. 80*, 6 (2009), 1–12.

[39] Dasanayake, N. L., and Carlsson, A. E. Stress generation by myosin minifilaments in actin bundles. *Phys. Biol. 10*, 3 (2013), 036006.

[40] Dasanayake, N. L., Michalski, P. J., and Carlsson, A. E. General mechanism of actomyosin contractility. *Phys. Rev. Lett. 107*, 11 (2011), 1–4.

[41] Delorme, V., Machacek, M., DerMardirossian, C., Anderson, K. L., Wittmann, T., Hanein, D., Waterman-Storer, C., Danuser, G., and Bokoch, G. M. Cofilin Activity Downstream of Pak1 Regulates Cell Protrusion Efficiency by Organizing Lamellipodium and Lamella Actin Networks. *Dev. Cell 13*, 5 (2007), 646–662.

[42] Didonna, B. a., and Levine, A. J. Unfolding cross-linkers as rheology regulators in F-actin networks. *Phys. Rev. E - Stat. Nonlinear, Soft Matter Phys. 75*, 4 (2007), 1–10.

[43] Duke, T. A. Molecular model of muscle contraction. *Proc. Natl. Acad. Sci. 96*, 6 (1999), 2770–2775.

[44] Edelstein-Keshet, L., and Ermentrout, G. B. A model for actin-filament length distribution in a lamellipod. *J. Math. Biol. 43*, 4 (2001), 325–355.

[45] Egelman, E. H., Francis, N., and Derosier, D. J. F-actin is a helix with a random variable twist. *Nature 298*, 5870 (1982), 131–135.

[46] Ehrlicher, A. J., Krishnan, R., Guo, M., Bidan, C. M., Weitz, D. A., and Pollak, M. R. Alpha-actinin binding kinetics modulate cellular dynamics and force generation. *Proc. Natl. Acad. Sci. U. S. A. 112*, 21 (2015).

[47] Elliott, C. M., Stinner, B., and Venkataraman, C. Modelling cell motility and chemotaxis with evolving surface finite elements. *J. R. Soc. Interface 9* (2012), 3027–3044.

[48] Ennomani, H., Letort, G., Guérin, C., Martiel, J.-L., Cao, W., Nédélec, F., De La Cruz, E. M., Théry, M., and Blanchoin, L. Architecture and Connectivity Govern Actin Network Contractility. *Curr. Biol. 26*, 5 (2016), 616–626.

[49] Erdmann, T., Albert, P. J., and Schwarz, U. S. Stochastic dynamics of small ensembles of non-processive molecular motors: The parallel cluster model. *J. Chem. Phys. 139*, 17 (2013), 175104.

[50] Falzone, T. T., Blair, S., and Robertson-Anderson, R. M. Entangled F-actin displays a unique crossover to microscale nonlinearity dominated by entanglement segment dynamics. *Soft Matter 11*, 22 (2015), 4418–23.

[51] Fass, J., Pak, C., Bamburg, J., and Mogilner, A. Stochastic simulation of actin dynamics reveals the role of annealing and fragmentation. *J. Theor. Biol. 252*, 1 (2008), 173–183.

[52] Ferrer, J. M., Lee, H., Chen, J., Pelz, B., Nakamura, F., Kamm, R. D., and Lang, M. J. Measuring molecular rupture forces between single actin filaments and actin-binding proteins. *Proc. Natl. Acad. Sci. 105*, 34 (2008), 9221–9226.

[53] Flegg, M. B., Chapman, S. J., and Erban, R. The two-regime method for optimizing stochastic reaction-diffusion simulations. *J. R. Soc. Interface 9*, 70 (2012), 859–68.

[54] Footer, M., Kerssemakers, J., Theriot, J., and Dogterom, M. Direct measurement of force generation by actin filament polymerization using an optical trap. *Proc. Natl. Acad. Sci. 104*, 7 (2007), 2181–2186.

[55] Foster, P. J., Furthauer, S., Shelley, M. J., and Needleman, D. J. Active contraction of microtubule networks. *Elife 4*, DECEMBER2015 (2015).

[56] Friedrich, B. M., Fischer-Friedrich, E., Gov, N. S., and Safran, S. a. Sarcomeric Pattern Formation by Actin Cluster Coalescence. *PLoS Comput. Biol. 8*, 6 (2012), e1002544.

[57] Fujiwara, I., Vavylonis, D., and Pollard, T. D. Polymerization kinetics of ADP- and ADP-Pi-actin determined by fluorescence microscopy. *Proc. Natl. Acad. Sci. U. S. A. 104*, 21 (2007), 8827–8832.

[58] Gao, T., Blackwell, R., Glaser, M. A., Betterton, M. D., and Shelley, M. J. Multiscale polar theory of microtubule and motor-protein assemblies. *Phys. Rev. Lett. 114*, 4 (2015).

[59] Gardel, M. L., Shin, J. H., MacKintosh, F. C., Mahadevan, L., Matsudaira, P., and Weitz, D. a. Elastic behavior of cross-linked and bundled actin networks. *Science 304*, 5675 (2004), 1301–1305.

[60] Gay, J. Modification of the overlap potential to mimic a linear sitesite potential. *J. Chem. Phys. 74*, 6 (1981), 3316.

[61] Geiger, B., Spatz, J. P., and Bershadsky, A. D. Environmental sensing through focal adhesions, 2009.

[62] Giancotti, F. G., and Ruoslahti, E. Integrin Signaling. *Science 285*, 5430 (1999), 1028–1032.

[63] Gibson, M. A., and Bruck, J. Efficient Exact Stochastic Simulation of Chemical Systems with Many Species and Many Channels. *J. Phys. Chem. A 104* (2000), 1876–1889.

[64] Gillespie, D. T. A general method for numerically simulating the stochastic time evolution of coupled chemical reactions. *J. Comput. Phys. 22*, 4 (1976), 403–434.

[65] Gillesple, D. T. Exact stochastic simulation of coupled chemical reactions. *J. Phys. Chem. 93555*, 1 (1977), 2340–2361.

[66] Gopinathan, A., Lee, K. C., Schwarz, J. M., and Liu, A. J. Branching, capping, and severing in dynamic actin structures. *Phys. Rev. Lett. 99*, 5 (2007), 1–4.

[67] Greenberg, M. J., Arpa, G., Tüzel, E., and Ostap, E. M. A Perspective on the Role of Myosins as Mechanosensors. *Biophys. J. 110*, 12 (2016), 2568–2576.

[68] Guo, B., and Guilford, W. H. Mechanics of actomyosin bonds in different nucleotide states are tuned to muscle contraction. *Proc. Natl. Acad. Sci. U. S. A. 103* (2006), 9844–9849.

[69] Gupton, S. L., and Waterman-Storer, C. M. Spatiotemporal Feedback between Actomyosin and Focal-Adhesion Systems Optimizes Rapid Cell Migration. *Cell 125*, 7 (2006), 1361–1374.

[70] Hermans, J., and Lentz, B. *Equilibria and Kinetics of Biological Macromolecules*. Wiley, 2014.

[71] Hill, A. V. The mechanical efficiency of frog's muscle. *Proc. R. Soc. London B 127*, 849 (1939), 434–451.

[72] Holmes, K. C., Popp, D., Gebhard, W., and Kabsch, W. Atomic model of the actin filament., 1990.

[73] Hotulainen, P., and Lappalainen, P. Stress fibers are generated by two distinct actin assembly mechanisms in motile cells. *J. Cell Biol. 173*, 3 (2006), 383–394.

[74] Hotulainen, P., Llano, O., Smirnov, S., Tanhuanpää, K., Faix, J., Rivera, C., and Lappalainen, P. Defning mechanisms of actin polymerization and depolymerization during Dendritic spine morphogenesis. *J. Cell Biol. 185*, 2 (2009), 323–339.

[75] Howard, J. *Mechanics of motor proteins and the cytoskeleton*. Sinauer, Sunderland, MA, 2001.

[76] Hu, K., Ji, L., Applegate, K. T., Danuser, G., and Waterman-Storer, C. M. Differential transmission of actin motion within focal adhesions. *Science 315*, 5808 (2007), 111–115.

[77] Hu, L., and Papoian, G. A. Mechano-chemical feedbacks regulate actin mesh growth in lamellipodial protrusions. *Biophys. J. 98*, 8 (2010), 1375–1384.

[78] Hu, L., and Papoian, G. A. Molecular transport modulates the adaptive response of branched actin networks to an external force. *J. Phys. Chem. B 117*, 42 (2013), 13388–13396.

[79] Hunter, a. W., and Wordeman, L. How motor proteins influence microtubule polymerization dynamics. *J. Cell Sci. 113 Pt 24* (2000), 4379–4389.

[80] Hussain, S., Molloy, J. E., and Khan, S. M. Spatiotemporal dynamics of actomyosin networks. *Biophys. J. 105*, 6 (2013), 1456–65.

[81] Johann, D., Goswami, D., and Kruse, K. Generation of Stable Overlaps between Antiparallel Filaments. *Phys. Rev. Lett. 115*, 11 (2015), 1–5.

[82] Jung, W., Murrell, M. P., and Kim, T. F-actin cross-linking enhances the stability of force generation in disordered actomyosin networks. *Comput. Part. Mech. 2*, 4 (2015), 317–327.

[83] Kampen, N. V. *Stochastic Processes in Physics and Chemistry*, 3rd ed. North Holland Personal Library, 1992.

[84] Kasza, K., Broedersz, C., Koenderink, G., Lin, Y., Messner, W., Millman, E., Nakamura, F., Stossel, T., MacKintosh, F., and Weitz, D. Actin Filament Length Tunes Elasticity of Flexibly Cross-Linked Actin Networks. *Biophys. J. 99*, 4 (2010), 1091–1100.

[85] Kim, T. Determinants of contractile forces generated in disorganized actomyosin bundles. *Biomech. Model. Mechanobiol. 14*, 2 (2014), 345–355.

[86] Kim, T., Hwang, W., and Kamm, R. D. Dynamic role of cross-linking proteins in actin rheology. *Biophys. J. 101*, 7 (2011), 1597–1603.

[87] Kim, T., Hwang, W., Lee, H., and Kamm, R. D. Computational analysis of viscoelastic properties of crosslinked actin networks. *PLoS Comput. Biol. 5*, 7 (2009), e1000439.

[88] Koenderink, G. H., and Paluch, E. K. Architecture shapes contractility in actomyosin networks. *Curr. Opin. Cell Biol. 50* (2018), 79–85.

[89] Köhler, S., and Bausch, A. R. Contraction mechanisms in composite active actin networks. *PLoS One 7*, 7 (2012), 1–8.

[90] Köhler, S., Schaller, V., and Bausch, A. R. Structure formation in active networks. *Nat. Mater. 10*, 6 (2011), 462–468.

[91] Kojima, H., Ishijima, A., and Yanagida, T. Direct measurement of stiffness of single actin filaments with and without tropomyosin by in vitro nanomanipulation. *Proc. Natl. Acad. Sci. 91*, 26 (1994), 12962–12966.

[92] Kolega, J. Cytoplasmic dynamics of myosin IIA and IIB: spatial 'sorting' of isoforms in locomoting cells. *J. Cell Sci. 111* (1998), 2085–2095.

[93] Komianos, J. E., and Papoian, G. A. Stochastic Ratcheting on a Funneled Energy Landscape is Necessary for Highly Efficient Contractility of Actomyosin Force Dipoles. *Phys. Rev. X 8*, 2 (2017), 21006.

[94] Korn, E. D., and Hammer, J. A. Myosins of nonmuscle cells. *Annu. Rev. Biophys. Biophys. Chem. 17* (1988), 23–45.

[95] Kovács, M., Thirumurugan, K., Knight, P. J., and Sellers, J. R. Load-dependent mechanism of nonmuscle myosin 2. *Proc. Natl. Acad. Sci. 104* (2007), 9994–9999.

[96] Kovács, M., Wang, F., Hu, A., Zhang, Y., and Sellers, J. R. Functional divergence of human cytoplasmic myosin II. Kinetic characterization of the non-muscle IIA isoform. *J. Biol. Chem. 278*, 40 (2003), 38132–38140.

[97] Kovar, D. R., Harris, E. S., Mahaffy, R., Higgs, H. N., and Pollard, T. D. Control of the assembly of ATP- and ADP-actin by formins and profilin. *Cell 124*, 2 (2006), 423–435.

[98] Kraikivski, P., and Slepchenko, B. M. Quantifying a Pathway: Kinetic Analysis of Actin Dendritic Nucleation. *Biophys. J. 99*, 3 (2010), 708–715.

[99] Kuramoto, Y. Effects of Diffusion on the Fluctuations in Open Chemical Systems. *Progress. Theor. Phys. 52* (1974), 711–713.

[100] Lan, Y., and Papoian, G. A. The stochastic dynamics of filopodial growth. *Biophys. J. 94*, 10 (2008), 3839–3852.

[101] Lansky, Z., Braun, M., Janson, M. E., Diez, S., Lansky, Z., Braun, M., Lu, A., Lüdecke, A., Schlierf, M., Ten Wolde, P. R., Janson, M. E., and Diez, S. Diffusible crosslinkers generate directed forces in microtubule networks. *Cell 160*, 6 (2015), 1159–1168.

[102] Laporte, D., Ojkic, N., Vavylonis, D., and Wu, J.-Q. Alpha-Actinin and fimbrin cooperate with myosin II to organize actomyosin bundles during contractile-ring assembly. *Mol. Biol. Cell 23*, 16 (2012), 3094–3110.

[103] Lenz, M. Geometrical origins of contractility in disordered actomyosin networks. *Phys. Rev. X 4*, 4 (2014), 041002.

[104] Lenz, M. Extensile actomyosin? 1–5.

[105] Lenz, M., Gardel, M. L., and Dinner, A. R. Requirements for contractility in disordered cytoskeletal bundles. *New J. Phys. 14*, 3 (2012), 033037.

[106] Lenz, M., Thoresen, T., Gardel, M. L., and Dinner, A. R. Contractile units in disordered actomyosin bundles arise from f-actin buckling. *Phys. Rev. Lett. 108*, 23 (2012).

[107] Levayer, R., and Lecuit, T. Biomechanical regulation of contractility: Spatial control and dynamics. *Trends Cell Biol. 22*, 2 (2012), 61–81.

[108] Levine, A. J., and MacKintosh, F. C. The mechanics and fluctuation spectrum of active gels. *J. Phys. Chem. B 113*, 12 (2009), 3820–3830.

[109] Lieleg, O., and Bausch, A. R. Cross-linker unbinding and self-similarity in bundled cytoskeletal networks. *Phys. Rev. Lett. 99*, 15 (2007), 1–4.

[110] Linsmeier, I., Banerjee, S., Oakes, P. W., Jung, W., Kim, T., and Murrell, M. P. Disordered actomyosin networks are sufficient to produce cooperative and telescopic contractility. *Nat. Commun. 7* (2016), 12615.

[111] Liu, A. P., Richmond, D. L., Maibaum, L., Pronk, S., Geissler, P. L., and Fletcher, D. A. Membrane-induced bundling of actinfilaments. *Nat. Phys. 4*, 10 (2008), 789–793.

[112] Low, S. H., Mukhina, S., Srinivas, V., Ng, C. Z., and Murata-Hori, M. Domain analysis of alpha-actinin reveals new aspects of its association with F-actin during cytokinesis. *Exp. Cell Res. 316*, 12 (2010), 1925–1934.

[113] Luo, T., Mohan, K., Iglesias, P. A., and Robinson, D. N. Molecular mechanisms of cellular mechanosensing. *Nat. Mater. 12*, 11 (2013), 1064–71.

[114] MacKintosh, F. C. Polymer-based models of cytoskeletal networks. *Cytoskelet. Mech. Model. Meas. Cell Mech. 2006*, 3 (2006), 152–169.

[115] Maly, I. V., and Borisy, G. G. Self-organization of a propulsive actin network as an evolutionary process. *Proc. Natl. Acad. Sci. 98*, 20 (2001), 11324–11329.

[116] Martin, A. C. Pulsation and stabilization: Contractile forces that underlie morphogenesis. *Dev. Biol. 341*, 1 (2010), 114–125.

[117] McFadden, W. M., McCall, P. M., Gardel, M. L., and Munro, E. M. Filament turnover tunes both force generation and dissipation to control long-range flows in a model actomyosin cortex. *PLoS Comput. Biol. 13*, 12 (2017), 1–27.

[118] Meyer, R. K., and Aebi, U. Bundling of actin-filaments by alpha-actinin depends on its molecular length. *J. Cell Biol. 110*, 6 (1990), 2013–2024.

[119] Miller, C. J., Bard Ermentrout, G., and Davidson, L. a. Rotational model for actin filament alignment by myosin. *J. Theor. Biol. 300* (2012), 344–359.

[120] Mitchison, T., and Kirschner, M. Dynamic instability of microtubule growth. *Nature 312*, 5991 (1984), 237–242.

[121] Mizuno, D., Tardin, C., Schmidt, C. F., and MacKintosh, F. C. Nonequilibrium Mechanics of Active Cytoskeletal Networks. *Science 315*, 5810 (2007), 370–373.

[122] Mogilner, A., and Edelstein-Keshet, L. Regulation of actin dynamics in rapidly moving cells: a quantitative analysis. *Biophys. J. 83*, 3 (2002), 1237–1258.

[123] Møller-Jensen, J., Borch, J., Dam, M., Jensen, R. B., Roepstorff, P., and Gerdes, K. Bacterial Mitosis: ParM of Plasmid R1 Moves Plasmid DNA by an Actin-like Insertional Polymerization Mechanism. *Mol. Cell 12*, 6 (2003), 1477–1487.

[124] Motility, A.-b., Rafelski, S. M., Alberts, J. B., and Odell, G. M. An experimental and computational study of the effect of ActA polarity on the speed of Listeria monocytogenes actin-based motility. *PLoS Comput. Biol. 5*, 7 (2009), e1000434.

[125] Müller, K. W., Cyron, C. J., and Wall, W. A. Computational analysis of morphologies and phase transitions of cross-linked, semi-flexible polymer networks. *Proc. R. Soc. London A 471*, 2182 (2015), 20150332.

[126] Mullins, R. D., Heuser, J. a., and Pollard, T. D. The interaction of Arp2/3 complex with actin: nucleation, high affinity pointed end capping, and formation of branching networks of filaments. *Proc. Natl. Acad. Sci. U. S. A. 95*, 11 (1998), 6181–6186.

[127] Murrell, M., Oakes, P. W., Lenz, M., and Gardel, M. L. Forcing cells into shape: the mechanics of actomyosin contractility. *Nat. Rev. Mol. Cell Biol. 16*, 8 (2015), 486–498.

[128] Murrell, M. P., and Gardel, M. L. F-actin buckling coordinates contractility and severing in a biomimetic actomyosin cortex. *Proc. Natl. Acad. Sci. 109*, 51 (2012), 20820–20825.

[129] Nagy, A., Takagi, Y., Billington, N., Sun, S. A., Hong, D. K. T., Homsher, E., Wang, A., and Sellers, J. R. Kinetic characterization of nonmuscle myosin IIB at the single molecule level. *J. Biol. Chem. 288*, 1 (2013), 709–722.

[130] Naumanen, P., Lappalainen, P., and Hotulainen, P. Mechanisms of actin stress fibre assembly. *J. Microsc. 231*, 3 (2008), 446–454.

[131] Nédélec, F. Computer simulations reveal motor properties generating stable antiparallel microtubule interactions. *J. Cell Biol. 158*, 6 (2002), 1005–1015.

[132] Nédélec, F., and Foethke, D. Collective Langevin dynamics of flexible cytoskeletal fibers. *New J. Phys. 9*, 11 (2007), 427.

[133] Newell-Litwa, K. A., Horwitz, R., and Lamers, M. L. Non-muscle myosin II in disease: mechanisms and therapeutic opportunities. *Dis. Model. Mech. 8*, 12 (2015), 1495–1515.

[134] Nishizaka, T., Seo, R., Tadakuma, H., Kinosita, K., and Ishiwata, S. Characterization of single actomyosin rigor bonds: load dependence of lifetime and mechanical properties. *Biophys. J. 79*, 2 (2000), 962–974.

[135] Norstrom, M. F., Smithback, P. A., and Rock, R. S. Unconventional processive mechanics of non-muscle myosin IIB. *J. Biol. Chem. 285*, 34 (2010), 26326–26334.

[136] Odell, G. M., and Foe, V. E. An agent-based model contrasts opposite effects of dynamic and stable microtubules on cleavage furrow positioning. *J. Cell Biol. 183*, 3 (2008), 471–483.

[137] Oelz, D. B., Rubinstein, B. Y., and Mogilner, A. A Combination of Actin Treadmilling and Cross-Linking Drives Contraction of Random Actomyosin Arrays. *Biophys. J. 109*, 9 (2015), 1818–1829.

[138] Ott, A., Magnasco, M., Simon, A., and Libchaber, A. Persistence of Actin. *Macromolecules 48*, 3 (1993), 1642.

[139] Pavlov, D., Muhlrad, A., Cooper, J., Wear, M., and Reisler, E. Actin Filament Severing by Cofilin. *J. Mol. Biol. 365*, 5 (2007), 1350–1358.

[140] Pellegrin, S., and Mellor, H. Actin stress fibres. *J. Cell Sci. 120*, 20 (2007), 3491–3499.

[141] Peskin, C. S., Odell, G. M., and Oster, G. F. Cellular Motions and Thermal Fluctuations: The Brownian Ratchet. *Biophys. J. 65*, 1 (1993), 316–324.

[142] Piazzesi, G., Reconditi, M., Linari, M., Lucii, L., Bianco, P., Brunello, E., Decostre, V. V., Stewart, A., Gore, D. B., Irving, T. C., Irving, M., and Lombardi, V. Skeletal Muscle Performance Determined by Modulation of Number of Myosin Motors Rather Than Motor Force or Stroke Size. *Cell 131*, 4 (2007), 784–795.

[143] Plimpton, S. Fast Parallel Algorithms for Short-Range Molecular Dynamics. *J. Comp. Phys. 117*, 1 (1995), 1–19.

[144] Pollard, T. D. Structure and polymerization of Acanthamoeba myosin-II filaments. *J. Cell Biol. 95*, 3 (1982), 816–825.

[145] Pollard, T. D. Actin and actin-binding proteins. *Cold Spring Harb. Perspect. Biol. 8*, 8 (2016).

[146] Pollard, T. D., Blanchoin, L., and Mullins, R. D. Molecular mechanisms controlling actin filament dynamics in nonmuscle cells. *Annu. Rev. Biophys. Biomol. Struct. 29* (2000), 545–76.

[147] Pollard, T. D., and Borisy, G. G. Cellular motility driven by assembly and disassembly of actin filaments. *Cell 112*, 4 (2003), 453–465.

[148] Popov, K., Komianos, J., and Papoian, G. A. MEDYAN : Mechanochemical Simulations of Contraction and Polarity Alignment in Actomyosin Networks. *PLoS Comput. Biol. 12*, 4 (2016), 1–40.

[149] Ramaswamy, R., González-Segredo, N., and Sbalzarini, I. F. A new class of highly efficient exact stochastic simulation algorithms for chemical reaction networks. *J. Chem. Phys. 130*, 24 (2009), 244104.

[150] Ramaswamy, R., and Sbalzarini, I. F. Exact on-lattice stochastic reaction-diffusion simulations using partial-propensity methods. *J. Chem. Phys. 135*, 24 (2011), 244103.

[151] Reif, F. *Fundamentals of Statistical and Thermal Physics*. McGraw-Hill, New York, 1965.

[152] Reymann, A.-C., Boujemaa-Paterski, R., Martiel, J.-L., Guerin, C., Cao, W., Chin, H. F., De La Cruz, E. M., Thery, M., and Blanchoin, L. Actin Network Architecture Can Determine Myosin Motor Activity. *Science 336*, 6086 (2012), 1310–1314.

[153] Roberts, E., Stone, J. E., and Luthey-Schulten, Z. Lattice microbes: High-performance stochastic simulation method for the reaction-diffusion master equation. *J. Comput. Chem. 34*, 3 (2013), 245–255.

[154] Rodriguez, J. V., Kaandorp, J. A., Dobrzynski, M., and Blom, J. G. Spatial stochastic modelling of the phosphoenolpyruvate-dependent phosphotransferase (PTS) pathway in Escherichia coli. *Bioinformatics 22*, 15 (2006), 1895–1901.

[155] Roland, J., Berro, J., Michelot, A., Blanchoin, L., and Martiel, J.-L. Stochastic severing of actin filaments by actin depolymerizing factor/cofilin controls the emergence of a steady dynamical regime. *Biophys. J. 94*, March (2008), 2082–2094.

[156] Ronceray, P., Broedersz, C., and Lenz, M. Fiber networks amplify active stress. *Proc Natl Acad Sci U S A 113*, 11 (2016).

[157] Rupp, B., and Nédélec, F. Patterns of molecular motors that guide and sort filaments. *Lab Chip 12* (2012), 4903.

[158] Saarikangas, J., Kourdougli, N., Senju, Y., Chazal, G., Segerstråle, M., Minkeviciene, R., Kuurne, J., Mattila, P. K., Garrett, L., Hölter, S. M., Becker, L., Racz, I., Hans, W., Klopstock, T., Wurst, W., Zimmer, A., Fuchs, H., Gailus-Durner, V., Hrabě de Angelis, M., von Ossowski, L., Taira, T., Lappalainen, P., Rivera, C., and Hotulainen, P. MIM-Induced Membrane Bending Promotes Dendritic Spine Initiation. *Dev. Cell 33*, 6 (2015), 644–659.

[159] Sajo, M., Ellis-Davies, G., and Morishita, H. Lynx1 Limits Dendritic Spine Turnover in the Adult Visual Cortex. *J. Neurosci. 36*, 36 (2016), 9472–9478.

[160] Salbreux, G., Charras, G., and Paluch, E. Actin cortex mechanics and cellular morphogenesis. *Trends Cell Biol. 22*, 10 (2012), 536–45.

[161] Sarman, S., and Laaksonen, A. Director alignment relative to the temperature gradient in nematic liquid crystals studied by molecular dynamics simulation. *Phys. Chem. Chem. Phys. 16*, 28 (2014), 14741–9.

[162] Schaub, S., Meister, J.-J., and Verkhovsky, A. B. Analysis of actin filament network organization in lamellipodia by comparing experimental and simulated images. *J. Cell Sci. 120*, 7 (2007), 1491–1500.

[163] Schmoller, K. M., Lieleg, O., and Bausch, a. R. Structural and viscoelastic properties of actin/filamin networks: Cross-linked versus bundled networks. *Biophys. J. 97*, 1 (2009), 83–89.

[164] Shaqfeh, E. S. G., and Koch, D. L. Orientational dispersion of fibers in extensional flows. *Phys. Fluid. A 2*, 7 (1990), 1077.

[165] Shutova, M., Yang, C., Vasiliev, J. M., and Svitkina, T. Functions of nonmuscle myosin ii in assembly of the cellular contractile system. *PLoS One 7*, 7 (2012).

[166] Shutova, M. S., Asokan, S. B., Talwar, S., Assoian, R. K., Bear, J. E., and Svitkina, T. M. Self-sorting of nonmuscle myosins IIA and IIB polarizes the cytoskeleton and modulates cell motility. *J. Cell Biol.* (2017), 1–14.

[167] Shutova, M. S., Spessott, W. A., Giraudo, C. G., and Svitkina, T. Endogenous species of mammalian nonmuscle myosin IIA and IIB include activated monomers and heteropolymers. *Curr. Biol. 24*, 17 (2014), 1958–1968.

[168] Small, J. V., Herzog, M., and Anderson, K. Actin filament organization in the fish keratocyte lamellipodium. *J. Cell Biol. 129*, 5 (1995), 1275–1286.

[169] Smith, B. a., Daugherty-Clarke, K., Goode, B. L., and Gelles, J. Pathway of actin filament branch formation by Arp2/3 complex revealed by single-molecule imaging. *Proc. Natl. Acad. Sci. U. S. A. 110*, 4 (2013), 1285–90.

[170] Smith, D., Ziebert, F., Humphrey, D., Duggan, C., Steinbeck, M., Zimmermann, W., and Käs, J. Molecular motor-induced instabilities and cross linkers determine biopolymer organization. *Biophys. J. 93*, 12 (2007), 4445–4452.

[171] Soares e Silva, M., Depken, M., Stuhrmann, B., Korsten, M., MacKintosh, F. C., and Koenderink, G. H. Active multistage coarsening of actin networks driven by myosin motors. *Proc. Natl. Acad. Sci. U. S. A. 108*, 23 (2011), 9408–9413.

[172] Somasi, M., Khomami, B., Woo, N. J., Hur, J. S., and Shaqfeh, E. S. G. Brownian dynamics simulations of bead-rod and bead-spring chains: Numerical algorithms and coarse-graining issues. *J. Nonnewton. Fluid Mech. 108*, 1-3 (2002), 227–255.

[173] Splettstoesser, T., Holmes, K. C., Noé, F., and Smith, J. C. Structural modeling and molecular dynamics simulation of the actin filament. *Proteins Struct. Funct. Bioinforma. 79*, 7 (2011), 2033–2043.

[174] Staiger, C. J. Signaling to the Actin Cytoskeleton in Plants. *Annu. Rev. Plant Physiol. Plant Mol. Biol. 51* (2000), 257–288.

[175] Stam, S., Alberts, J., Gardel, M. L., and Munro, E. Isoforms Confer Characteristic Force Generation and Mechanosensation by Myosin II Filaments. *Biophys. J. 108*, 8 (2015), 1997–2006.

[176] Stam, S., Freedman, S. L., Banerjee, S., Weirich, K. L., Dinner, R., Gardel, M. L., Dinner, A. R., and Gardel, M. L. Filament Rigidity and Connectivity Tune the Deformation Modes of Active Biopolymer Networks. *bioArxiv* (2017), 201708625.

[177] Stukalin, E. B., and Kolomeisky, A. B. ATP Hydrolysis Stimulates Large Length Fluctuations in Single Actin Filaments. *Biophys. J. 90*, 8 (2006), 2673–2685.

[178] Suarez, C., Roland, J., Boujemaa-Paterski, R., Kang, H., McCullough, B. R., Reymann, A. C., Guérin, C., Martiel, J. L., De La Cruz, E. M., and Blanchoin, L. Cofilin tunes the nucleotide state of actin filaments and severs at bare and decorated segment boundaries. *Curr. Biol. 21*, 10 (2011), 862–868.

[179] Sun, S. X., Walcott, S., and Wolgemuth, C. W. Cytoskeletal cross-linking and bundling in motor-independent contraction. *Curr. Biol. 20*, 15 (2010), R649–R654.

[180] Svitkina, T. M., Bulanova, E. A., Chaga, O. Y., Vignjevic, D. M., Kojima, S. I., Vasiliev, J. M., and Borisy, G. G. Mechanism of filopodia initiation by reorganization of a dendritic network. *J. Cell Biol. 160*, 3 (2003), 409–421.

[181] Tang, H., Laporte, D., and Vavylonis, D. Actin cable distribution and dynamics arising from cross-linking, motor pulling and filament turnover. *Mol. Biol. Cell 25*, 19 (2014), 3006–3016.

[182] Thoresen, T., Lenz, M., and Gardel, M. L. Thick filament length and isoform composition determine self-organized contractile units in actomyosin bundles. *Biophys. J. 104*, 3 (2013), 655–665.

[183] Tojkander, S., Gateva, G., Schevzov, G., Hotulainen, P., Naumanen, P., Martin, C., Gunning, P. W., and Lappalainen, P. A molecular pathway for myosin II recruitment to stress fibers. *Curr. Biol. 21*, 7 (2011), 539–550.

[184] VanBuren, V., Cassimeris, L., and Odde, D. J. Mechanochemical Model of Microtubule Structure and Self-Assembly Kinetics. *Biophys. J. 89*, 5 (2005), 2911–2926.

[185] Vavylonis, D., Kovar, D. R., O'Shaughnessy, B., and Pollard, T. D. Model of formin-associated actin filament elongation. *Mol. Cell 21* (2006), 455–466.

[186] Vavylonis, D., Wu, J.-Q., Hao, S., O'Shaughnessy, B., and Pollard, T. D. Assembly mechanism of the contractile ring for cytokinesis by fission yeast. *Science 319*, 2008 (2008), 97–100.

[187] Veigel, C., Molloy, J. E., Schmitz, S., and Kendrick-Jones, J. Load-dependent kinetics of force production by smooth muscle myosin measured with optical tweezers. *Nat. Cell Biol. 5*, 11 (2003), 980–986.

[188] Verkhovsky, A. B. Myosin II filament assemblies in the active lamella of fibroblasts their morphogenesis and role in the formation of actin filament bundles. *J. Cell Biol. 131*, 4 (1995), 989–1002.

[189] Verkhovsky, A. B., and Borisy, G. G. Non-Sarcomeric Mode of Myosin II Organization in the Fibroblast Lamellum. *J. Cell Biol. 123*, 3 (1993), 637–652.

[190] Verkhovsky, a. B., Svitkina, T. M., and Borisy, G. G. Polarity sorting of actin filaments in cytochalasin-treated fibroblasts. *J. Cell Sci. 110*, 11 (1997), 1693–1704.

[191] Vicente-Manzanares, M., Koach, M. A., Whitmore, L., Lamers, M. L., and Horwitz, A. F. Segregation and activation of myosin IIB creates a rear in migrating cells. *J. Cell Biol. 183*, 3 (2008), 543–554.

[192] Vicente-Manzanares, M., Ma, X., Adelstein, R. S., and Horwitz, A. R. Non-muscle myosin II takes centre stage in cell adhesion and migration. *Nat. Rev. Mol. Cell Biol. 10*, 11 (2009), 778–790.

[193] Vignaud, T. T. T., Blanchoin, L., Théry, M., and Thery, M. Directed cytoskeleton self-organization. *Trends Cell Biol. 22*, 12 (2012), 671–682.

[194] Vignjevic, D., Kojima, S.-i., Aratyn, Y., Danciu, O., Svitkina, T., and Borisy, G. G. Role of fascin in filopodial protrusion. *J. Cell Biol. 174*, 6 (2006), 863–75.

[195] Vignjevic, D., and Montagnac, G. Reorganisation of the dendritic actin network during cancer cell migration and invasion. *Semin. Cancer Biol. 18*, 1 (2008), 12–22.

[196] Vilfan, A., and Duke, T. Instabilities in the transient response of muscle. *Biophys. J. 85*, 2 (2003), 818–827.

[197] Vogel, V., and Sheetz, M. Local force and geometry sensing regulate cell functions. *Nat. Rev. Mol. Cell Biol. 7*, 4 (2006), 265–275.

[198] Wachsstock, D., Schwarz, W., and Pollard, T. Cross-linker dynamics determine the mechanical properties of actin gels. *Biophys. J. 66*, 3 (1994), 801–809.

[199] Wachsstock, D. H., Schwartz, W. H., and Pollard, T. D. Affinity of alpha-actinin for actin determines the structure and mechanical properties of actin filament gels. *Biophys. J. 65*, July (1993), 205–214.

[200] Walcott, S., and Sun, S. X. Active force generation in cross-linked filament bundles without motor proteins. *Phys. Rev. E - Stat. Nonlinear, Soft Matter Phys. 82*, 5 (2010), 1–4.

[201] Walcott, S., Warshaw, D. M., and Debold, E. P. Mechanical coupling between myosin molecules causes differences between ensemble and single-molecule measurements. *Biophys. J. 103*, 3 (2012), 501–510.

[202] Wang, H., and Vavylonis, D. Model of For3p-Mediated Actin Cable Assembly in Fission Yeast. *PLoS One 3*, 12 (2008), e4078.

[203] Wang, S., and Wolynes, P. G. Communication: Effective temperature and glassy dynamics of active matter. *J. Chem. Phys. 135*, 5 (2011), 051101.

[204] Wang, S., and Wolynes, P. G. Active contractility in actomyosin networks. *Proc. Natl. Acad. Sci. 109*, 17 (2012), 6446–6451.

[205] Wang, S., and Wolynes, P. G. Tensegrity and motor-driven effective interactions in a model cytoskeleton. *J. Chem. Phys. 136*, 14 (2012), 145102.

[206] Webber, S. E. Polymer Micelles : An Example of Self-Assembling Polymers. *J. Phys. Chem. B 5647*, 98 (1998), 2618–2626.

[207] Welf, E. S., and Haugh, J. M. Stochastic models of cell protrusion arising from spatiotemporal signaling and adhesion dynamics. *Methods Cell Biol. 110* (2012), 223–241.

[208] Yamaguchi, H., and Condeelis, J. Regulation of the actin cytoskeleton in cancer cell migration and invasion, 2007.

[209] Yildiz, a., and Selvin, P. R. Fluorescence imaging with one manometer accuracy: Application to molecular motors. *Acc. Chem. Res. 38*, 7 (2005), 574–582.

[210] Zhuravlev, P. I., Lan, Y., Minakova, M. S., and Papoian, G. A. Theory of active transport in filopodia and stereocilia. *Proc. Natl. Acad. Sci. 109*, 27 (2012), 10849–10854.

[211] Zhuravlev, P. I., and Papoian, G. A. Molecular noise of capping protein binding induces macroscopic instability in filopodial dynamics. *Proc. Natl. Acad. Sci. 106*, 28 (2009), 11570–11575.

[212] Zhuravlev, P. I., and Papoian, G. A. Protein fluxes along the filopodium as a framework for understanding the growth-retraction dynamics: the interplay between diffusion and active transport. *Cell Adh. Migr. 5*, 5 (2011), 448–456.